

MODELING OF RESIN TRANSFER MOLDING FOR COMPOSITES
MANUFACTURING

A THESIS SUBMITTED TO
THE GRADUATE SCHOOL OF NATURAL AND APPLIED SCIENCES
OF
MIDDLE EAST TECHNICAL UNIVERSITY

BY

HAKAN İPEK

IN PARTIAL FULFILLMENT OF THE REQUIREMENTS
FOR THE DEGREE OF MASTER OF SCIENCE
IN
MECHANICAL ENGINEERING

NOVEMBER 2005

Approval of the Graduate School of Natural and Applied Sciences

Prof. Dr. Canan ÖZGEN
Director

I certify that this thesis satisfies all the requirements as a thesis for the degree of Master of Science.

Prof. Dr. S. Kemal İDER
Head of Department

This is to certify that we have read this thesis and that in our opinion it is fully adequate, in scope and quality, as a thesis for the degree of Master of Science.

Assist. Prof. Dr. Merve ERDAL
Supervisor

Examining Committee Members

Prof. Dr. Mustafa İlhan GÖKLER	(METU, ME)	_____
Assist. Prof. Dr. Merve ERDAL	(METU, ME)	_____
Assist. Prof. Dr. Serkan DAĞ	(METU, ME)	_____
Assist. Prof. Dr. Cüneyt SERT	(METU, ME)	_____
M.S. Fikret ŞENEL	(Barış Elektrik End. A.Ş.)	_____

I hereby declare that all information in this document has been obtained and presented in accordance with academic rules and ethical conduct. I also declare that, as required by these rules and conduct, I have fully cited and referenced all material and results that are not original to this work.

Name, Last name : Hakan İPEK

Signature :

ABSTRACT

MODELING OF RESIN TRANSFER MOLDING FOR COMPOSITES MANUFACTURING

İpek, Hakan

M.S., Department of Mechanical Engineering

Supervisor: Assist. Prof. Dr. Merve Erdal

November 2005, 122 pages

The resin transfer molding (RTM) process, in which a thermosetting resin is injected into a mold cavity preloaded with a porous fiber preform, is a manufacturing method for producing advanced continuous fiber reinforced composite products with complex geometries. Numerical simulation of resin transfer molding process is an often needed tool in manufacturing design, in order to analyze the process before the mold is constructed. In this study, a numerical simulation of the resin impregnation process in RTM of composite materials is performed by using and modifying an existing simulation program. The parts that are molded in the simulations have their planar dimensions much larger than their thicknesses. Therefore, the mold filling process can be modeled as two dimensional by neglecting the variations along the thickness direction. The program is capable of simulating two-dimensional, isothermal impregnation processes through orthotropic fiber preforms of planar but complex geometries. The formulations of the physical problem, used in this study, were taken from the theory of macroscopic flow through anisotropic porous media. The formulated governing equation and boundary conditions are solved in a regular-geometry computational domain by transformation through boundary fitted coordinate system. The discretization for numerical solution is performed by

the finite difference method. The current study extends the existing capabilities of the simulation program by enabling the simulation of impregnation through non-homogeneous fiber preforms. Furthermore, the capability to simulate injection from two gates (as opposed to a single gate injection that existed before) is developed and added to the program. Various one-dimensional impregnation simulations (as parametric studies) are performed to assess the influence of process parameters. Results are also compared with analytical solutions and found to be in agreement with them. Two-dimensional impregnation simulations are performed for a planar, complex geometry mold. The two-dimensional results are compared with experimental results from the literature and are found to be in acceptable agreement with them. In addition to the study of various parametric variations in two-dimensional impregnation, double-gate resin injection simulations are performed and discussed as well.

Keywords: Resin Transfer Molding, Numerical Modeling, Multiple Gate Resin Injection.

ÖZ

REÇİNE TRANSFERLEME YÖNTEMİ İLE BİRLEŞİK MALZEME ÜRETİMİ

İpek, Hakan

Yüksek Lisans, Makina Mühendisliği Bölümü

Tez Yöneticisi: Yard. Doç .Dr. Merve Erdal

Kasım 2005, 122 pages

Boş kalıba yerleştirilmiş gözenekli elyaf yapıya termofiksaj reçinenin enjekte edildiği reçine transfer kalıplaması, karışık geometrili, ileri kompozit ürünlerin üretilmesi için kullanılan bir yöntemdir. Reçine transfer kalıplaması sürecinin sayısal simülasyonu, üretim modellemesinde kalıp imal edilmeden önceki süreci analiz etmek amacıyla ihtiyaç duyulan bir araçtır. Bu çalışmada, mevcut bir simülasyon programı kullanılarak ve geliştirilerek, kompozit malzemenin reçine transfer kalıplamasında, reçine emdirme sürecinin sayısal simülasyonu gerçekleştirilmiştir. Simülasyonda kalıplanan parçaların düzlemsel ebatları kalınlıklarından çok daha fazladır. Bu nedenle, reçine transferi süreci, kalınlık yönündeki süreçteki değişimler gözardı edilerek iki boyutlu olarak modellenabilir. Program, iki boyutlu ortotropik elyaf yapılarının düzlemsel, karmaşık geometrileri boyunca, eş sıcaklıklı, emdirme sürecinin simülasyonunu yapabilir. Çalışmada kullanılan fiziksel problemin formülasyonu, eşyönsüz gözenekli ortam boyunca gerçekleşen iri ölçekli akım teorisinden alınmıştır. Emdirme sürecini modelleyen matematiksel formülasyonlar ve sınır koşulları, sınırlara sıkıştırılmış koordinat sistemi kullanılarak dönüşümü yapılmış düzgün geometrik sayısal alanda çözülmüştür. Sayısal çözüm için gerekli olan süreksiz hale getirme, sonlu farklılıklar metoduyla gerçekleştirilmiştir. Bu çalışmada, homojen olmayan elyaf yapılar emdirme simülasyonu gerçekleştirilerek, simülasyon

programının yetenekleri genişletilmiştir. Ayrıca, (programdaki mevcut tek kapılı enjeksiyon simülasyonuna ek olarak) iki kapılı enjeksiyon simülasyonu geliştirilmiş ve programa eklenmiştir. Süreç parametrelerinin etkilerine değer biçmek için, çeşitli bir boyutlu emdirme simülasyonları (parametrik çalışmalar) gerçekleştirilmiştir. Sonuçlar analitik çözümlerle karşılaştırılmış ve onlarla uyumlu olduğu gözlenmiştir. İki boyutlu emdirme simülasyonu düzlemsel, karışık geometrik kalıplar için uygulanmıştır. İki boyutlu sonuçlar daha önce yapılan çalışmalardaki deneysel sonuçlarla karşılaştırılmış ve onlarla kabuledilebilir uyumda olduğu görülmüştür. Bunlara ek olarak, iki kapılı reçine emdirme simülasyonları gerçekleştirilmiş ve sonuçları tartışılmıştır.

Anahtar Kelimeler: Reçine Transfer Kalıplaması, Sayısal Modelleme, Çok Kapılı Reçine Enjeksiyonu.

To My Parents

ACKNOWLEDGMENTS

I should express my thanks to my supervisor Assist. Prof. Dr. Merve Erdal for her guidance and endless criticism that taught me more than I dream, insight and during our study.

I owe thanks to my home-mate Erhan Karabaş for his support, help and understanding. Thanks go to Mehmet for sparing time to me. And thanks go to Semih for our small talks and small tours whenever I was tired and bored.

I owe a big thank to my parents for their support and faith at every stage of my education. Thank you Zeynep for the days you were with me and for being nearby whenever I was in need of you.

TABLE OF CONTENTS

PLAGIARISM.....	iv
ABSTRACT.....	v
ÖZ.....	vii
ACKNOWLEDGMENTS.....	x
TABLE OF CONTENTS.....	xi
1. INTRODUCTION.....	1
1.1 Description of the Resin Transfer Molding (RTM) Process.....	1
1.2 Composite Material Components	5
1.3 RTM Process Among Other Composite Manufacturing Techniques	9
1.4 The Need for Modeling in RTM	13
1.5 Scope of the Thesis Study.....	14
2. RESIN TRANSFER MOLDING MODELING.....	16
2.1 Literature Review of Darcy Type Flow Simulations.....	16
2.2 Current Model.....	19
2.2.1 Formulation of the Problem	20
2.2.2 Boundary Conditions	22
2.2.2 Physical Significant of Process Parameters.....	26
3. NUMERICAL IMPLEMENTATION AND SOLUTION	28
3.1 Transformation of Governing Equation and Boundary Conditions to Computational Domain from Physical Domain	28
3.1.1 Boundary-Fitted Coordinate System and Elliptic Grid Generation	29
3.1.2 Governing Equation and Boundary Conditions in the Computational Domain	32
3.2 Discretization of Governing Equation and Boundary Conditions in Transformed Solution Domain	40
3.3 Solution Method	44

3.4 Determination of Process Parameters	44
3.4.1 Velocity	44
3.4.2 Pressure.....	45
3.5 Evolution of Flow Domain.....	47
3.5.1 Solution Sequence in the Program	47
3.5.2 Flow Front Advancement	48
3.6 Double Gate Injection Simulation.....	49
3.6.1 First Contact of Two Advancing Flow Fronts.....	51
3.6.2 Further Contact of Two Advancing and Merging Flow Fronts	54
4. RESULTS AND DISCUSSION	58
4.1 1-D RTM Simulations	58
4.1.1 Permeability Analysis	60
4.1.2 Velocity Analysis.....	61
4.1.3 Viscosity Analysis	62
4.1.4 Fiber Volume Fraction Analysis.....	63
4.2 2-D RTM Simulations	65
4.2.1 Comparison of Model Results with Experiment	66
4.2.2 Velocity Analysis.....	68
4.2.3 Viscosity Analysis	73
4.2.4 Fiber Volume Fraction Analysis.....	76
4.2.4.1 Homogeneous Fiber Volume Fraction..	76
4.2.4.2 Non homogeneous Fiber Volume Fraction.....	77
4.2.5 Permeability Analysis.....	82
4.2.5.1 Homogeneous and Isotropic Preform Permeability.....	83
4.2.5.2 Homogeneous and Anisotropic Preform Permeability.....	85
4.2.5.3 Non-homogeneous and Anisotropic Preform Permeability.....	89
4.3 Double Gate RTM Analysis	95

5. CONCLUSION	102
REFERENCES.....	105
APPENDICES	
A: INTERCHANGING THE DEPENDENT AND INDEPENDENT VARIABLES IN GRID GENERATION EQUATIONS.....	109
B: FINITE DIFFERENCE EXPRESSIONS.....	112
C: PRESSURE EQUATION DISCRETIZATION....	114
D: COMPUTER PROGRAM FLOW CHART.....	118

LIST OF FIGURES

Figure 1.1	A modern civil aero-engine.....	2
Figure 1.2	Auto body panels and automobile structure parts.....	2
Figure 1.3	Sketch of resin transfer molding process.....	3
Figure 1.4	Various stages of the RTM process.....	4
Figure 1.5	Woven preform architectures.....	6
Figure 1.6	Various fiber types.....	8
Figure 1.1	Composite manufacturing methods.....	10
Figure 2.1	A typical impregnation process in mold space.....	16
Figure 2.2	Different regions involved in the impregnation of a fiber tow bundle embedded in a medium of higher permeability.....	17
Figure 2.3	Mold wall boundary condition.....	23
Figure 2.4	Boundary conditions.....	24
Figure 2.5	Resin flow fronts spreading out from a center gate as the resin fills an anisotropic preform.....	27
Figure 3.1	Physical and computational domains of a boundary fitted coordinate system transformation applied to a sample resin transfer molding process.....	30
Figure 3.2	Boundary conditions.....	36
Figure 3.3	Impregnation front advancement with slip based contact point relocations.....	48
Figure 3.4	The impregnation front advancement with imposed orthogonality based contact point relocation.....	49
Figure 3.5	Double gate injection in a two dimensional irregular geometry mold cavity.....	50
Figure 3.6	The initial contact of two advancing resin flow fronts.....	52
Figure 3.7	Computational domain before and at first contact of two advancing flow fronts.....	52
Figure 3.8	Determination of the contact point on merging flow fronts.....	55
Figure 3.9	The merging of two flow fronts (nodes 1 to 4 are contact nodes).....	56
Figure 4.1	1-D Mold Configuration.....	58

Figure 4.2	Variation of inlet pressure during one-dimensional RTM under constant injection rate.....	60
Figure 4.3	Variation inlet pressure during one dimensional RTM constant injection rate with different perform permeabilities values.....	61
Figure 4.4	Variation in inlet pressure and fill time during one dimensional RTM under different injection velocities.....	62
Figure 4.5	Variation of inlet pressure for one dimensional RTM under constant inlet velocity for different resin viscosities.....	63
Figure 4.6	Variation in inlet pressure for one dimensional RTM under constant inlet velocity for different fiber volume fractions.....	64
Figure 4.7	The irregular mold for 2-D analysis.....	65
Figure 4.8	The mold cavity for model-experiment comparison.....	66
Figure 4.9	Comparison of experiment and simulation results for 2-D resin impregnation through an irregular mold geometry.....	67
Figure 4.10	Resin flow progression and corresponding boundary fitted mesh systems for different resin inlet velocities.....	68
Figure 4.11	Inlet pressure variations at different inlet velocities.....	70
Figure 4.12	Flow front progressions for varying injection velocity.....	71
Figure 4.13	Pressure distributions at the instance of fill for varying injection velocity conditions.....	72
Figure 4.14	Flow front progressions for different resin viscosities at constant injection rates. (flow fronts plotted every $\Delta t = 20s$ time increment).....	74
Figure 4.15	Inlet pressure variations at different inlet viscosities for constant injection rates.....	75
Figure 4.16	Pressure distributions at the instance of fill for different resin viscosities at constant injection rates.....	75
Figure 4.17	Flow front progressions for different fiber volume fractions (homogeneous preform) at constant resin injection rate. (Flow fronts plotted every $\Delta t = 20s$ time increment).....	78
Figure 4.18	Inlet pressure rise with time at different volume fractions.....	79
Figure 4.19	Non homogeneous preform configurations for simulations in cases 2 and 3.....	80

Figure 4.20	Flow front progressions for homogeneous and non-homogeneous fiber volume fraction (flow fronts plotted every $\Delta t = 40s$ time increment).....	81
Figure 4.21	The change of inlet pressure with time according to the different volume fractions conditions.....	82
Figure 4.22	Pressure distributions at the instance of fill for homogeneous and non-homogeneous fiber volume fraction preform at constant injection rate.....	83
Figure 4.23	Inlet pressure variations for different values of homogeneous and isotropic preform permeability at constant injection rates	85
Figure 4.24	Pressure distributions at the instance of fill for different values of homogeneous and isotropic preform permeability at constant injection rates.....	86
Figure 4.25	Comparison of the flow fronts at two time instances, for homogeneous, anisotropic preform permeability at constant injection rate.....	87
Figure 4.26	Flow front progressions for homogeneous and anisotropic permeability preforms at constant injection rates (flow fronts plotted every $\Delta t = 20s$ time increment).....	88
Figure 4.27	Inlet pressure variation for different levels of anisotropy for homogeneous preforms at constant injection rates.....	89
Figure 4.28	Pressure distribution at the instance of fill at various anisotropy levels for homogeneous preform.....	90
Figure 4.29	Non homogeneous preform configurations for anisotropic, non homogeneous preform permeability simulations.....	92
Figure 4.30	Comparison of the flow fronts at two time instances for nonhomogenous isotropic-anisotropic preform permeability at constant injection rate.....	93
Figure 4.31	Flow front progressions for non-homogeneous isotropic-anisotropic permeability cases. (flow fronts plotted every $\Delta t = 40s$ time increment).....	94
Figure 4.32	Inlet pressure variation for different levels of anisotropy for nonhomogeneous preforms at constant injection rates.....	95

Figure 4.33	Pressure distributions at the instance of fill at various nonhomogeneous levels for isotropic/anisotropic preform.....	96
Figure 4.34	Location of resin flow front at various time levels for double gate resin injection (same injection rates at both gates).....	97
Figure 4.35	Flow front progressions for double gate resin injection.....	98
Figure 4.36	" Weld " line formed by merging of the two flow fronts (at the same resin injection rate).....	99
Figure 4.37	Comparisons of inlet pressure at gates 1 and 2 from double gate resin injection and single gate (gate 1) injection.....	99
Figure 4.38	Pressure distribution at various instances of double gate resin injection.....	100
Figure 4.39	Flow front progressions for double gate resin injection rates (different injection rates at the gates).....	101
Figure C.1	Nodal point regions used discretized pressure equation.....	110

LIST OF TABLES

Table 1.1	Typical Fibre Properties (Costs are approximate and may change with quantity, fabric weight and style).....	7
Table 3.1	The geometrical coefficients of equation.....	39
Table 4.1	Process parameters and results for 1-D flow verification studies.....	59
Table 4.2	Process parameters and results for 1-D permeability analysis.....	60
Table 4.3	Process parameters and results for 1-D velocity analysis.....	62
Table 4.4	Process parameters and results for 1-D viscosity analysis....	63
Table 4.5	Process parameters and results for 1-D volume fraction analysis.....	64
Table 4.6	Process parameters for 2-D velocity analysis.....	68
Table 4.7	Process Parameters for 2-D Viscosity Analysis.....	73
Table 4.8	Process Parameters for 2-D Volume Fraction Analysis.....	76
Table 4.9	Process Parameters for 2-D Non-homogeneous Volume Fraction Analysis.....	79
Table 4.10	Process parameters for 2-D homogeneous and isotropic preform permeability analysis.....	85
Table 4.11	Process parameters for 2-D onhomogenous and anisotropic perform permeability analysis.....	91
Table 4.12	Process parameters for double gate resin injection (same injection rates at both gates).....	97
Table 4.13	The simulation data for 2-D homogeneous and isotropic double gate run.....	101

CHAPTER I

INTRODUCTION

1.1 Description of the Resin Transfer Molding (RTM) Process

The use of continuous fiber reinforced polymeric matrix composite materials in high technology applications has been increasing in the last 20-25 years. This is due to the favorable characteristics that composite parts have been shown to exhibit when compared with traditional metals for many applications. Among these characteristics is higher stiffness to weight ratios, versatile structural performance capabilities, increased environmental resistance, decreased thermal expansion, and improved fatigue life. Today, with the acceptance of advanced composite materials as viable components for a wide range of applications, the challenge to manufacture reliable composite parts with predictable microstructures in productive and cost effective manners has gained significant importance [1].

Resin transfer molding (RTM), also referred to as liquid molding, is one of the most popular manufacturing processes for producing continuous fiber reinforced composite materials. RTM can significantly cut manufacturing cycle times compared to other composite process methods and it is a viable method for mass production of composites parts. It can be adapted for use as a processing stage in an automated, repeatable manufacturing process for greater efficiency, reducing cycle time. RTM is used in the production of the low-cost/high-volume 500-50,000 parts per year of the automotive industry as well as higher performance/lower volume 50-5,000 parts per year of the aerospace industry [2].

Figure 1.1 shows a modern civil aircraft engine which has several components produced by RTM. Among these components are fan blades

(component 3) on the figure, noise cone (component 4) and nose cowl (component 5) [3].

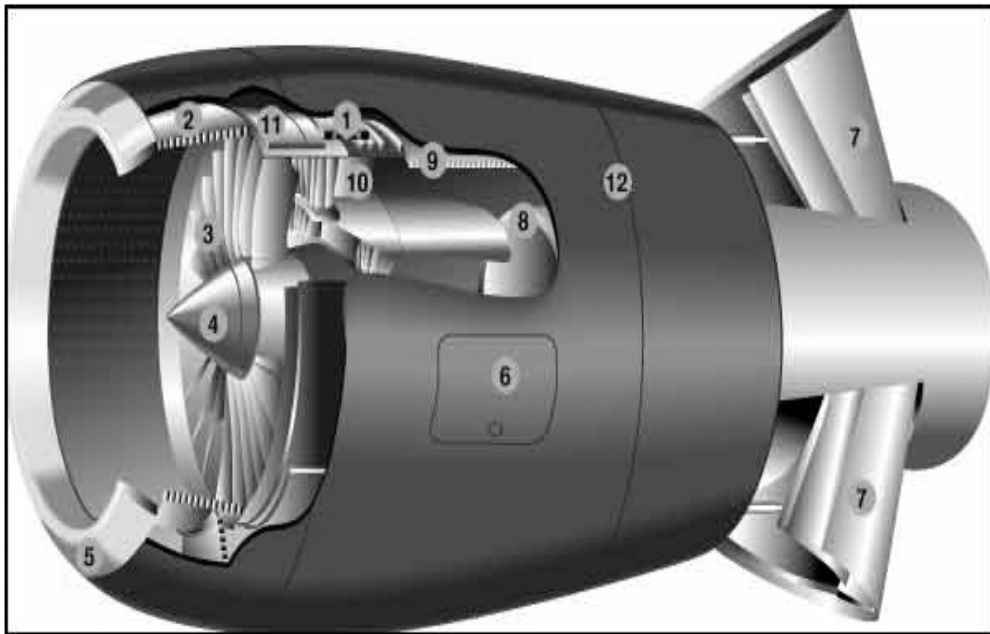


Figure 1.1 A modern civil aero-engine [3].

Some other industry applications of the RTM process include

- Automotive industry (auto body panels, truck air deflector, caravan components, see Figure 1.2)
- Consumer products (Antenna dishes, chairs, swim pool panels, bathtub/ shower units, solar collectors...)
- Aerospace and military
- Corrosion resistance applications (chemical storage tanks, tubes...)
- Wind turbine blades.

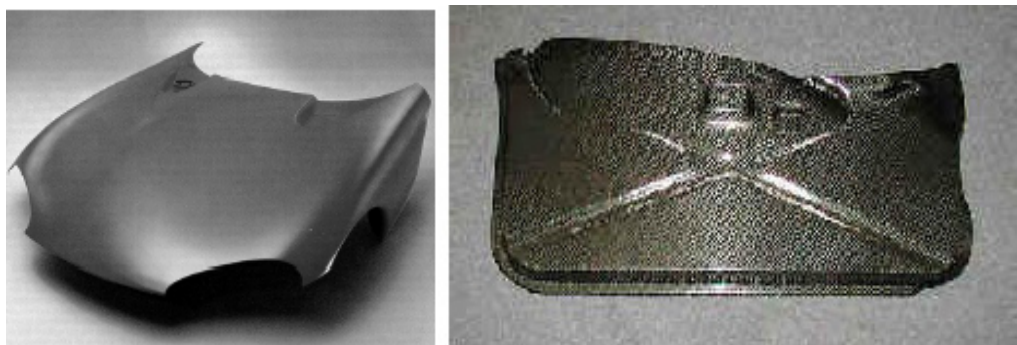


Figure 1.2 Auto body panels and automobile structure parts [4].

The RTM process involves impregnating a fiber reinforcement preplaced in a closed mold with a suitable catalyzed liquid resin, which cures into a solid form in the shape of the mold cavity. Figure 1.3 presents schematic of the process.

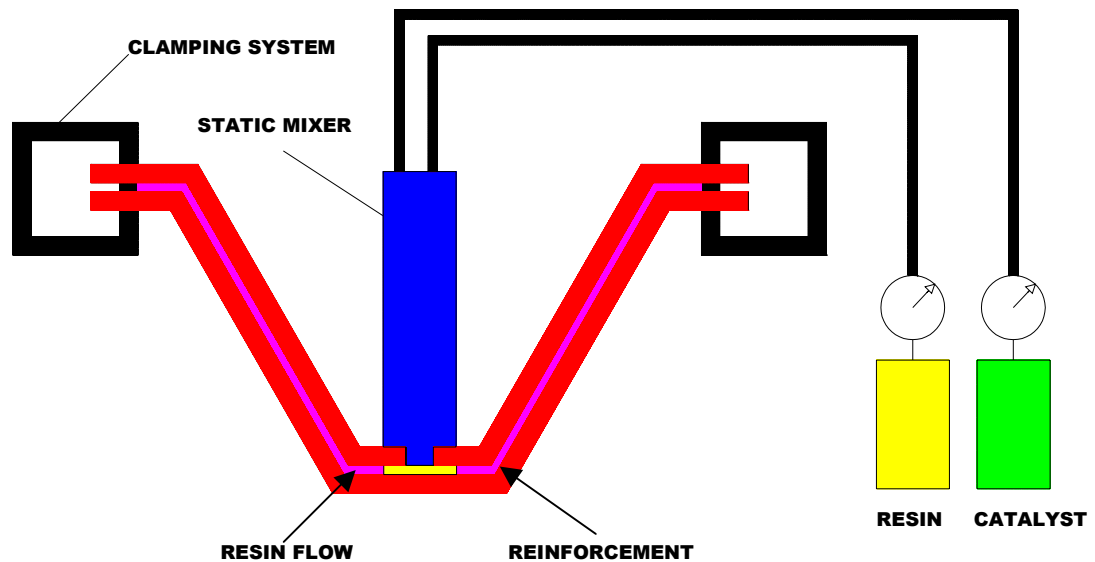


Figure 1.3 Sketch of resin transfer molding process [5]

At first, a dry (un-impregnated), preshaped reinforcing fiber mat, is placed into a female or male mold according to the shape of mold (Figure 1.4). The preshaped reinforcing mat, which is also known as preform, can be woven or non-woven fiber strands, which form the load bearing component of the composite.

After the reinforcing mat is placed, the mold is closed and tightly sealed around all edges with perimeter gaskets. The liquid resin and catalyst are mixed in dispenser equipment, and then pumped into the mold under low pressure, through properly positioned gates, following predesigned paths through the preform. The liquid resin impregnates the fiber reinforcement, forming the load-transferring matrix component and giving rigidity to the composite. Air vents opens on the mold through which air inside the mold, that is being replaced by the resin, must be vented out. Typically, injection is carried out from the bottom of the part and air vents are positioned at various

locations around the mold. The vents are generally placed around the top perimeter of the mold (Figure 1.4).

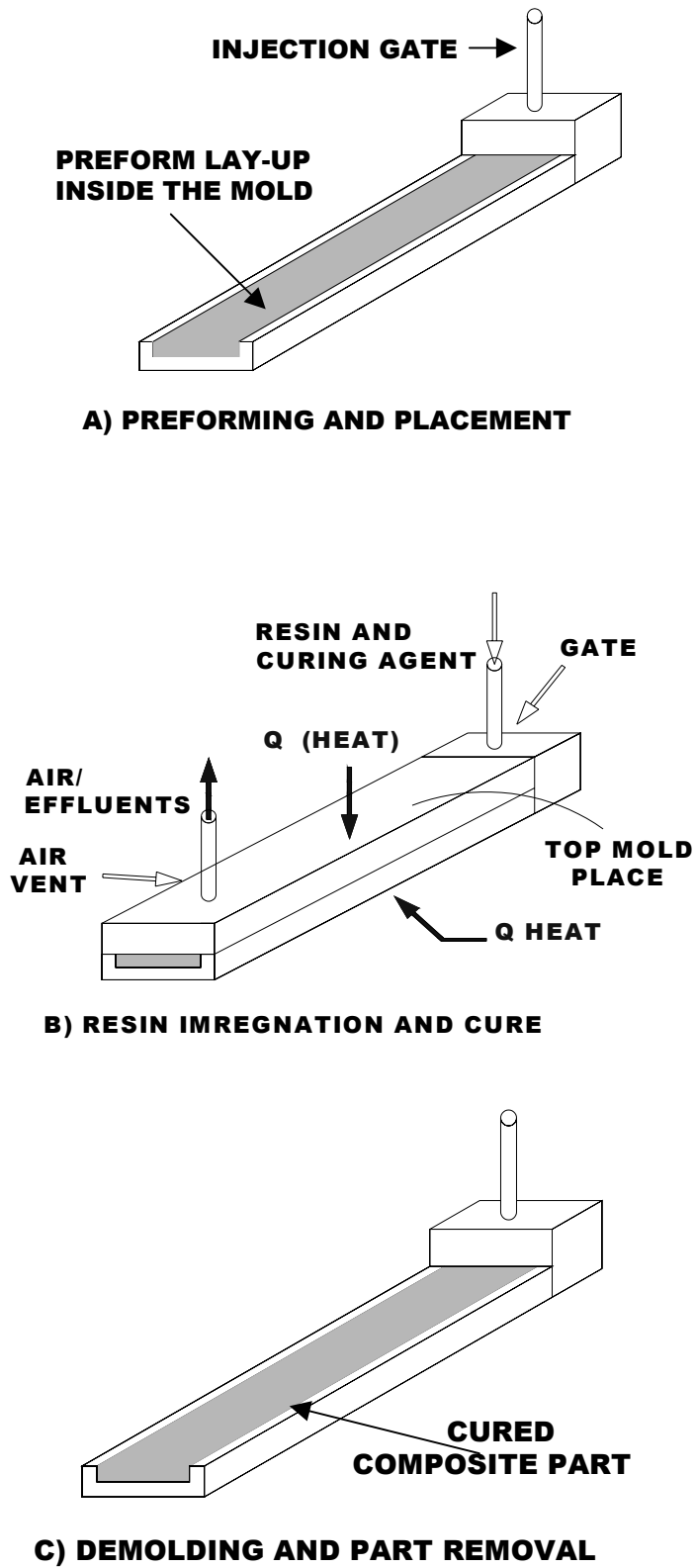


Figure 1.4 Various stages of the RTM process [6]

When the resin completely fills the mold cavity, the injection process is stopped. After the filling cycle, the parts are cured usually at room temperature (sometimes the mold can be heated to accelerate cure) and subsequently, the mold is opened and finished part is removed. The processing stages are shown in Figure 1.4. Usually a gel coating is applied to the mold cavity surfaces prior to the injection process to allow for smooth resin flow. This application is useful for improving the finished product surface quality and allowing for the easy removal of finished parts. In the RTM processes, low-viscosity resins are used to permeate preforms quickly and evenly before the onset of cure. Both mold and resin can be heated, if necessary, depending on the material and application. Parts manufactured through RTM do not need to be autoclaved. However, once cured and demolded, a part destined for a high-temperature application usually undergoes post-cure operation.

1.2 Composite Material Components

Reinforcement and resin are the two basic materials used in RTM process to produce composites. RTM can use a wide variety of different reinforcement and resin systems to obtain a composite material with a broad spectrum of properties. Since each fiber and resin material brings its own contribution to the composite, knowledge of raw material properties is the first step in designing a satisfactory composite product. The reinforcement provides mechanical properties such as stiffness, tension and impact strength and the resin system (matrix) provides physical properties including resistance to fire, weather, ultraviolet light and corrosive chemicals, as well as the rigidity necessary for a solid composite form.

The selection of reinforcing fibres and fiber architecture directly affects the performance of the composite and the process design. Fiber architecture selection depends on performance issues such as modulus, strength, durability, compressibility during preforming to attain adequate volume

fractions and drapability to insure proper placement of the reinforcement during preforming operations.[2] The fibers are stitched or woven into various two-dimensional or three-dimensional architectures for RTM applications as seen in Figure 1.5.

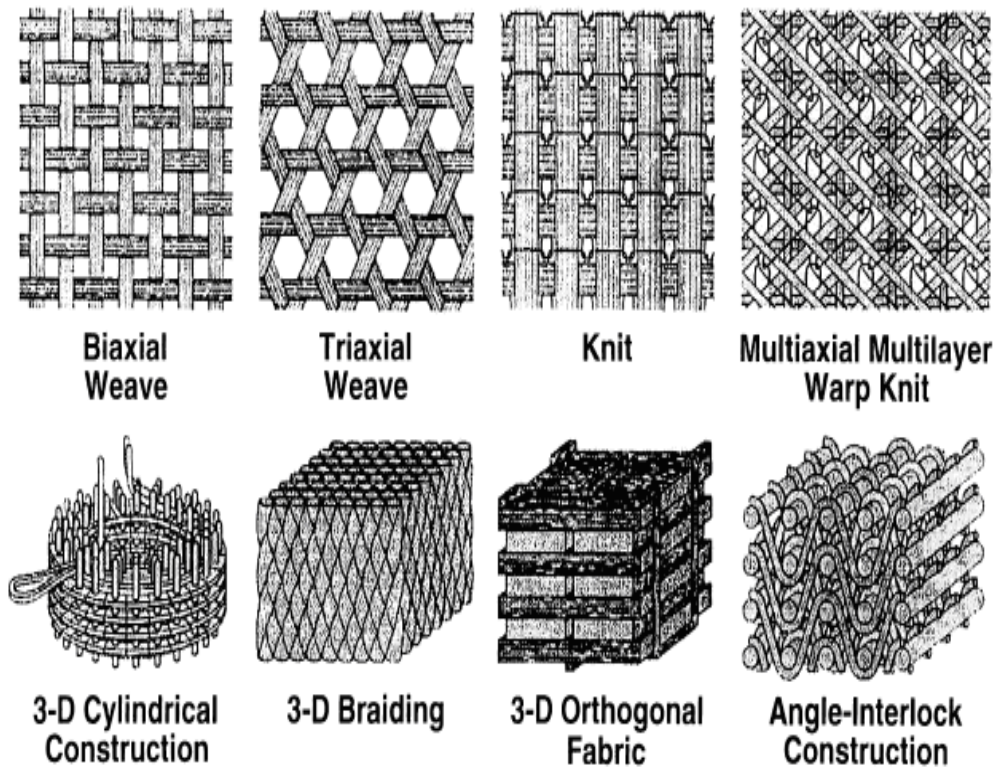


Figure 1.5 Woven preform architectures [2]

The fiber material is another important parameter in the end-product performance. Table 1.1 presents various fiber types and their properties. Figure 1.6 shows various fibers. The glass fiber is the most widely used reinforcement material, because it is readily available and comparatively cheaper than others such as Carbon or Aramid.

E-Glass is of lower strength and stiffness than the other fibers in Table 1.1, but is also considerably lower in cost. This fiber is denser than the alternatives and resulting structures reinforced with E-Glass will therefore be heavier than those reinforced with higher performance fibers. Typically, an E-Glass structure may be over twice the weight of a Carbon or Aramid

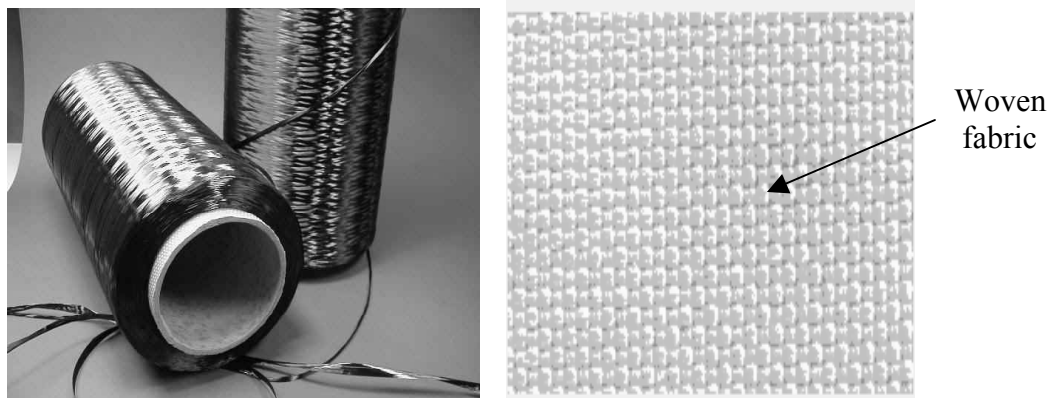
reinforced composite structure. This fiber is electrically nonconductive and offers good corrosion resistance.

Table 1.1 Typical Fibre Properties (Costs are approximate and may change with quantity, fabric weight and style) [7].

	E-Glass	S-Glass	Aramid (Kevlar 49)	High Strength Carbon	High Modulus Carbon	Polyeth- Ylene (Dyneema Sk65)
Tensile Strength (MPa)	2400	3100	3600	3300-6370	2600-4700	3000
Tensile Modulus (GPa)	70	86	130	230-300	345-590	95
Failure Strain (%)	3.5	4.0	2.5	1.5-2.2	0.6-1.4	3.6
Density (Kg / m^3)	2560	2490	1440	1800	1900	970
Coefficient of Thermal Exp ($10^{-6}/iC$)	5.0	5.6	$-2L^*+59T^*$	$-1L^*+17T^*$	$-1L^*$	$-12L^*$
Fiber Cost (£/kg)	1.25	7	15	10-15	~60	20-30
Fabric** Cost (£/kg)	2-3	10-15	20-25	15-35	~100	30-50
Specific Fabric Cost ($£/m^3 \times 10^{-3}$)	5-8	25-37	29-36	27-63	~190	29-49
<p>*L= Longitudinal length T=Transverse length **Fibers woven into fabric *** Price quotes as of November, 2005</p>						



a) Glass Fiber



b) Carbon Fiber

c) Ballistic Kevlar

Figure 1.6 Various fiber types [8]

Carbon fibers are available in a wide range of grades offering different mechanical properties. All carbon fibers offer relatively high strengths and stiffness, but are brittle and fail at relatively low strain levels. They have a negative coefficient of thermal expansion [8].

Aramid fibers such as Kevlar offer very high tensile strengths and relatively high elongation to failure. This results in good energy absorbance capabilities, for example in structures subject to impact forces. The fiber has very low density and therefore results in lightweight structures. Most fiber-reinforced composite materials exhibit slightly lower strengths in compression than tension, but this is particularly true for Aramid-reinforced composites.

Like Carbon fibers, Aramid fibers have a negative coefficient of thermal expansion as well

Polyethylene (PE) fibers exhibit high tensile strengths, but lower modulus than other high performance fibers such as Aramid or Carbon. They also exhibit very low compressive strengths. They can provide very high levels of impact strength and are being used in applications such as lightweight armour plating. PE fibers have a highly negative coefficient of thermal expansion [9]

As the matrix component of the composite, a wide range of thermosetting resin systems can be used including polyester, vinylester, epoxy, phenolic and methyl methacrylates, combined with various pigments and fillers if desired [9]

The resin in an RTM process must satisfy several requirements. The resin should have low viscosity throughout the injection process but not too low. If the resin viscosity is too high, the reinforcement will have a tendency to move, the impregnation pressure will be too high and the resin will not be able to penetrate the preform properly. However if the resin viscosity is too low, there is a risk that the mold will fill before the individual fiber bundles are fully wetted and impregnated. The resin should also have low volatility, low out-gassing during cure and good fiber wetting

1.3 RTM Process Among Other Composite Manufacturing Techniques

The end properties of a composite part depend on the properties of its components, i.e. fiber reinforcement & resin matrix, but also on the method by which they are processed. The most widely recognized manufacturing methods to date for processing composites are summarized in Figure 1.7.

The major advantage of RTM is the separation of the molding process from the design of the fiber architecture, compared to the other polymer composite manufacturing techniques. Having the fiber preform stage separate from the injection and cure stages, enables the designer to create uniquely tailored material to fit precisely a specific demand profile. A variety of fiber types and forms can be combined for this purpose.

POLYMERIC MATRIX COMPOSITES MANUFACTURING

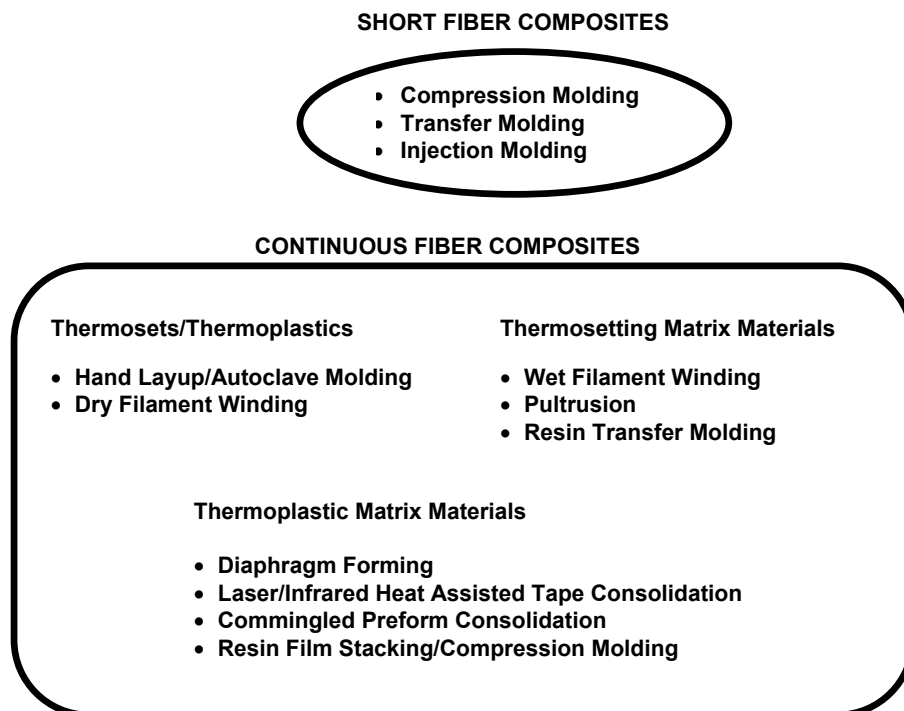


Figure 1.7 Composite manufacturing methods [1].

Resin Transfer Molding performs well in part microstructure control complexity, compared to processes like injection molding and compression molding. Other benefits include low capital investment, relatively inexpensive dry preforms (compared to prepreg material); that can be stored at room temperature. Production of relatively thick, near net-shape parts, eliminates most post-fabrication work. RTM also yields dimensionally accurate complex parts with good surface detail and delivers a smooth surface finish on all exposed surfaces. It is possible to place inserts inside the preform before the mold is closed, allowing the RTM process to accommodate core materials

and integrate "molded in" fittings and other hardware into the part structure during the molding process. Moreover, void content on RTM parts is comparatively low, measuring in the 0 to 2 percent range [10].

A major distinction of each composite fabrication technique lies in its suitability for the production of short fiber or continuous fiber composites. Within this division, further classifications can be imposed based on whether the method is used for the manufacturing of thermosetting matrix composites, thermoplastic composites, or both. Short fiber composites are typically manufactured using either a compression molding process with sheet molding compound or bulk molding compound, a transfer molding process, or an injection molding process. These processes have been used to make both thermoset and thermoplastic composite parts.

In contrast to RTM, where resin and catalyst are premixed prior to injection into the mold, reaction injection molding RIM injects a rapid-curing resin and a catalyst into the mold in two separate streams; mixing and the resultant chemical reaction both occur in the mold at a very fast pace. In a reinforced RIM process, the reinforcement (typically chopped fibers or flakes) is added to the liquid chemical systems. In such a process, high injection pressure is needed because of the high reactivity of the resin system for short processing-cycle times. RIM is especially used in the automotive industry for high-volume, low-performance composite applications (e.g. spare tire covers, bumper beams, satellite antennas, etc.). However; RTM is used for obtaining more accurate part dimensions and good surface quality parts like the front panel of automobile body of Figure 1.2. In addition, RTM only employs continuous fiber reinforcement.

Although short fiber composites have been shown to have many industrial applications, continuous fiber composites are demanded for high performance structural applications. These composites can only be manufactured by hand lay-up followed by autoclave curing, compression molding, wet filament winding, pultrusion or RTM.

Traditional composite manufacturing techniques such as hand lay-up are slow and labor intensive and such processes are only suitable to relatively simple geometries. Comparatively complex shapes can be made efficiently in RTM with production times 5–20 times shorter and with better surface definition. In addition, RTM is a closed mold process and volatile emissions during processing is lower than open mold processes such as hand lay-up.

The pultrusion process is used in the fabrication of continuous fiber composite parts that can only have constant cross-section profiles. The process is continuous, fast and part length variations are limited to shipping capabilities. In contrast, RTM can be used to mold complex three-dimensional shapes. The initial capital investment for pultrusion is generally higher than filament winding or hand lay up processes. Common pultruded parts are solid rods, hollow tubes, flat sheets and various types of beams including angles, channels, hat-sectioned and wide-flanged beams [10].

The filament winding process is used in the fabrication of tubular composite parts. Typical examples include storage tanks, electrical conduit, and composite tanks, rocket engine cases, nose cones of missiles. Filament winding process is used for high-volume production at golf club shafts, fishing rods, pipe, and pressure vessels. The geometry of the parts that can be manufactured is limited mostly to parts that are symmetric about one axis [10].

Of all the continuous fiber reinforced composite manufacturing techniques, only RTM is capable of producing highly complex geometry parts. RTM has the potential to arise as a rapid, automated manufacturing technique for producing large, complex, high performance structures with good surface finish. In addition, RTM allows for part design flexibility and large number of components can be integrated into a single part during the process.

1.4 The Need for Modeling in RTM

RTM is a highly complex process with large number of processing variables and with complex flow behavior during resin impregnation and cure. In order to obtain a cost-effective, repeatable process, it needs to be optimized for the determination of appropriate process parameters that would yield the desired properties in the end part.

In designing an RTM process for manufacturing a specific product, an experimental process optimization based on a trial-and-error approach can prove quite costly. The fiber, resin and mold material are relatively expensive. In addition, the production of the mold takes long time at appreciable cost. As a result, numerical process simulation tools that can be used in process optimization have been developed, are being improvement and have been in use for the past 10-20 years. These tools, when accurate, can reduce the production design costs and time to market, considerably.

Various two and three-dimensional flow models have been developed to simulate the resin impregnation processes. Simulations may or may not include all process stages such as heating of the fibers, resin injection and resin curing. Simulations can be used for optimizing mold features such as location of injection gates and venting ports, as well as for eliminating dry spots, calculating and reducing injection times. Mold filling simulations programs also yield information about optimum processing parameters such as resin injection pressure and flow rate, resin/mold temperature.

1.5 Scope of the Thesis Study

In this study, an existing resin transfer molding computer program is employed to simulate various RTM impregnation configurations and is modified by developing additional capabilities for more complicated RTM scenarios. The computer program has been developed over about 15 years involving several graduate studies, each contributing to various aspects of the process. It is written in FORTRAN and presently, is composed of about

20 000 lines. The program (in its full form) is capable of simulating not only the RTM process, but also injection molding, reaction injection molding, structural reaction injection molding and whisker reinforced injection molding as well as particle filtration.

Presently, the program is capable of simulating 2-D resin flow through orthotropic performs in complex mold geometries with single gates. The current work adds to the program non-homogenous perform impregnation capability (both in fiber volume fraction and permeability) as well as double gate injection simulation capability.

The thesis is presented in the following manner:

Chapter 1 (the current chapter) presented the process description of resin transfer molding along with material properties, application. The reasons behind the development of RTM simulation were also presented here.

Chapter 2 presents a literature survey on various RTM models based on Darcy's law, after which the current RTM model is explained. The stream function-Darcy law governing equation formulation and boundary conditions for the impregnation model in the current program are derived and explained.

Chapter 3 presents the numerical implementation and solution of the RTM model of Chapter 2. The governing equation and boundary conditions are transformed to the regular computational domain by a boundary-fitted coordinate system transformation. Elliptic grid generation is employed to generate the mesh needed for numerical solution. Finite difference discretization along with successive over relaxation method are used to solve the problem for stream function. The procedures of obtaining the remaining flow parameters (velocity, pressure, etc.) are described. The last part of the chapter presents the numerical implementation of double gate resin injection simulation.

Chapter 4 presents various RTM configuration simulations based on the program and its modifications. A one-dimensional impregnation parametric study is performed initially, to investigate the effect of various process parameters. The results are also compared with one-dimensional resin impregnation analytical solution. Two-dimensional resin impregnation simulations for irregular mold geometry are presented and compared with actual impregnation results from an experiment. Simulations are further presented for various process parameter configurations in two-dimensional impregnation and discussed. Two-dimensional resin impregnation in various non-homogeneous fiber preforms, which is a capability developed as part of the current work, is presented. The last part of the chapter presents the results of the double gate resin injection simulation in irregular two-dimensional molds.

Finally, Chapter 5 presents the conclusions of this study.

CHAPTER 2

RESIN TRANSFER MOLDING MODELING

2.1 Literature Review of Darcy Type Flow Simulations

Modeling of the RTM process is a challenging task. There are various stages of the process such as resin injection, resin cure, demolding and removing parts. Figure 2.1 depicts a typical resin impregnation process. The resin flow within the mold cavity can be complicated: the resin impregnates (in most cases) a tightly packed fibrous perform (flow through porous medium); the shape of the mold cavity can be quite complicated; a continuously evolving flow domain with a free surface exists, rendering the flow geometry further complex.

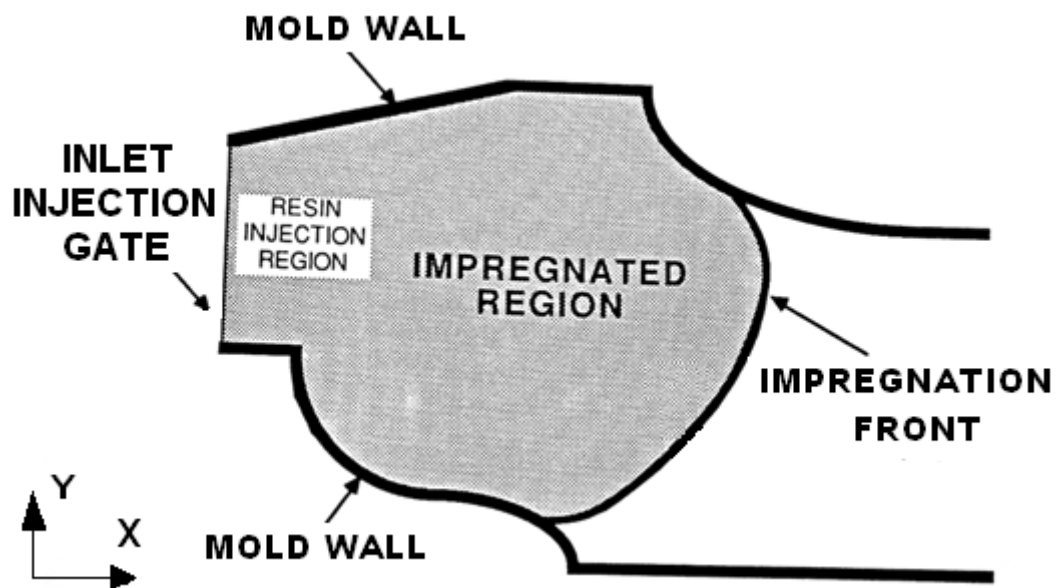


Figure 2.1 A typical impregnation process in mold space [1].

The resin may or may not behave as a Newtonian fluid. The flow is mostly two-dimensional due to small part thickness; however, three-dimensional effects may be important at some configurations. The flow proceeds through

a fibrous region, which must also be characterized, usually in terms of permeability of the domain to incoming resin flow and fiber volume fraction. The small air pockets within fiber tows (bundles) in the preforms are called micropores and the more open regions outside them are called macropores. Thus there is a flow at two scales in the fibrous preform: the global motion of resin in macropores and simultaneously, the impregnation of micropores within fiber bundles. Under normal RTM conditions, the macropore front moves ahead of the micropore front [11]. Since fibrous preforms used in RTM are dry, the mold filling stage is an unsaturated flow process. So it is possible to distinguish two different regions wetted by the resin as described in Figure 2.2

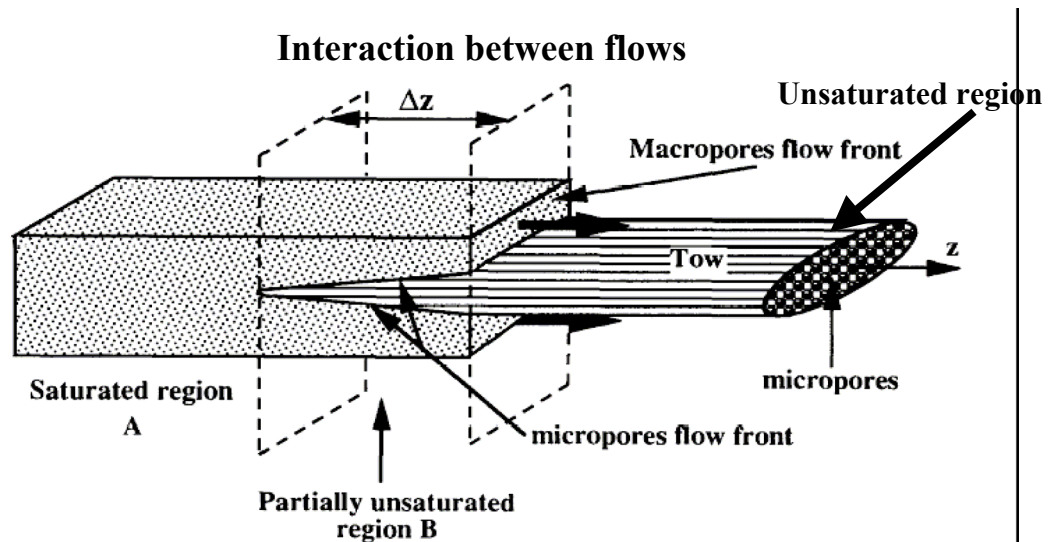


Figure 2.2 Different regions involved in the impregnation of a fiber tow bundle embedded in a medium of higher permeability [11].

- A fully saturated region (A) far behind the macropore flow front
- A partially unsaturated region (B) close to the macropore flow front. In this area a transient impregnation process takes place during which micropores are filled by resin.

In modeling studies, the flow of resin through a fiber preform is usually treated as macroscopic flow in a porous medium. The most frequently used approach in the composites field to model the macroscopic resin impregnation of the fiber preforms in RTM is Darcy's law [12] expressed in the following form for a porous medium by

$$\bar{V} = -\frac{1}{\mu} \underline{K} \cdot \nabla P \quad (2.1)$$

where \bar{V} the superficial resin velocity within the preform, P is the flow pressure, μ is the resin viscosity and \underline{K} is a tensor that depicts the directional permeability. In Darcy's model, inertial effects are negligible. This relationship is often applied to determine the permeability tensor of heterogeneous preforms from experimental measurements.

The superficial velocity is not actual resin velocity though the fiber preform. The relation between the superficial and actual velocity are given as

$$V_{actual} = \frac{V}{\varepsilon} = \frac{V}{1 - v_f} \quad (2.2)$$

where V_{actual} is the actual velocity, ε is the preform porosity and v_f is the fiber volume fraction in the mold.

Coulter [1] presented a resin impregnation model based on two-dimensional, isothermal Darcy flow. Boundary fitted coordinate systems in conjunction with the finite difference method were employed to track the motion of the flow front into planar cavities of mildly complex geometry. A result was presented for Newtonian fluids and for isotropic as well as orthotropic preforms [13]. This work was later extended by Aoyagi [14, 15] to non isothermal, reactive flows as encountered in structural reaction injection molding (SRIM) process. SRIM is a subclass of RTM and characterized by a smaller cure time which is of the order of the fill time. Detailed results regarding the flow front positions were presented.

While the above studies focused on the accurate description of the details of the flow field, other researchers put more emphasis on geometric flexibility.

Bruschke and Advani [16] used a control volume/ finite element method to numerically analyze isothermal Darcy flow in complex three dimensional shapes such as a cross-member of a passenger van. A locally two-dimensional flow model was employed, valid for thin walled, shell like structures. The another application is that isothermal, two-dimensional Darcy flow has also been solved for using control volume/ finite element techniques by Fracchia and Tucker [17].

The finite element analysis is used for Darcy flow in axisymmetric parts such as pipes. The flow front is not tracking by the use of control volumes, but by the addition of nodes at every time step. This is an example of the use of finite element in conjunction with boundary fitted coordinates systems for mold filling simulations that is presented by Chan and Hwang [18].

2.2 Current Model

The current study uses and updates a custom computer program, written in FORTRAN, to simulate various RTM scenarios. This program has been developed over the years by various researchers and includes a many of process simulations other than RTM as well. In the current research, the aim is to simulate various RTM scenarios with the existing capabilities as well as to develop and add multiple gate injection capability to the program.

The resin impregnation is formulated by assuming two-dimensional, quasi-steady, isothermal flow of a Newtonian viscous fluid through a porous medium. The fiber preform is characterized by a macroscopic permeability. The permeability can be anisotropic in the simulations. The preform is assumed to be orthotropic; however, the principal permeability axes are made to coincide with the Cartesian coordinate system during formulations.

2.2.1 Formulation of the Problem

The resin flow through the mold was depicted earlier in Figure 2.1. The macroscopic flow of resin through the fiber preform is modeled by Darcy's law as

$$\vec{V} = -\frac{\underline{\underline{K}}}{\mu} \cdot \nabla P \quad (2.3)$$

$\underline{\underline{K}}$ is the symmetric permeability tensor which, in Cartesian coordinates, can be written in three dimensions as

$$\underline{\underline{K}} = \begin{pmatrix} K_{xx} & K_{xy} & K_{xz} \\ K_{xy} & K_{yy} & K_{yz} \\ K_{xz} & K_{yz} & K_{zz} \end{pmatrix} \quad (2.4)$$

For a two-dimensional flow, such as resin impregnation where the mold cavity thickness is much smaller than planar dimensions, the permeability tensor reduces to

$$\underline{\underline{K}} = \begin{pmatrix} K_{xx} & K_{xy} \\ K_{yx} & K_{yy} \end{pmatrix} \quad (2.5)$$

The x and y direction can be seen in Figure 2.1. For two-dimensional flow, Darcy's Law can be written explicitly

$$u = -\frac{1}{\mu} \left(K_{xx} \frac{\partial P}{\partial x} + K_{xy} \frac{\partial P}{\partial y} \right) \quad (2.6)$$

$$v = -\frac{1}{\mu} \left(K_{yx} \frac{\partial P}{\partial x} + K_{yy} \frac{\partial P}{\partial y} \right) \quad (2.7)$$

In the formulation, u and v are the components of velocity in the x and y directions, respectively. Last forty years of anisotropic porous media research shows that fabric preforms in the RTM processes exhibit orthotropic behavior, i.e. they have three mutually orthogonal principle axes [1]. By making the permeability principal axes coincide with Cartesian coordinate system, the permeability tensor of the equation (2.5) reduces to

$$\underline{\underline{K}} = \begin{pmatrix} K_{xx} & 0 \\ 0 & K_{yy} \end{pmatrix} \quad (2.8)$$

Then, the formulations of equations (2.6) and (2.7) become

$$u = -\frac{K_{xx}}{\mu} \frac{\partial P}{\partial x} \quad (2.9)$$

$$v = -\frac{K_{yy}}{\mu} \frac{\partial P}{\partial y} \quad (2.10)$$

or

$$\frac{\partial P}{\partial x} + \frac{\mu}{K_{xx}} u = 0 \quad (2.11)$$

$$\frac{\partial P}{\partial y} + \frac{\mu}{K_{yy}} v = 0 \quad (2.12)$$

In the above equations, the preform permeabilities in the x and y directions are represented by K_{xx} and K_{yy} . These quantities are usually obtained from simple one-dimensional impregnation experiments, which are then used in complex RTM simulations. The continuity equation is introduced through streamfunction formulations as

$$u = \frac{\partial \psi}{\partial y} \quad (2.13)$$

$$v = -\frac{\partial \psi}{\partial x} \quad (2.14)$$

Darcy's Law (equations (2.11) and (2.12)) and the continuity equation (equations (2.13) and (2.14)) can be combined into a single equation by eliminating the pressure in equations (2.11) and (2.12) by cross differentiation as

$$\begin{aligned} & \frac{\mu}{K_{yy}} \frac{\partial \psi^2}{\partial x^2} + \frac{\mu}{K_{xx}} \frac{\partial \psi^2}{\partial y^2} + \left[\frac{1}{K_{xx}} \frac{\partial \mu}{\partial y} - \frac{\mu}{K_{xx}^2} \left(\frac{\partial K_{xx}}{\partial y} \right) \right] \frac{\partial \psi}{\partial y} \\ & + \left[\frac{1}{K_{yy}} \frac{\partial \mu}{\partial x} - \frac{\mu}{K_{yy}^2} \left(\frac{\partial K_{yy}}{\partial x} \right) \right] \frac{\partial \psi}{\partial x} = 0 \end{aligned} \quad (2.15)$$

Equation (2.15) is the governing equation for the two-dimensional, isothermal, quasi-steady flow of a Newtonian resin through an orthotropic preform having its principle axes aligned with an x-y Cartesian coordinate system.

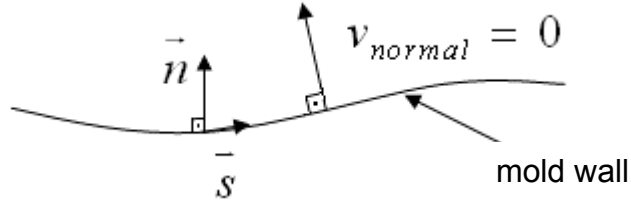
2.2.2 Boundary Conditions

Due to the elliptic nature of the stream function equation (2.15) boundary conditions need to be specified along the entire boundary of the flow domain. There are three types of boundaries in the current problem:

- The edges of the mold in the x-y plane that are in contact with the polymer (mold walls – solid boundary)
- The advancing resin flow front (free surface)
- Resin inlet locations (gates) in the mold

A stream function condition must be specified on all the boundaries. The edges of the mold are impermeable so the velocity normal to the mold edge is zero. The stream function-velocity relation (equations (2.13) and (2.14)) implies that the derivative of stream function in the direction normal to the boundary must be zero. However, the velocity tangent to the edge of the mold is not necessarily zero [19].

The current model assumes that the fluid “slips” along the edge of the mold, so every wetted edge of the mold becomes a stream line. The mold wall boundary conditions are depicted in Figure 2.3.



The two boundary conditions where the resin contacts the edge of the mold are

$$\Psi_{\text{SIDE WALLS}} = \text{constant} \quad (2.16)$$

$$\frac{\partial \psi}{\partial s} = v_{\text{normal}} = 0 \quad (2.17)$$

Figure 2.3 Mold wall boundary condition

Along the resin flow front (free surface), the pressure is zero gage. Because of positioning of the air vents, the resin replaces air as it fills the cavity and the resin front remains at atmospheric pressure (provided there is no build-up of air pressure due to the inadequate venting of the mold).

Since the flow front is an isobar, the stream lines are perpendicular to the flow front by the virtue of Darcy’s Law. The motion of a fluid particle along the flow front is normal to the curve describing the position of the front [20].

At the flow front, the pressure is zero gage and from force balance, it can be shown that the shear stress, τ_{nt} on the resin front surface is also zero.

If an infinitesimal control surface denoted by $d\vec{A}$ ($\vec{n}dA$) that lies on the resin front is considered, then $d\vec{A}$ is parallel to $\vec{V}_{flow\ front}$ in the Figure 2.4. Since τ_{nt} lies in the plane of $d\vec{A}$, τ_{nt} is perpendicular to $\vec{V}_{flow\ front}$ and its value is taken as zero on the flow front. This condition can be stated as [1]

$$\tau_{nt} = \mu \left[\left(\frac{\partial u}{\partial x} - \frac{\partial v}{\partial y} \right) \sin 2\theta - \left(\frac{\partial u}{\partial y} + \frac{\partial v}{\partial x} \right) \cos 2\theta \right] = 0 \quad (2.18)$$

where θ represents the angle between the outward normal at a point along the free surface and the x-axis as shown in Figure 2.4. Equation (2.18) can be expressed in terms of stream function through equations (2.13) and (2.14), which yield a condition for stream function on the flow front, as required by the problem formulation.

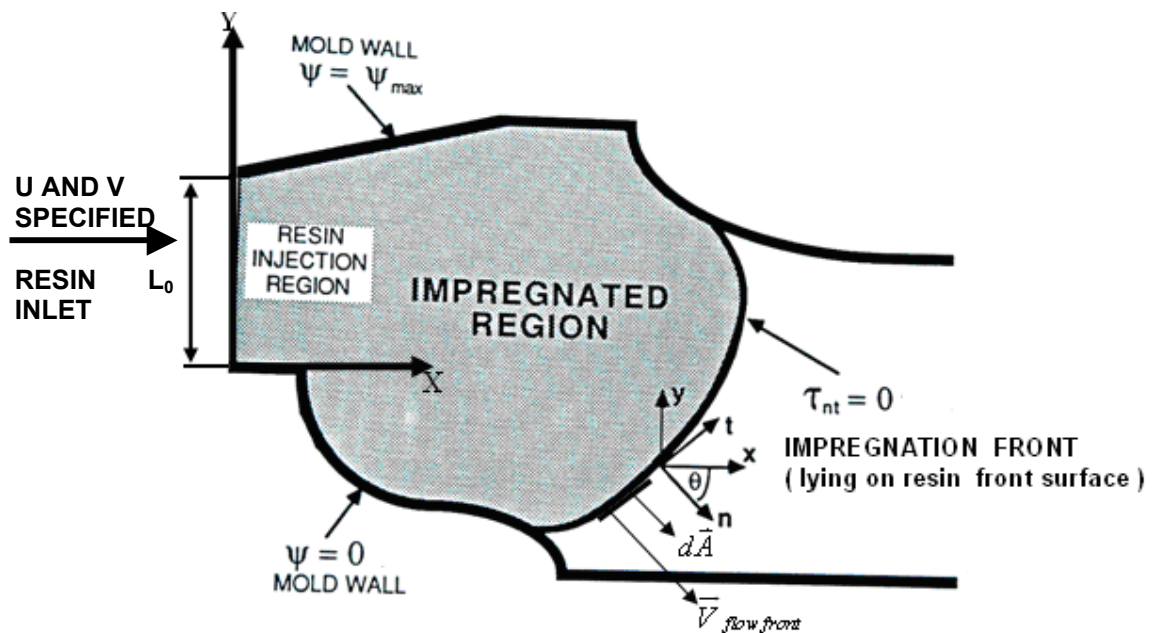


Figure 2.4 Boundary conditions [1]

The boundary condition for the resin inlet location depends on the inlet gate. A gate has either a known pressure or a known flow rate, which may vary

with time. In the current formulation, the inlet condition is prescribed flow rate. This is input as constant u and v inlet velocities. Usually, the gate is quite narrow, and the flow rate can be taken as constant across its width. The stream function values can be found from

$$\psi = \int u dy - \int v dx \quad (2.19)$$

Choosing the y -axis to coincide with the gate simplifies the gate ψ distribution calculation (see Figure 2.4). The injection is normal to the gate. Therefore, there is no v velocity and the stream function distribution along the injection gate can be determined from a more specific form of equation (2.19) as

$$\psi_{gate}(0, y) - \psi_{gate}(0, 0) = \int_0^y u_{gate}(0, y) dy \quad (2.20)$$

$$\psi_{gate}(y) - \psi_{gate, y=0} = \bar{u}_{inlet} \cdot y \quad (2.21)$$

where \bar{u}_{inlet} is the constant inlet velocity (along x - direction) with

$$\bar{u}_{inlet} = \frac{u_o}{\varepsilon} \quad (2.22)$$

where ε is the preform porosity given as

$$\varepsilon = 1 - v_f \quad (2.23)$$

Stream function along the gate is

$$\psi_{gate}(y) = \frac{u_0}{\varepsilon} y \quad (2.24)$$

with $\psi_{gate, y=0} = 0$ (as seen in Figure 2.4). Maximum change of stream function along the gate is

$$\Delta \psi_{max} = \psi_{gate}(L_0) - \psi_{gate, y=0} = \frac{u_0}{\varepsilon} L_0 \quad (2.25)$$

where L_0 is the width of the gate. Scaling ψ by $\Delta \psi_{max}$,

$$\psi_{gate}^* = \frac{\psi_{gate}}{\Delta\psi_{max}} = \frac{u_0}{\varepsilon} y \frac{1}{\frac{u_0}{\varepsilon} L_0} = \frac{y}{L_0} \quad (2.26)$$

The scaled stream function ψ_{gate}^* varies between 0 and 1 as

$$\psi_{gate}^* = \frac{y}{L_0} \quad (2.27)$$

The three types of boundary conditions are depicted in an impregnating flow domain sketch in Figure 2.4.

2.3 Physical Significant of Process Parameters

Preform permeability is a measure of how “easy” it is for the fluid (resin) to impregnate the porous domain (fiber preform). If the value of the permeability is low, then the process requires higher injection pressure (more “difficult”). Thus, a tightly woven preform can result in a low permeability which can complicate the process. On the other hand, a tightly woven preform yields a high fiber volume fraction in the mold cavity (and hence, in the part). This is a favorable trait as the part becomes stronger with higher fiber content. Therefore, the processing needs and part design requirements must be carefully balanced for an optimum (compromised) outcome.

The fiber volume fraction values vary between 0 and 1. When there is no fiber, the fiber volume fraction, v_f , is 0. When the mold cavity is completely (and theoretically) filled with fibers, v_f would be 1. In production, for high performance composites, v_f is around 0.5. The permeability of the preform is affected by the fiber volume fraction, as discussed in the previous paragraph.

A preform can also have anisotropic permeability, which means that the fluid can impregnate the preform more “easily” in a certain direction than the other directions. Figure 2.5 depicts a permeability experiment for an anisotropic preform. In such an experiment, the permeability is determined by applying

the changing injection pressure and the measured flow front locations (and the calculated impregnation velocity) to a macroscopic model (usually Darcy's). In the figure, the fluid is seen to be moving faster in x direction than other directions as it encounters the least resistance in x direction. Therefore, the highest permeability is in x direction (i.e. K_{xx} is the largest permeability). The smallest permeability lies along y direction, i.e. K_{yy} . It should be noted that in this figure the "principal" permeability directions (directions along which permeability is the smallest and the largest) coincide with the x-y coordinate axes.

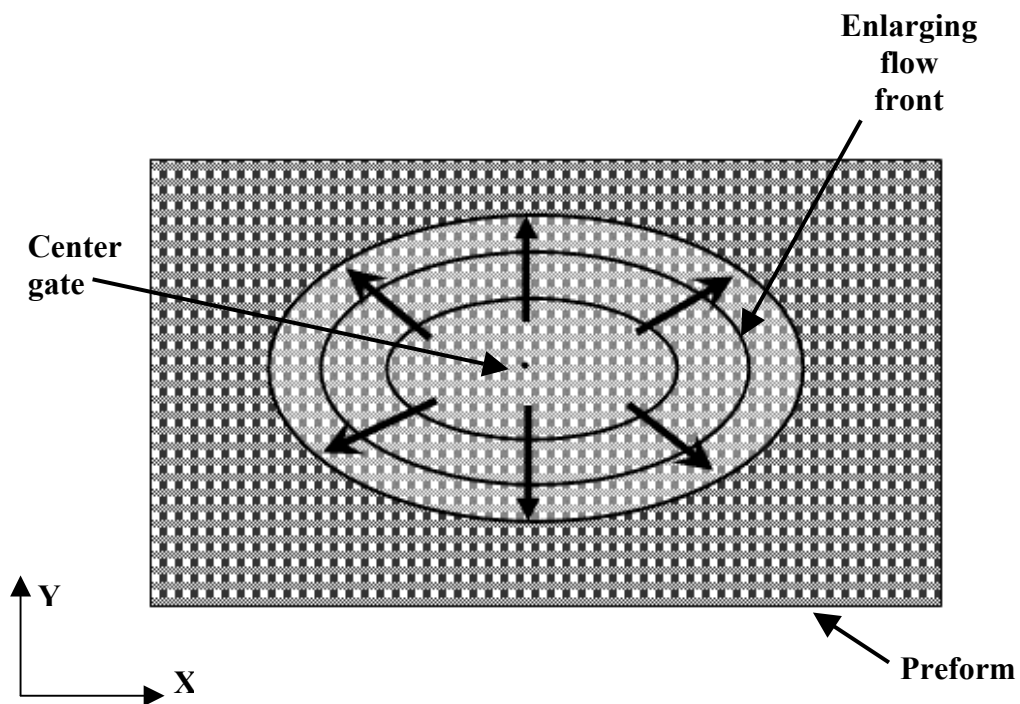


Figure 2.5 Resin flow fronts spreading out from a center gate as the resin fills an anisotropic preform.

The resins that are used in RTM are thermosetting resins with generally low viscosity values. Even though the resins are not commonly Newtonian, the shear rates associated with RTM process, are usually low. At low shear rates, the resin behavior resembles that of Newtonian fluids. Therefore, in modeling RTM impregnation, Newtonian fluid approximation for the resin is often used.

CHAPTER 3

NUMERICAL IMPLEMENTATION AND SOLUTION

3.1 Transformation of Governing Equation and Boundary Conditions to Computational Domain from Physical Domain

In the simulated RTM process; the filling stage consists of the impregnation of resin into a fibrous preform network according to the conditions of prescribed injection rate.

The modeling of this process was presented in the previous chapter. In this analysis, the impregnation was assumed to occur in a two-dimensional flow field. This two-dimensional flow field assumption becomes realistic because most RTM parts are typically characterized by a dimension (usually the thickness) which is much smaller, relative to the overall part size. The processes are assumed to be isothermal as curing becomes prominent after the cavity is filled and the resin systems are taken to be Newtonian, which is acceptable for most resins as they are low viscosity and the shear rates are small.

For a two-dimensional, isothermal resin impregnation process, the Darcy-based model that combined Darcy's equation with continuity was presented in Chapter 2. The derived model was based on steady-state assumption. The resin impregnation process is an unsteady process in which flow domain is continuously moving and changing its shape. However, during the modeling phase, the flow is assumed to achieve a quasi-steady condition at each progression (movement) of the flow front, due to the relatively slow nature of the process.

The governing equation is valid in the flow domain. However the flow domain does not have a regular geometry as its shape changes continuously due to

the moving flow front. This is a condition observed in all mold cavity shapes, including regular geometries. This prevents the analytical solution of the problem for most cases. Numerical solution requires discretization of the governing equation and thus, the solution domain. For irregular shaped domains, the nature of discretization can affect the solution accuracy greatly.

In the current problem, the geometrical complexity of the flow domain is the major computational challenge. The location of the impregnation flow front is not known in advance and the irregular shape of the mold walls along with the unknown location of the flow front are the main causes of this geometric complexity.

3.1.1 Boundary-Fitted Coordinate System and Elliptic Grid Generation

In order to handle the geometrical complexity of the flow domain during numerical discretization, boundary-fitted coordinate system (BFCS) is employed. This technique has been developed and used by various researchers previously [21-23].

The main idea of this technique lies in mapping the irregular physical problem (flow) domain (x, y) into a regular computational domain (ζ, η) for two-dimensional flow, through an appropriate grid (mesh) generation that fits to the physical domain. The transformation is depicted in Figure 3.1. The four irregular boundaries of the flow domain (2 mold walls, 1 injection gate and 1 resin flow front) are marked on the figure. The computational domain has regular grids and gridlines intersecting normally. In the physical (flow) domain, the gridlines become distorted as seen in Figure 3.1. The governing equation and boundary condition are to be transformed to and solved in the computational regular domain.

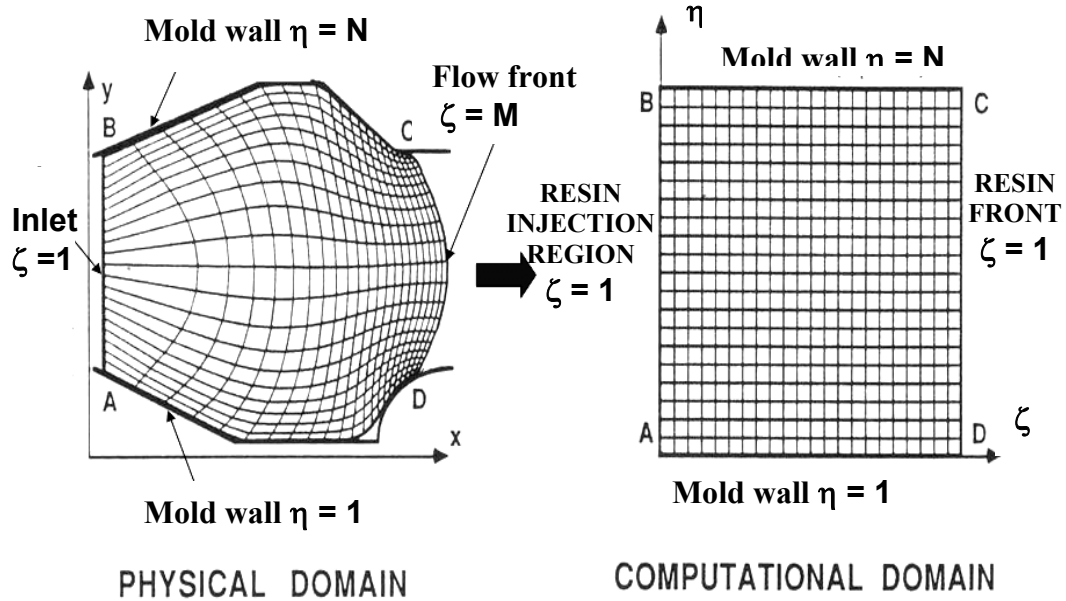


Figure 3.1 Physical and computational domains of a boundary fitted coordinate system transformation applied to a sample resin transfer molding process. [20]

In the transformation method, the physical and computational coordinates are related to one another by algebraic relations $\zeta(x, y)$, $\eta(x, y)$. The relations between the physical and the computational coordinates are obtained through the solution of differential equations, which can be elliptic, hyperbolic or parabolic. In the current study, elliptic grid generation is used. The current code is also capable of grid concentration through the nonhomogenous elliptic equation, i.e. the Poisson equation.

The generated grids are used in a finite difference discretization scheme. The nodal spacing in computational space does not affect the solution, so for convenience, the node spacing in computational space $\Delta\zeta$ and $\Delta\eta$, are taken to be unity, i.e. $\Delta\zeta=\Delta\eta=1$. The number of nodes in the ζ and η directions are selected in the program, which defines the size of the computational domain. The grid generation process calculates the physical (x-y) coordinates of each node in the computational mesh.

Here, a set of partial differential equations describes the mapping between the physical and the computational domain. In principle, the grid generation equations can be of any type, parabolic, hyperbolic or elliptic. Elliptic grid

generators are most often used because they distribute the nodes smoothly in physical space and effectively handle boundary discontinuities and singularities [20-23]. The Poisson-type elliptic grid generation equations for a two dimensional problems are

$$\frac{\partial^2 \xi}{\partial x^2} + \frac{\partial^2 \xi}{\partial y^2} = P(\xi, \eta) \quad (3.1)$$

$$\frac{\partial^2 \eta}{\partial x^2} + \frac{\partial^2 \eta}{\partial y^2} = Q(\xi, \eta) \quad (3.2)$$

where (x, y) are the physical coordinates and (ξ, η) are the computational coordinates. P and Q are the grid control functions that allow the user to manipulate the distribution of the nodes in the physical domain. When transforming into a Cartesian computational domain, setting P and Q equal to zero produces a mesh with uniformly distributed nodes. Equations (3.1) and (3.2) are solved by interchanging the dependent and independent variables, so that the calculation produces the (x, y) coordinates for each ξ, η node in the mesh. The inversion operation is detailed in Appendix A. The equivalent equations with the interchanged variables are

$$\alpha x_{\xi\xi} - 2\beta x_{\xi\eta} + \gamma x_{\eta\eta} + J^2 (Px_{\xi} + Qx_{\eta}) = 0 \quad (3.3)$$

$$\alpha y_{\xi\xi} - 2\beta y_{\xi\eta} + \gamma y_{\eta\eta} + J^2 (Py_{\xi} + Qy_{\eta}) = 0 \quad (3.4)$$

where J is the Jacobian of the coordinate transformation given as

$$J = x_{\xi}y_{\eta} - y_{\xi}x_{\eta} \quad (3.5)$$

and α, β and γ are the geometric coefficients of transformation defined as

$$\alpha = x_{\eta}^2 + y_{\eta}^2 \quad \beta = x_{\xi}x_{\eta} + y_{\xi}y_{\eta} \quad \gamma = x_{\xi}^2 + y_{\xi}^2 \quad (3.6)$$

The boundary values for x (ξ, η) and y (ξ, η) are known from the physical domain. Solving equations (3.3) and (3.4) numerically generates the grid

nodes $x(\zeta, \eta)$ and $y(\zeta, \eta)$. Using central difference formulas yields a coupled set of expressions which can be solved for $x_{i,j}$ and $y_{i,j}$ values at each grid node. The actual magnitude of the computational coordinates ξ and η do not enter into the calculations therefore their absolute values do not affect to the solution and the mesh increment are specified as $\Delta\xi = \Delta\eta = 1$. This choice of increments also eliminates $\Delta\xi$ and $\Delta\eta$ from the difference equations, simplifying the expressions. An iterative solution is employed to determine $x(\xi, \eta)$ and $y(\xi, \eta)$ with under-relaxation when necessary to promote convergence. Some initial guesses for the x, y coordinates can cause the Jacobian to become zero, causing a temporary singularity during the iterations in the program used in this study. This problem can be avoided by assigning a more reasonable initial distribution for the x and y variables and continuously monitoring the value of the Jacobian at each grid points.

3.1.2 Governing Equation and Boundary Conditions in the Computational Domain

The governing stream function equation and the boundary condition equations are transformed to computational domain by performing a chain rule differentiation [20]. The first derivatives in the computational domain of any variable $f(x, y)$ can be expressed as

$$f_\xi = f_x x_\xi + f_y y_\xi \quad (3.7)$$

$$f_\eta = f_x x_\eta + f_y y_\eta$$

Applying same formulations to the stream function equations yields

$$\psi_\xi = \psi_x x_\xi + \psi_y y_\xi \quad (3.8a)$$

$$\psi_\eta = \psi_x x_\eta + \psi_y y_\eta \quad (3.8b)$$

Applying Cramer's rule to invert these equations gives

$$\psi_x = \frac{1}{J} (y_\eta \psi_\xi - y_\xi \psi_\eta) \quad (3.9a)$$

$$\psi_y = \frac{1}{J} (x_\xi \psi_\eta - x_\eta \psi_\xi) \quad (3.9b)$$

where the Jacobian of the transformation is

$$J = x_\xi y_\eta - x_\eta y_\xi \quad (3.10)$$

The second derivative ψ_{xx} can be expressed as

$$\begin{aligned} \frac{\partial \psi^2}{\partial x^2} &= \frac{y_\eta^2}{J^2} \frac{\partial \psi^2}{\partial \xi^2} + \frac{y_\xi^2}{J^2} \frac{\partial \psi^2}{\partial \eta^2} - \frac{2y_\xi y_\eta}{J^2} \frac{\partial \psi^2}{\partial \xi \partial \eta} \\ &+ \frac{1}{J^2} \left[(y_\eta y_{\xi\eta} - y_\xi y_{\eta\eta}) - \frac{J_\xi}{J} y_\eta^2 + \frac{J_\eta}{J} y_\eta y_\xi \right] \frac{\partial \psi}{\partial \xi} \\ &+ \frac{1}{J^2} \left[(y_\xi y_{\xi\eta} - y_\eta y_{\xi\xi}) - \frac{J_\xi}{J} y_\xi y_\eta - \frac{J_\eta}{J} y_\xi^2 \right] \frac{\partial \psi}{\partial \eta} \end{aligned} \quad (3.11)$$

Defining

$$C_{xx\xi\xi} = \frac{1}{J^2} y_\eta^2 \quad (3.12)$$

$$C_{xx\eta\eta} = \frac{1}{J^2} y_\xi^2 \quad (3.13)$$

$$C_{xx\xi\eta} = -\frac{2y_\xi y_\eta}{J^2} \quad (3.14)$$

$$C_{xx\xi} = \frac{1}{J^2} \left[(y_\eta y_{\xi\eta} - y_\xi y_{\eta\eta}) - \frac{J_\xi}{J} y_\eta^2 + \frac{J_\eta}{J} y_\eta y_\xi \right] \quad (3.15)$$

$$C_{xx\eta} = \frac{1}{J^2} \left[(y_\xi y_{\xi\eta} - y_\eta y_{\xi\xi}) - \frac{J_\xi}{J} y_\xi y_\eta - \frac{J_\eta}{J} y_\xi^2 \right] \quad (3.16)$$

and substituting into equation (3.11) yields

$$\frac{\partial \psi^2}{\partial x^2} = C_{xx\xi\xi} \frac{\partial \psi^2}{\partial \xi^2} + C_{xx\eta\eta} \frac{\partial \psi^2}{\partial \eta^2} - C_{xx\xi\eta} \frac{\partial \psi^2}{\partial \xi \partial \eta} + C_{xx\xi} \frac{\partial \psi}{\partial \xi} + C_{xx\eta} \frac{\partial \psi}{\partial \eta} \quad (3.17)$$

Likewise

$$\frac{\partial \psi^2}{\partial y^2} = C_{yy\xi\xi} \frac{\partial \psi^2}{\partial \xi^2} + C_{yy\eta\eta} \frac{\partial \psi^2}{\partial \eta^2} - C_{yy\xi\eta} \frac{\partial \psi^2}{\partial \xi \partial \eta} + C_{yy\xi} \frac{\partial \psi}{\partial \xi} + C_{yy\eta} \frac{\partial \psi}{\partial \eta} \quad (3.18)$$

with

$$C_{yy\xi\xi} = \frac{1}{J^2} x_\eta^2 \quad (3.19)$$

$$C_{yy\eta\eta} = \frac{1}{J^2} x_\xi^2 \quad (3.20)$$

$$C_{yy\xi\eta} = -\frac{2x_\xi x_\eta}{J^2} \quad (3.21)$$

$$C_{yy\xi} = \frac{1}{J^2} \left[(x_\eta x_{\xi\eta} - x_\xi x_{\eta\eta}) - \frac{J_\xi}{J} x_\eta^2 + \frac{J_\eta}{J} x_\eta x_\xi \right] \quad (3.22)$$

$$C_{yy\eta} = \frac{1}{J^2} \left[(x_\xi x_{\xi\eta} - x_\eta x_{\xi\xi}) - \frac{J_\xi}{J} x_\xi x_\eta - \frac{J_\eta}{J} x_\xi^2 \right] \quad (3.23)$$

Defining

$$C_{y\eta} = \frac{x_\xi}{J} \quad (3.24)$$

$$C_{y\xi} = -\frac{x_\eta}{J} \quad (3.25)$$

and placing in equation (3.9) yields

$$\frac{\partial \psi}{\partial x} = C_{x\xi} \frac{\partial \psi}{\partial \xi} - C_{x\eta} \frac{\partial \psi}{\partial \eta} \quad (3.26)$$

$$\frac{\partial \psi}{\partial y} = C_{y\eta} \frac{\partial \psi}{\partial \eta} - C_{y\xi} \frac{\partial \psi}{\partial \xi} \quad (3.27)$$

with

$$C_{x\xi} = \frac{y_\eta}{J} \quad (3.28)$$

$$C_{x\eta} = -\frac{y_\xi}{J} \quad (3.29)$$

The viscosity and permeability derivatives are transformed as

$$\frac{\partial \mu}{\partial y} = \frac{1}{J} \left(\frac{\partial \mu}{\partial \eta} \frac{\partial x}{\partial \xi} - \frac{\partial \mu}{\partial \xi} \frac{\partial x}{\partial \eta} \right) \quad (3.30)$$

$$\frac{\partial K_x}{\partial y} = \frac{1}{J} \left(\frac{\partial K_x}{\partial \eta} \frac{\partial x}{\partial \xi} - \frac{\partial K_x}{\partial \xi} \frac{\partial x}{\partial \eta} \right) \quad (3.31)$$

$$\frac{\partial \mu}{\partial x} = \frac{1}{J} \left(\frac{\partial \mu}{\partial \xi} \frac{\partial y}{\partial \eta} - \frac{\partial \mu}{\partial \eta} \frac{\partial y}{\partial \xi} \right) \quad (3.32)$$

$$\frac{\partial K_y}{\partial x} = \frac{1}{J} \left(\frac{\partial K_y}{\partial \xi} \frac{\partial y}{\partial \eta} - \frac{\partial K_y}{\partial \eta} \frac{\partial y}{\partial \xi} \right) \quad (3.33)$$

Placing equation (3.17), (3.27), (3.30), (3.31), (3.32) and (3.33) in equation (2.15) turns the governing stream function equation to

$$\begin{aligned} & \frac{\mu}{K_{yy}} \left(C_{xx\xi\xi} \frac{\partial \psi^2}{\partial \xi^2} + C_{xx\eta\eta} \frac{\partial \psi^2}{\partial \eta^2} - C_{xx\xi\eta} \frac{\partial \psi^2}{\partial \xi \partial \eta} + C_{xx\xi} \frac{\partial \psi}{\partial \xi} + C_{xx\eta} \frac{\partial \psi}{\partial \eta} \right) \\ & + \frac{\mu}{K_{xy}} \left(C_{yy\xi\xi} \frac{\partial \psi^2}{\partial \xi^2} + C_{yy\eta\eta} \frac{\partial \psi^2}{\partial \eta^2} - C_{yy\xi\eta} \frac{\partial \psi^2}{\partial \xi \partial \eta} + C_{yy\xi} \frac{\partial \psi}{\partial \xi} + C_{yy\eta} \frac{\partial \psi}{\partial \eta} \right) \\ & + \left[\frac{1}{K_x} \frac{1}{J} \left(\frac{\partial \mu}{\partial \eta} \frac{\partial x}{\partial \xi} - \frac{\partial \mu}{\partial \xi} \frac{\partial x}{\partial \eta} \right) - \frac{\mu}{K_x^2} \frac{1}{J} \left(\frac{\partial K_x}{\partial \eta} \frac{\partial x}{\partial \xi} - \frac{\partial K_x}{\partial \xi} \frac{\partial x}{\partial \eta} \right) \right] \left(C_{y\eta} \frac{\partial \psi}{\partial \eta} - C_{y\xi} \frac{\partial \psi}{\partial \xi} \right) \quad (3.34) \\ & + \left[\frac{1}{K_y} \frac{1}{J} \left(\frac{\partial \mu}{\partial \xi} \frac{\partial y}{\partial \eta} - \frac{\partial \mu}{\partial \eta} \frac{\partial y}{\partial \xi} \right) - \frac{\mu}{K_y^2} \frac{1}{J} \left(\frac{\partial K_y}{\partial \xi} \frac{\partial y}{\partial \eta} - \frac{\partial K_y}{\partial \eta} \frac{\partial y}{\partial \xi} \right) \right] \left(C_{x\xi} \frac{\partial \psi}{\partial \xi} - C_{x\eta} \frac{\partial \psi}{\partial \eta} \right) \\ & = 0 \end{aligned}$$

Defining

$$D_{11} = \frac{K_{yy}}{K_{xy}} \quad (3.35a)$$

$$D_{12} = \frac{K_y}{J\mu K_x} \left[\frac{\partial \mu}{\partial \eta} \frac{\partial x}{\partial \xi} - \frac{\partial \mu}{\partial \xi} \frac{\partial x}{\partial \eta} \right] - \frac{K_y}{JK_x^2} \left[\frac{\partial K_x}{\partial \eta} \frac{\partial x}{\partial \xi} - \frac{\partial K_x}{\partial \xi} \frac{\partial x}{\partial \eta} \right] \quad (3.35b)$$

$$D_{13} = \frac{1}{J\mu} \left[\frac{\partial \mu}{\partial \xi} \frac{\partial y}{\partial \eta} - \frac{\partial \mu}{\partial \eta} \frac{\partial y}{\partial \xi} \right] - \frac{1}{JK_y} \left[\frac{\partial K_y}{\partial \xi} \frac{\partial y}{\partial \eta} - \frac{\partial K_y}{\partial \eta} \frac{\partial y}{\partial \xi} \right] \quad (3.35c)$$

and substituting into equation (3.34) and rearranging yields the final form of the transformed governing equation as

$$\begin{aligned} & \left[C_{xx\xi} + D_{11}C_{yy\xi} - D_{12}C_{y\xi} + D_{13}C_{x\xi} \right] \frac{\partial \psi}{\partial \xi} \\ & + \left[C_{xx\eta} + D_{11}C_{yy\eta} + D_{12}C_{y\eta} - D_{13}C_{x\eta} \right] \frac{\partial \psi}{\partial \eta} \\ & + \left[C_{xx\xi\xi} + D_{11}C_{yy\xi\xi} \right] \frac{\partial \psi^2}{\partial \xi^2} + \left[C_{xx\eta\eta} + D_{11}C_{yy\eta\eta} \right] \frac{\partial \psi^2}{\partial \eta^2} \\ & - \left[C_{xx\xi\eta} + D_{11}C_{yy\xi\eta} \right] \frac{\partial \psi^2}{\partial \xi \partial \eta} = 0 \end{aligned} \quad (3.36)$$

The boundary conditions were derived in Chapter 2 previously. The flow domain boundary conditions are depicted in Figure 3.2.

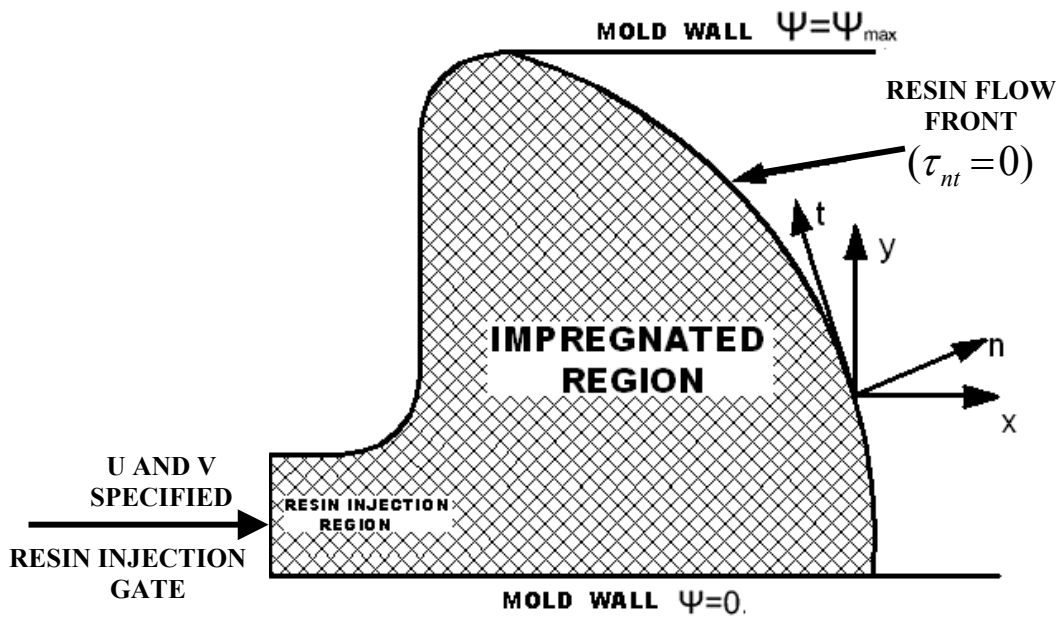


Figure 3.2 Boundary conditions

Solid (Mold Wall) Boundaries: Along the mold walls the stream function is set to constant values. Along the lower wall this constant stream function value is set to zero. The upper mold wall is assigned a constant stream function value of one as

$$\psi_{Lower-wall} = 0 \quad (3.37a)$$

$$\psi_{Upper-wall} = 1 \quad (3.37b)$$

Resin Inlet Boundary (Gate): Along the inlet region to the flow field, the stream function values are related to the specified constant u and v velocities. At the inlet gate, the distribution of stream function obtained via equation (2.26) is adapted directly on the computational ξ and η nodes.

Resin Impregnation Front: On all free surface nodal point excluding the liquid-solid contact points at the mold-wall, shear stress vanishes was expressed in Chapter 2 in equation (2.17). This condition was expressed in Chapter 2 in equation (2.18). Placing the stream function definition into equation (2.18) yields

$$\tau = \frac{\partial^2 \psi}{\partial x^2} \cos 2\theta + 2 \sin 2\theta \frac{\partial^2 \psi}{\partial y \partial x} - \cos 2\theta \frac{\partial^2 \psi}{\partial y^2} = 0 \quad (3.38)$$

The second term in equation (3.38) is

$$\begin{aligned} \frac{\partial}{\partial y} \psi_x &= \frac{1}{J^2} \left[J \frac{\partial}{\partial y} (y_\eta \psi_\xi - y_\xi \psi_\eta) - (y_\eta \psi_\xi - y_\xi \psi_\eta) \frac{\partial J}{\partial y} \right] \\ &= \left(-\frac{x_\eta y_\eta}{J^2} \right) \psi_{\xi\xi} + \left(-\frac{x_\xi y_\xi}{J^2} \right) \psi_{\eta\eta} + \left(\frac{x_\xi y_\eta + x_\eta y_\xi}{J^2} \right) \psi_{\xi\eta} \\ &+ \frac{1}{J^2} \left[(x_\xi y_{\eta\eta} - x_\eta y_{\xi\eta}) - \frac{J_\xi}{J} y_\eta x_\eta + \frac{J_\eta}{J} x_\xi y_\eta \right] \psi_\xi \\ &+ \frac{1}{J^2} \left[(x_\eta y_{\xi\xi} - x_\xi y_{\xi\eta}) - \frac{J_\eta}{J} y_\xi x_\xi - \frac{J_\xi}{J} x_\eta y_\xi \right] \psi_\eta \end{aligned} \quad (3.39)$$

Using the coefficients defined in equation (3.19) to (3.23) equation (3.39) is written in simpler form as;

$$\frac{\partial \psi}{\partial y \partial x} = C_{XY\xi\xi} \frac{\partial \psi^2}{\partial \xi^2} + C_{YY\eta\eta} \frac{\partial \psi^2}{\partial \eta^2} - C_{YY\xi\eta} \frac{\partial \psi^2}{\partial \xi \partial \eta} + C_{XY\xi} \frac{\partial \psi}{\partial \xi} + C_{XY\eta} \frac{\partial \psi}{\partial \eta} \quad (3.40)$$

Substituting the equation (3.11) and (3.40) into equations (3.38) yields;

$$\begin{aligned} & \left(C_{XX\xi\xi} \frac{\partial \psi^2}{\partial \xi^2} + C_{XX\eta\eta} \frac{\partial \psi^2}{\partial \eta^2} - C_{XX\xi\eta} \frac{\partial \psi^2}{\partial \xi \partial \eta} + C_{XX\xi} \frac{\partial \psi}{\partial \xi} + C_{XX\eta} \frac{\partial \psi}{\partial \eta} \right) \cos 2\theta \\ & + 2 \sin 2\theta \left(C_{XY\xi\xi} \frac{\partial \psi^2}{\partial \xi^2} + C_{YY\eta\eta} \frac{\partial \psi^2}{\partial \eta^2} - C_{YY\xi\eta} \frac{\partial \psi^2}{\partial \xi \partial \eta} + C_{XY\xi} \frac{\partial \psi}{\partial \xi} + C_{XY\eta} \frac{\partial \psi}{\partial \eta} \right) \\ & - \cos 2\theta \left(C_{YY\xi\xi} \frac{\partial \psi^2}{\partial \xi^2} + C_{YY\eta\eta} \frac{\partial \psi^2}{\partial \eta^2} - C_{YY\xi\eta} \frac{\partial \psi^2}{\partial \xi \partial \eta} + C_{YY\xi} \frac{\partial \psi}{\partial \xi} + C_{YY\eta} \frac{\partial \psi}{\partial \eta} \right) = 0 \end{aligned} \quad (3.41)$$

Rearranging yields the flow front boundary condition in computational domain as

$$\begin{aligned} & \frac{\partial \psi}{\partial \xi} \left[C_{XY\xi} 2 \sin 2\theta - (C_{YY\xi} - C_{XX\xi}) \cos 2\theta \right] \\ & \frac{\partial \psi}{\partial \eta} \left[2 \sin 2\theta C_{XY\eta} - (C_{YY\eta} - C_{XX\eta}) \cos 2\theta \right] \\ & \frac{\partial \psi^2}{\partial \xi^2} \left[2 \sin 2\theta C_{XY\xi\xi} - (C_{YY\xi\xi} - C_{XX\xi\xi}) \cos 2\theta \right] \\ & \frac{\partial \psi^2}{\partial \eta^2} \left[2 \sin 2\theta C_{XY\eta\eta} - (C_{YY\eta\eta} - C_{XX\eta\eta}) \cos 2\theta \right] \\ & \frac{\partial \psi^2}{\partial \xi \partial \eta} \left[-2 \sin 2\theta C_{XY\xi\eta} - (C_{XX\xi\eta} - C_{YY\xi\eta}) \cos 2\theta \right] = 0 \end{aligned} \quad (3.42)$$

The geometrical coefficients that are used in the transformed governing equation and the boundary conditions are summarized in Table 3.1.

Table 3.1 The geometrical coefficients of equation

$$C_{xx\xi} = \frac{1}{J^2} \left[(y_\eta y_{\xi\eta} - y_\xi y_{\eta\eta}) - \frac{J_\xi}{J} y_\eta^2 + \frac{J_\eta}{J} y_\eta y_\xi \right] \quad (3.15)$$

$$C_{xx\eta} = \frac{1}{J^2} \left[(y_\xi y_{\xi\eta} - y_\eta y_{\xi\xi}) - \frac{J_\xi}{J} y_\xi y_\eta - \frac{J_\eta}{J} y_\xi^2 \right] \quad (3.16)$$

$$C_{xx\xi\xi} = \frac{1}{J^2} y_\eta^2 \quad (3.12)$$

$$C_{xx\eta\eta} = \frac{1}{J^2} y_\xi^2 \quad (3.13)$$

$$C_{xx\xi\eta} = -\frac{2y_\xi y_\eta}{J^2} \quad (3.14)$$

$$C_{yy\xi} = \frac{1}{J^2} \left[(x_\eta x_{\xi\eta} - x_\xi x_{\eta\eta}) - \frac{J_\xi}{J} x_\eta^2 + \frac{J_\eta}{J} x_\eta x_\xi \right] \quad (3.22)$$

$$C_{yy\eta} = \frac{1}{J^2} \left[(x_\xi x_{\xi\eta} - x_\eta x_{\xi\xi}) - \frac{J_\xi}{J} x_\xi x_\eta - \frac{J_\eta}{J} x_\xi^2 \right] \quad (3.23)$$

$$C_{yy\xi\xi} = \frac{1}{J^2} x_\eta^2 \quad (3.19)$$

$$C_{yy\eta\eta} = \frac{1}{J^2} x_\xi^2 \quad (3.20)$$

$$C_{yy\xi\eta} = -\frac{2x_\xi x_\eta}{J^2} \quad (3.21)$$

$$C_{x\xi} = \frac{y_\eta}{J} \quad (3.28)$$

$$C_{x\eta} = -\frac{y_\xi}{J} \quad (3.29)$$

$$C_{y\eta} = \frac{x_\xi}{J} \quad (3.24)$$

$$C_{y\xi} = -\frac{x_\eta}{J} \quad (3.25)$$

$$J = x_\xi y_\eta - x_\eta y_\xi \quad (3.10)$$

3.2 Discretization of Governing Equation and Boundary Conditions in Transformed Solution Domain

The governing equation and boundary conditions in computational domain were derived in the previous chapter. Collecting the geometric and physical coefficients as

$$A_{\xi} = C_{xx\xi} + D_{11}C_{yy\xi} - D_{12}C_{y\xi} + D_{13}C_{x\xi} \quad (3.43)$$

$$A_{\xi\xi} = C_{xx\xi\xi} + D_{11}C_{yy\xi\xi} \quad (3.44)$$

$$A_{\eta} = C_{xx\eta} + D_{11}C_{yy\eta} + D_{12}C_{y\eta} + D_{13}C_{x\eta} \quad (3.45)$$

$$A_{\eta\eta} = C_{xx\eta\eta} + D_{11}C_{yy\eta\eta} \quad (3.46)$$

$$A_{\xi\eta} = C_{xx\xi\eta} + D_{11}C_{yy\xi\eta} \quad (3.47)$$

and substituting into equation (3.36) yields a simpler form of the governing equation as

$$A_{\xi} \frac{\partial \psi}{\partial \xi} + A_{\eta} \frac{\partial \psi}{\partial \eta} + A_{\xi\xi} \frac{\partial \psi^2}{\partial \xi^2} + A_{\eta\eta} \frac{\partial \psi^2}{\partial \eta^2} + A_{\xi\eta} \frac{\partial \psi^2}{\partial \xi \partial \eta} = 0 \quad (3.48)$$

Equation (3.48) is discretized for a finite difference solution. Appendix-B presents various finite difference formulations for an M x N computational domain grid system. Derivatives in equation (3.48) are centrally differenced based on Appendix B as equation (3.48) is valid for interior nodes only.

The resulting discretized equation is

$$A_{\xi} \frac{1}{2}(\psi_{i+1,j} - \psi_{i-1,j}) + A_{\eta} \frac{1}{2}(\psi_{i,j+1} - \psi_{i,j-1}) + A_{\xi\xi}(\psi_{i+1,j} - 2\psi_{i,j} + \psi_{i-1,j}) \quad (3.49)$$

$$A_{\eta\eta}(\psi_{i,j+1} - 2\psi_{i,j} + \psi_{i,j-1}) + A_{\xi\eta} \frac{1}{4}(\psi_{i+1,j+1} - \psi_{i+1,j-1} - \psi_{i-1,j+1} + \psi_{i-1,j-1}) = 0$$

Rearranging gives

$$\begin{aligned}
\psi_{i,j} = & \frac{1}{8} \frac{A_{\xi\eta}}{(A_{\xi\xi} + A_{\eta\eta})} \psi_{i-1,j-1} + \frac{\left(-A_{\eta} \frac{1}{2} + A_{\eta\eta}\right)}{2(A_{\xi\xi} + A_{\eta\eta})} \psi_{i,j-1} \\
& - \frac{1}{8} \frac{A_{\xi\eta}}{(A_{\xi\xi} + A_{\eta\eta})} \psi_{i+1,j-1} + \frac{\left(A_{\xi\xi} - A_{\xi} \frac{1}{2}\right)}{2(A_{\xi\xi} + A_{\eta\eta})} \psi_{i-1,j} \\
& + \frac{\left(\frac{1}{2}A_{\xi} + A_{\xi\xi}\right)}{2(A_{\xi\xi} + A_{\eta\eta})} \psi_{i+1,j} - \frac{1}{8} \frac{A_{\xi\eta}}{(A_{\xi\xi} + A_{\eta\eta})} \psi_{i-1,j+1} \\
& + \frac{\left(A_{\eta} \frac{1}{2} + A_{\eta\eta}\right)}{2(A_{\xi\xi} + A_{\eta\eta})} \psi_{i,j+1} + \frac{1}{8} \frac{A_{\xi\eta}}{(A_{\xi\xi} + A_{\eta\eta})} \psi_{i+1,j+1}
\end{aligned} \tag{3.50}$$

Defining the constants

$$A_1 = \frac{A_{\xi\eta}}{8(A_{\xi\xi} + A_{\eta\eta})} \tag{3.51a}$$

$$A_2 = \left[\frac{1}{2(A_{\xi\xi} + A_{\eta\eta})} \right] \left[A_{\eta\eta} - \frac{A_{\eta}}{2} \right] \tag{3.51b}$$

$$A_3 = \frac{-A_{\xi\eta}}{8(A_{\xi\xi} + A_{\eta\eta})} \tag{3.51c}$$

$$A_4 = \left[\frac{1}{2(A_{\xi\xi} + A_{\eta\eta})} \right] \left[A_{\xi\xi} - \frac{A_{\xi}}{2} \right] \tag{3.51d}$$

$$A_5 = \left[\frac{1}{2(A_{\xi\xi} + A_{\eta\eta})} \right] \left[A_{\xi\xi} + \frac{A_{\xi}}{2} \right] \tag{3.51e}$$

$$A_6 = \left[\frac{1}{2(A_{\xi\xi} + A_{\eta\eta})} \right] \left[A_{\eta\eta} + \frac{A_{\eta}}{2} \right] \tag{3.51f}$$

and successively substituting in equation (3.50) gives the final centrally discretized governing equation as

$$\begin{aligned} \psi_{i,j} = & A_1\psi_{i-1,j-1} + A_2\psi_{i,j-1} + A_3\psi_{i+1,j-1} + A_4\psi_{i-1,j} \\ & + A_5\psi_{i+1,j} + A_6\psi_{i,j+1} + A_7\psi_{i-1,j+1} + A_8\psi_{i+1,j+1} = 0 \end{aligned} \quad (3.52)$$

For the flow front boundary condition, defining the coefficients

$$B_\xi = \left[2C_{xy\xi} \sin 2\theta - (C_{yy\xi} - C_{xx\xi}) \cos 2\theta \right] \quad (3.53a)$$

$$B_\eta = \left[2C_{xy\eta} \sin 2\theta - (C_{yy\eta} - C_{xx\eta}) \cos 2\theta \right] \quad (3.53b)$$

$$B_{\xi\xi} = \left[2C_{xy\xi\eta} \sin 2\theta - (C_{yy\xi\xi} - C_{xx\xi\xi}) \cos 2\theta \right] \quad (3.53c)$$

$$B_{\eta\eta} = \left[2C_{xy\eta\eta} \sin 2\theta - (C_{yy\eta\eta} - C_{xx\eta\eta}) \cos 2\theta \right] \quad (3.53d)$$

$$B_{\xi\eta} = \left[2C_{xy\xi\eta} \sin 2\theta - (C_{yy\xi\eta} - C_{xx\xi\eta}) \cos 2\theta \right] \quad (3.53e)$$

and placing in equation (3.42) yields

$$\frac{\partial \psi}{\partial \xi} B_\xi + \frac{\partial \psi}{\partial \eta} B_\eta + \frac{\partial \psi^2}{\partial \xi^2} B_{\xi\xi} + \frac{\partial \psi^2}{\partial \eta^2} B_{\eta\eta} + \frac{\partial \psi^2}{\partial \xi \partial \eta} B_{\xi\eta} = 0 \quad (3.54)$$

The flow front nodes lie on the last ξ line ($i=M$). Thus, all discretization for ξ derivatives involve backward differencing. For η direction derivatives, central differencing is employed. It should be noted that the flow front nodes at $j=1$ and $j=N$ are solid boundary nodes and subject to prescribed ψ conditions.

Then,

$$\frac{\partial \psi}{\partial \xi} \Big|_{M,j} = \frac{1}{2} (3\psi_{M,j} - 4\psi_{M-1,j} + \psi_{M-2,j}) \quad (3.55)$$

$$\frac{\partial \psi}{\partial \eta} \Big|_{M,j} = \frac{1}{2} (\psi_{M,j+1} - \psi_{M,j-1}) \quad (3.56)$$

$$\frac{\partial \psi^2}{\partial \xi^2} \Big|_{M,j} = (2\psi_{M,j} - 5\psi_{M-1,j} + 4\psi_{M-2,j} - \psi_{M-3,j}) \quad (3.57)$$

$$\frac{\partial \psi^2}{\partial \eta^2} \Big|_{M,j} = (\psi_{M,j+1} - 2\psi_{M,j} + \psi_{M,j-1}) \quad (3.58)$$

$$\frac{\partial \psi^2}{\partial \xi \partial \eta} \Big|_{M,j} = \frac{1}{2} (\psi_{M,j+1} - \psi_{M,j-1} - \psi_{M-1,j+1} + \psi_{M-1,j-1}) \quad (3.59)$$

Substituting the above equations in equation (3.54) yields

$$\begin{aligned}
& B_{\xi} \frac{1}{2} (3\psi_{M,j} - 4\psi_{M-1,j} + \psi_{M-2,j}) \\
& + B_{\eta} \frac{1}{2} (\psi_{M,j+1} - \psi_{M,j-1}) \\
& + B_{\xi\xi} (2\psi_{M,j} - 5\psi_{M-1,j} + 4\psi_{M-2,j} - \psi_{M-3,j}) \\
& + B_{\eta\eta} (\psi_{M,j+1} - 2\psi_{M,j} + \psi_{M,j-1}) \\
& + B_{\xi\eta} \frac{1}{2} (\psi_{M,j+1} - \psi_{M,j-1} - \psi_{M-1,j+1} + \psi_{M-1,j-1}) = 0
\end{aligned} \tag{3.60}$$

Further defining the coefficients

$$B_P = \left[\frac{3}{2} B_{\xi} + 2B_{\xi\xi} - 2B_{\eta\eta} \right]^{-1} \tag{3.61a}$$

$$B_1 = B_P \left[-\frac{B_{\xi\eta}}{2} \right] \tag{3.61b}$$

$$B_2 = B_P \left[\frac{1}{2} B_{\eta} - B_{\eta\eta} + \frac{B_{\xi\eta}}{2} \right] \tag{3.61c}$$

$$B_3 = B_P \left[B_{\xi\xi} \right] \tag{3.61d}$$

$$B_4 = B_P \left[-\frac{1}{2} B_{\xi} - 4B_{\xi\xi} \right] \tag{3.61e}$$

$$B_5 = B_P \left[2B_{\xi} - 5B_{\xi\xi} \right] \tag{3.61f}$$

$$B_6 = B_P \left[\frac{1}{2} B_{\xi\eta} \right] \tag{3.61g}$$

$$B_7 = B_P \left[-\frac{1}{2} B_{\eta} - B_{\eta\eta} - \frac{1}{2} B_{\xi\eta} \right] \tag{3.61h}$$

and substituting in equation (3.60) and rearranging yields the final form of the discretized flow front boundary condition as

$$\psi_{M,j} = B_1\psi_{M-1,j-1} + B_2\psi_{M,j-1} + B_3\psi_{M-3,j} + B_4\psi_{M-2,j} \quad (3.62)$$

$$B_5\psi_{M-1,j} + B_6\psi_{M-1,j-1} + B_7\psi_{M,j+1}$$

3.3 Solution Method

The discretized governing equation and boundary condition equations are written for all the nodes, resulting in a system of linear algebraic equations. For all interior nodes, $i=2$ to $M-1$ and $j=2$ to $N-1$, equation (3.52) is valid. For the mold walls, at $j=1$, $\psi_{i,1} = 0$ and at $j=N$, $\psi_{i,N} = 1$ for $i=1$ to M . For the flow front nodes at $i=M$ for $j=2$ to $N-1$, equation (3.62) is written.

The resulting systems of equations are solved for $\psi_{i,j}$ at every position of the flow front (at each time step) using successive over relaxation, SOR, iteration scheme. The convergence criterion is given as;

$$\left\{ \left| \frac{\psi_{i,j}^{NEW} - \psi_{i,j}^{OLD}}{\psi_{i,j}^{OLD}} \right| \times 100 \right\} < \xi_{CONV} \quad (3.63)$$

In the above equations, the superscripts OLD and NEW refer to successive iteration solutions.

3.4 Determination of Process Parameters

Following the determination of stream function values on the grid nodes, corresponding velocity and pressure distributions are calculated as follows:

3.4.1 Velocity

Velocity calculations are performed using the stream function – velocity relations presented earlier in equations (2.13) and (2.14). From the scaled stream function implementation of section 2.2.2, the velocities can be obtained as

$$u = \frac{\partial \psi}{\partial y} = \Delta \psi_{\max} \frac{\partial}{\partial y}(\psi^*) = \left[\frac{\partial x}{\partial \xi} \frac{\partial \psi^*}{\partial \eta} - \frac{\partial x}{\partial \eta} \frac{\partial \psi^*}{\partial \xi} \right] \times \frac{u_0 \times L_0}{2xJ} \times \frac{1}{(1-v_f)} \quad (3.64)$$

$$v = -\frac{\partial \psi}{\partial x} = \Delta \psi_{\max} \frac{\partial}{\partial x}(\psi^*) = \left[\frac{\partial y}{\partial \xi} \frac{\partial \psi^*}{\partial \eta} - \frac{\partial y}{\partial \eta} \frac{\partial \psi^*}{\partial \xi} \right] \times \frac{u_0 \times L_0}{2xJ} \times \frac{1}{(1-v_f)} \quad (3.65)$$

The discretization of equations (3.64) and (3.65) during the present study was carried out in the manner presented in Appendix B. The discretized equations (3.64) and (3.65) contain the term $\frac{u_0 L_0}{1-v_f}$ to account for the scaling of the stream values to the maximum volume of 1. u_0 is the inlet injection velocity, J is the gate width, v_f is the fiber volume fraction in cavity and $1-v_f$ is porosity, \mathcal{E} .

3.4.2 Pressure

Following the determination of stream function values, the pressure distribution is obtained using Darcy law and stream function definition starting with

$$dp = \frac{\partial P}{\partial x} dx + \frac{\partial P}{\partial y} dy \quad (3.66)$$

$$\int dp = \int \frac{\partial P}{\partial x} dx + \int \frac{\partial P}{\partial y} dy \quad (3.67)$$

Placing the Darcy's law of equations (2.11) and (2.12) in equation (3.67)

$$\int dp = -\int \left(\frac{\mu}{K_{xx}} u \right) dx - \int \left(\frac{\mu}{K_{yy}} v \right) dy \quad (3.69)$$

Between any two points A and B within the mold, if the points are close to one another, equation (3.69) can be integrated to yield.

$$P_A - P_B \cong - \left(\frac{\mu}{K_{xx}} u \right)_{\frac{A+B}{2}} (x_A - x_B) - \left(\frac{\mu}{K_{yy}} v \right)_{\frac{A+B}{2}} (y_A - y_B) \quad (3.70)$$

or approximately

$$P_A - P_B = - \left[\frac{(\mu_B + \mu_A)(x_A - x_B)}{2(K_{xx,B} + K_{xx,A})} \right] (u_B + u_A) \quad (3.71)$$

$$- \left[\frac{(\mu_B + \mu_A)(y_A - y_B)}{2(K_{yy,B} + K_{yy,A})} \right] (v_B + v_A)$$

Introducing the stream function, equation (3.69) becomes;

$$P_A - P_B = \left\{ \frac{(\mu_B + \mu_A)(y_A - y_B)}{2(K_{yy,B} + K_{yy,A})} \right\} \left[\left(\frac{\partial \psi}{\partial x} \right)_B + \left(\frac{\partial \psi}{\partial x} \right)_A \right] \quad (3.72)$$

$$- \left\{ \frac{(\mu_B + \mu_A)(x_A - x_B)}{2(K_{xx,B} + K_{xx,A})} \right\} \left[\left(\frac{\partial \psi}{\partial y} \right)_B + \left(\frac{\partial \psi}{\partial y} \right)_A \right]$$

Lastly, transforming into the computational domain through equation (2.13) and (2.14) and solving for P_A , pressure formulation becomes;

$$P_A = \left\{ \frac{(\mu_B + \mu_A)(y_A - y_B)}{2(K_{yy,B} + K_{yy,A})} \right\} \left[\left(C_{x\xi} \frac{\partial \psi}{\partial \xi} + C_{x\eta} \frac{\partial \psi}{\partial \eta} \right)_B + \left(C_{x\xi} \frac{\partial \psi}{\partial \xi} + C_{x\eta} \frac{\partial \psi}{\partial \eta} \right)_A \right]$$

$$- \left\{ \frac{(\mu_B + \mu_A)(x_A - x_B)}{2(K_{xx,B} + K_{xx,A})} \right\} \left[\left(C_{y\xi} \frac{\partial \psi}{\partial \xi} + C_{y\eta} \frac{\partial \psi}{\partial \eta} \right)_B + \left(C_{y\xi} \frac{\partial \psi}{\partial \xi} + C_{y\eta} \frac{\partial \psi}{\partial \eta} \right)_A \right] \quad (3.73)$$

$$- P_B$$

where the coefficients $C_{x\xi}$, $C_{x\eta}$, $C_{y\xi}$, $C_{y\eta}$ are given in Table 3.1. Equation (3.73) is discretized using the finite difference equation of appendix C. The discretized equations are given in the Appendix C by equations (C.1) to (C.24).

The pressure at point A can be determined if the pressure at point B is known. The flow front pressure is assumed to be zero. Thus, the above equation can give the pressure distribution within the whole flow domain starting from the flow front and working backward to the inlet gate.

3.5 Evolution of Flow Domain

3.5.1 Solution Sequence in the Program

The determination of the flow domain parameters (stream function, velocities and flow pressure) was explained in the previous section. In the computer program, the sequence of the calculations, movement of the resin front and the subsequent flow domain evolution follow the below outline.

Flow domain exists in the mold with the mesh generated inside. Then,

1. Stream function values are calculated on the grid nodes
2. Velocities are calculated on the grid nodes
3. Using flow front nodal velocities, the flow front advances with a time increment of Δt . The location of the new flow front is determined as

$$\vec{R}_{new\ flow\ front} = \vec{R}_{old\ flow\ front} + \vec{V}_{flow\ front} \cdot \Delta t$$

4. With the new flow front, the mold boundary and the inlet gate, a new flow domain is defined. A new mesh is generated in this flow field.
5. Stream function and velocity values from the “old” mesh are transformed onto the new mesh.
6. Pressure on all grid nodes are calculated
7. Time level is advanced to $t = t + \Delta t$. The next iteration starts from step 1 again

A detailed flowchart for the computer program is presented in Appendix D.

3.5.2 Flow Front Advancement

Figure 3.3 shows an example of flow front advancement between successive quasi-steady solutions (two consecutive time levels).

The nodes 2 and 3 move to the new positions (2', 3') along the new resin front. A slip condition or imposed orthogonality relocation method is used to define the new impregnation front/mold wall contact points. During slip based contact point movement, shown in Figure 3.3, new impregnation front/mold wall contact points, such as point 1' in the figure, are determined by locating intersections between cubic spline curve fits of the mold wall nodes (i.e. the points W1, W2, W3, W4, etc.) and a cubic spline curve fit of the newly determined resin front using the contact point from the previous time step (i.e. a spline of the points 1, 2', 3', etc.). The new contact point becomes 1'. In some cases, this contact point relocation can bring about the elimination of some newly determined resin front nodal points such as the point 2' in Figure 3.3 After that, replacement points along the newly determined free surface can be added (points 2'' and 3'', etc.).

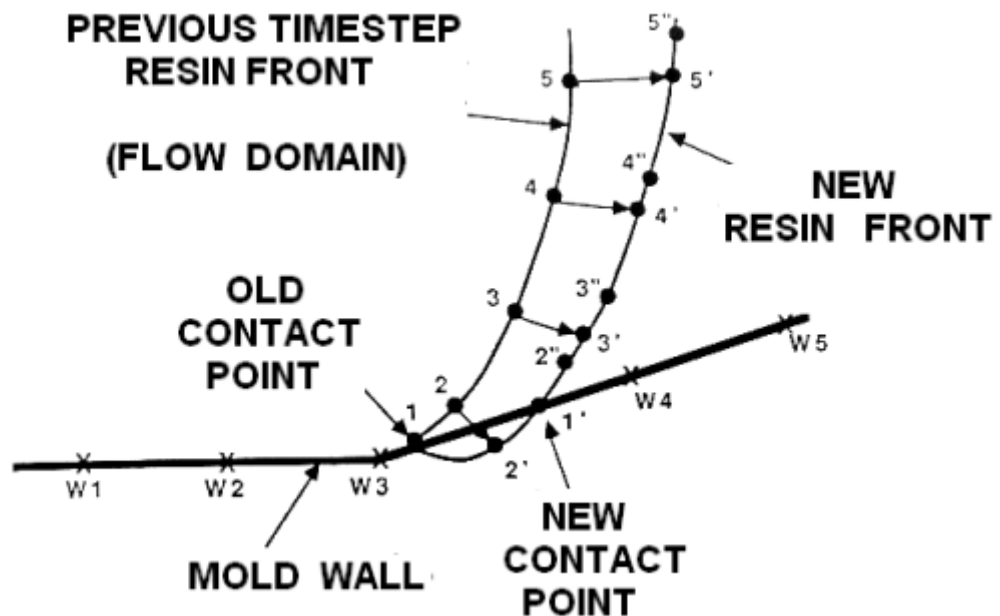


Figure 3.3 Impregnation front advancement with slip based contact point relocations [1].

When the near-wall tangential velocities (tangent to wall) fall below a specified percentage of maximum flow field velocity, an orthogonality method is applied, which results in the resin flow front intersecting the mold wall normally as shown in Figure 3.4. This approach reduces truncation errors in finite difference equations, and improves the accuracy of the finite difference results [1].

During impregnation, the growth in the physical size of the fluid flow field necessitates an increase in the number of computational nodal points in the ξ direction. In that case, a new $\xi = \text{constant}$ mesh line is added to the grid system. On the other hand, the mesh lines along η direction remain the same throughout the simulation. Thus, at the beginning, the initial flow domain is sketched with a large number of η lines, but relatively small number of ξ lines.

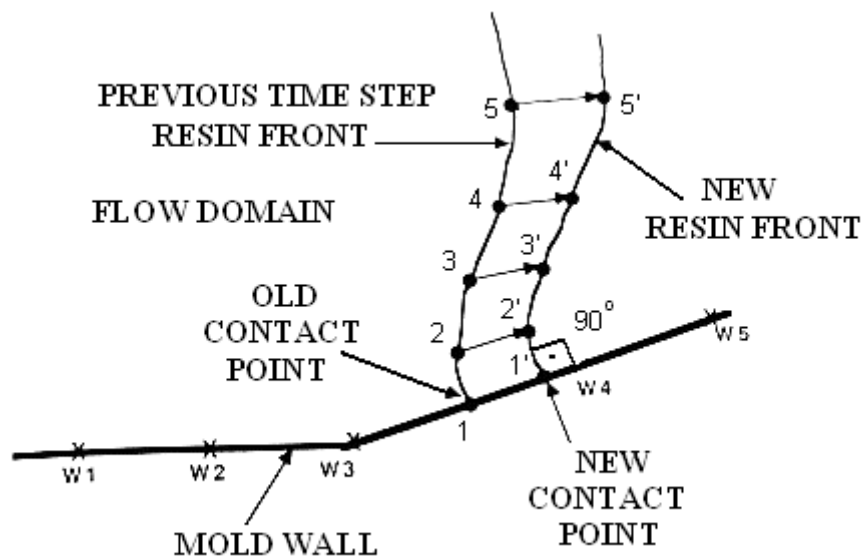


Figure 3.4 The impregnation front advancement with imposed orthogonality based contact point relocation [1].

3.6 Double Gate Injection Simulation

One of the goals of the current study was to increase the versatility of the current program by developing a double gate injection simulation capability. Double gate (or multiple-gate) injection is useful in RTM applications as the mold cavity can be filled at less time. In addition, multiple gate injection

enables the adjustment of the fill patterns and the location(s) of fill points in the mold cavity to a larger degree.

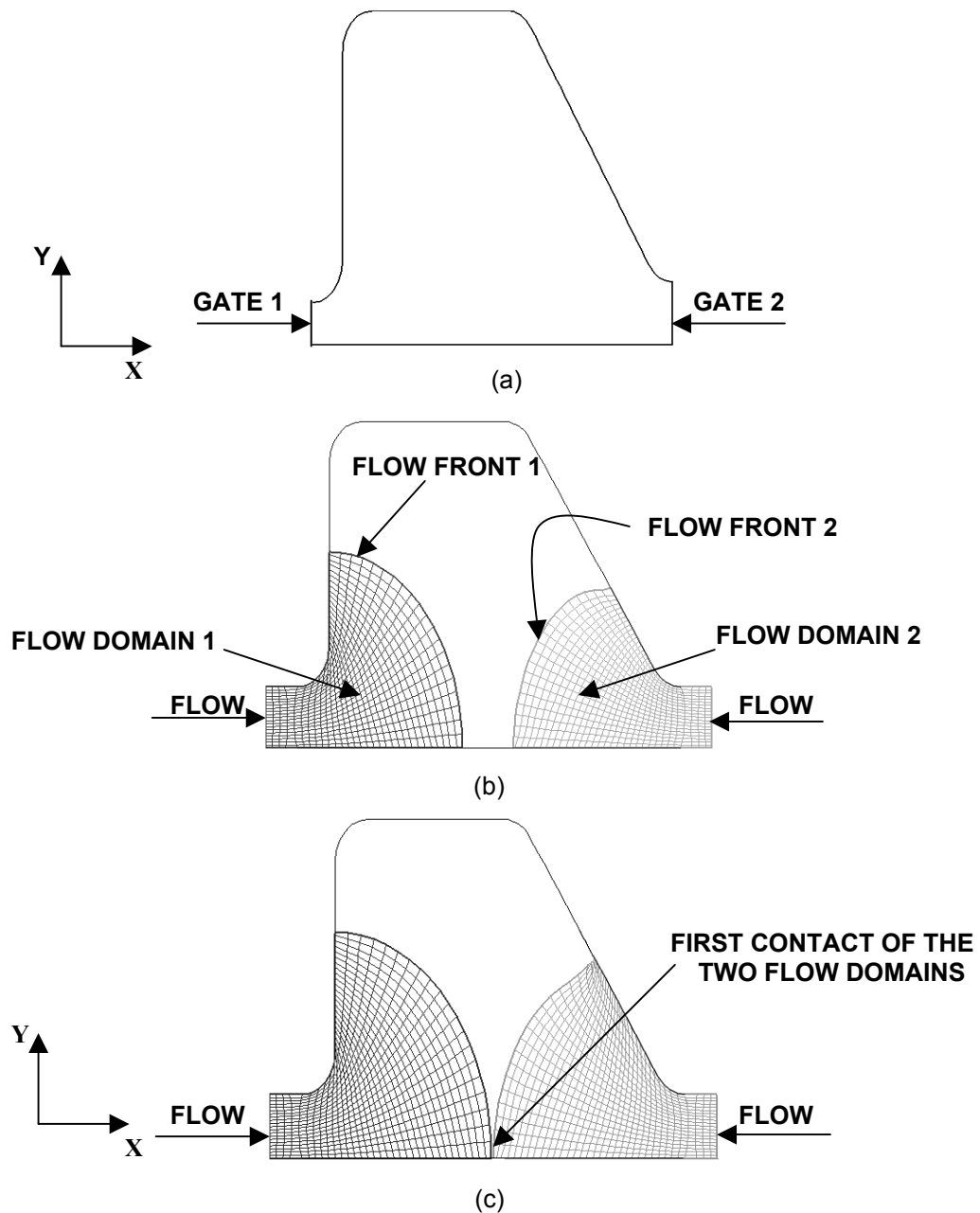


Figure 3.5 Double gate injections in a two dimensional irregular geometry mold cavity.

Figure 3.5a presents the sketch of an irregular shaped mold cavity, which has a much smaller thickness (in z-direction) than planar dimensions. There are two resin inlet (injection) gates as shown. As the resin begins filling from both gates, the flow domain evolutions are the same as a single gate flow domains (Figure 3.5b). The computer program was modified to accept two

flow domains (each with its own inlet gate), which is a relatively straightforward modification. The majority of the program modification begins after the flow fronts first make contact (Figure 3.5c). This section presents the double-gate injection simulation in two parts: conditions at the instant of first contact and condition afterwards.

3.6.1. First Contact of Two Advancing Flow Fronts

When the flow domains first meet, they meet at a single point (Figure 3.5c). Up until this time instant, the two domains (both physical and computational) were independent. But from this instant on, the merged flow front points become a single point with unique properties that are valid in both domains. Thus, the calculation of the flow parameters is changed.

When the flow fronts first meet as seen in Figure 3.5c, the stream function values are already known on all the nodes (Appendix D). Due to the mold wall location of the intersection point (a boundary point), the stream function value at this position is the same zero value, even if it is obtained separately from each flow domain solution.

However, unlike the stream function, separate flow domain solutions yield two different velocities at the intersection point, which can not be used. Therefore, once the flow fronts are advanced and the initial contact point is determined, a single velocity at the contact point must be calculated using both domains.

A close-up of the domain initial contact is presented in Figure 3.6. Some of the nodes around and including the contact point are numbered from 1 to 7 (point 2 is the contact point).

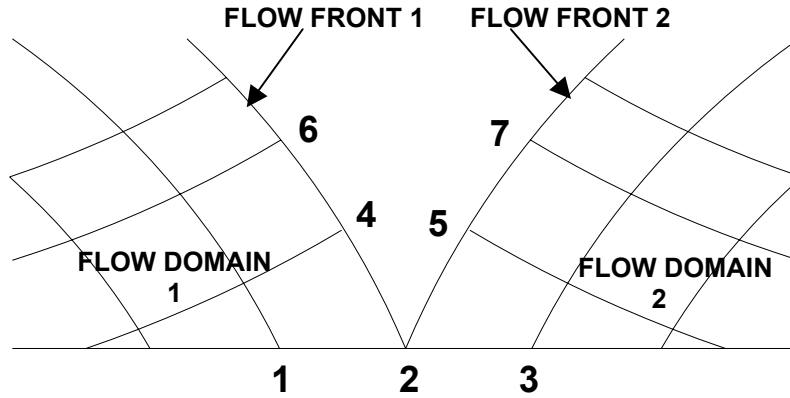
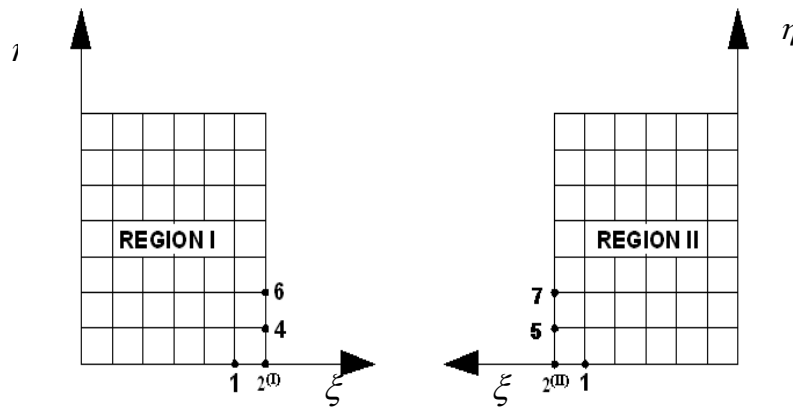
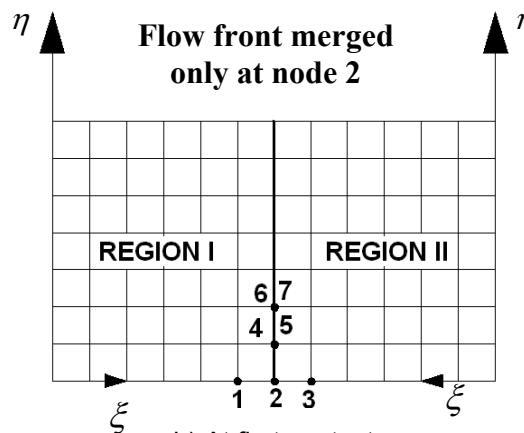


Figure 3.6 The initial contact of two advancing resin flow fronts.

In each flow domain, before contact, the velocities were determined using equations (3.64) and (3.65) in section 3.4.1. Once contact is made, point 2 becomes the same node on both domains as depicted in Figure 3.6. All other nodes on the flow front (4, 5, 6, 7, etc.) are separate. The computational domains before and at contact are depicted in Figure 3.7.



a) Right before contact $2^{(I)}$ is in the domain 1, $2^{(II)}$ in domain 2.



b) At first contact

Figure 3.7 Computational domains before and at first contact of two advancing flow fronts.

At contact, node 2 is considered an "interior" node that lies on the mold wall, i.e. not much different than node 1 or node 3. Thus, the calculation of the velocity of node 2 proceeds in a similar manner, with one difference. The derivatives in η direction in equations (3.64) and (3.65) are now taken as the average of the derivatives in domain 1 and domain 2. Specifically the derivatives for node 2, after contact, become

$$\psi_{\eta,2} = \frac{1}{2} \left(\frac{-3\psi_2 + 4\psi_4 - \psi_6}{2\Delta\eta} + \frac{-3\psi_2 + 4\psi_5 - \psi_7}{2\Delta\eta} \right) \quad (3.48)$$

$$\psi_{\xi,2} = \frac{\psi_1 - \psi_3}{2\Delta\xi} \quad (3.49)$$

$$y_{\eta,2} = \frac{1}{2} \left(\frac{-3y_2 + 4y_4 - y_6}{2\Delta\eta} + \frac{-3y_2 + 4y_5 - y_7}{2\Delta\eta} \right) \quad (3.50)$$

$$y_{\xi,2} = \frac{y_1 - y_3}{2\Delta\xi} \quad (3.51)$$

$$x_{\eta,2} = \frac{1}{2} \left(\frac{-3x_2 + 4x_4 - x_6}{2\Delta\eta} + \frac{-3x_2 + 4x_5 - x_7}{2\Delta\eta} \right) \quad (3.52)$$

$$x_{\xi,2} = \frac{x_1 - x_3}{2\Delta\xi} \quad (3.53)$$

with

$$J_2 = x_{\xi,2} y_{\eta,2} - x_{\eta,2} y_{\xi,2} \quad (3.54)$$

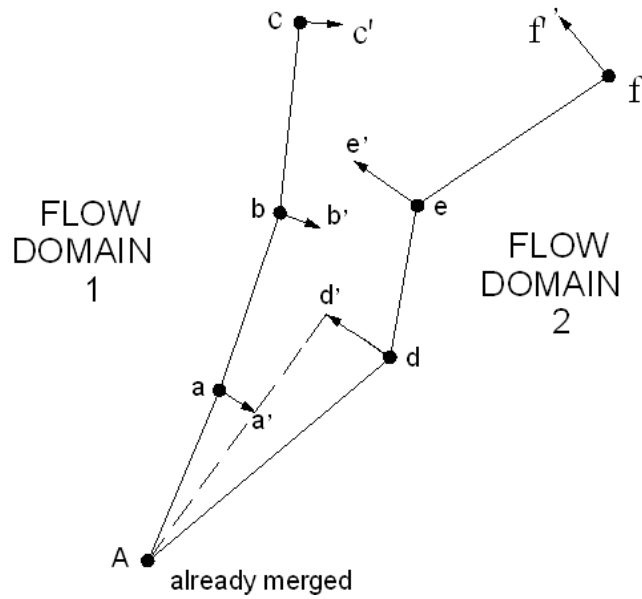
In the given configuration of the Figures 3.6 and 3.7, the contact point in velocity value in the y-direction "v" is zero because the mold wall lies along x-direction. Thus, for this contact point, a single velocity component, "u", exists and is calculated using the modified derivatives in velocity formulations.

3.6.2. Further Contact of Two Advancing and Merging Flow Fronts

After the determination of first contact point velocity, the rest of the flow parameters are obtained. Specifically, the stream function and velocity values on the mesh nodes of the previous flow front position (Figure 3.7a) i.e. no contact state, are transported to the current (contact) mesh (Figure 3.7b), except those at the contact point (whose derivatives were given in the previous section).

The pressure values at all nodes (except the contact point) are determined using the formulation of Appendix C. For the contact point, the determination of pressure resembles that of the velocity calculation. The contact point is once again treated as an interior node that lies on the mold wall. Thus, the corresponding pressure formulation corresponds to "Region 2" in Appendix D, with the derivatives in η direction, again coming from averaged values in both domains.

Afterwards, the time level is increased and the next iteration is performed similarly. After the initial contact on the mold wall, the successive contacts take place at locations away from the mold wall, where the two flow fronts merge. The determination of the merge points (and the resulting "weld" line) is performed by checking, at every iterations, whether the nodes on each front pass into the domain of the other flow front. The new intersection (merge) points are obtained as depicted in Figure 3.8.



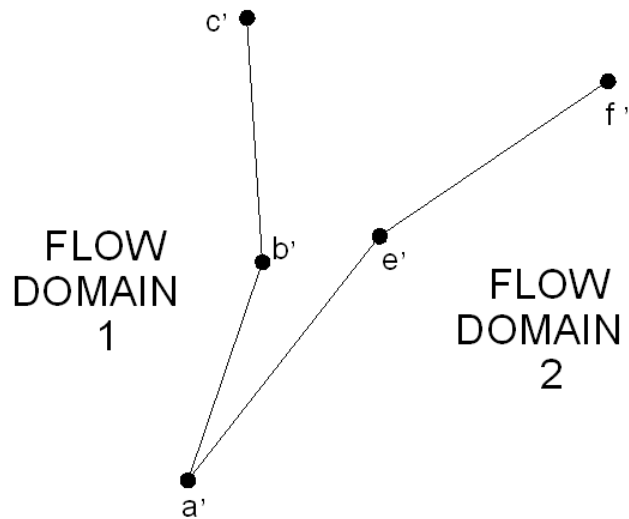
(a) Flow front at t

A : on already merged node (as of time t)

a to f : front nodes at the current time step, t

a' to f' : position of the nodes after Δt time increment advancement.

- - - - : hypothetical line between A and d', on which a' lies (Δt is adjusted to ensure such an outcome)



b) New flow fronts at $t + \Delta t$ (the nodes on each flow front b', c', etc and e',f' etc. Will be redistributed every on each front.

Figure 3.8 Determination of the contact point on merging flow fronts

The determination of the properties in other contact points is similar to the previous section. In Figure 3.9, node 1 (which is common in the two flow

domains) is treated as an interior mold wall node. Node 4 (which is the next contact point) is also treated as an interior point with averaged η derivatives. However, it is not lying on the mold wall like node 1.

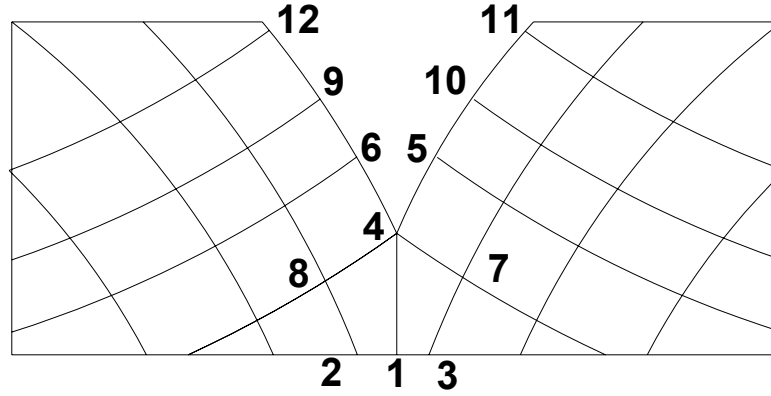


Figure 3.9 The merging of two flow fronts (nodes 1 to 4 are contact nodes)

The modified derivatives for node 4 are

$$\psi_{\eta,4} = \frac{1}{2} \left(\frac{\psi_6 - \psi_1}{2\Delta\eta} + \frac{\psi_5 - \psi_1}{2\Delta\eta} \right) \quad (3.55)$$

$$\psi_{\xi,4} = \frac{\psi_7 - \psi_8}{2\Delta\xi} \quad (3.56)$$

$$y_{\eta,4} = \frac{1}{2} \left(\frac{y_6 - y_1}{2\Delta\eta} + \frac{y_5 - y_1}{2\Delta\eta} \right) \quad (3.57)$$

$$y_{\xi,4} = \frac{y_7 - y_8}{2\Delta\xi} \quad (3.58)$$

$$x_{\eta,4} = \frac{1}{2} \left(\frac{x_6 - x_1}{2\Delta\eta} + \frac{x_5 - x_1}{2\Delta\eta} \right) \quad (3.59)$$

$$x_{\xi,4} = \frac{x_7 - x_8}{2\Delta\xi} \quad (3.60)$$

$$J_4 = x_{\xi,2} y_{\eta,2} - x_{\eta,2} y_{\xi,2} \quad (3.61)$$

If one is to recall the numerical solution procedure, the stream functions are determined through SOR solution (Section 3.3). In multiple flow domains with merging flow fronts, the iteration procedure is applied to all domains separately. After convergence in each domain, the stream function values on common (merged) front nodes (e.g. nodes 1 and 4 in Figure 3.9) are checked against each other. The iterations procedure is repeated until same values are obtained at merged nodes.

CHAPTER 4

RESULTS AND DISCUSSION

In this chapter, the RTM code is used to simulate various impregnation scenarios. The results are presented and discussed for single gate injection (1-D and 2-D flow) and double gate injection (2-D flow). The flowchart of the simulation program is presented in Appendix D.

4.1 1-D RTM Simulations

In order to validate the RTM predictions of the computer code, a test case of steady, one-dimensional RTM flow in a straight channel mold cavity was simulated. A sketch of the process is shown in Figure 4.1.

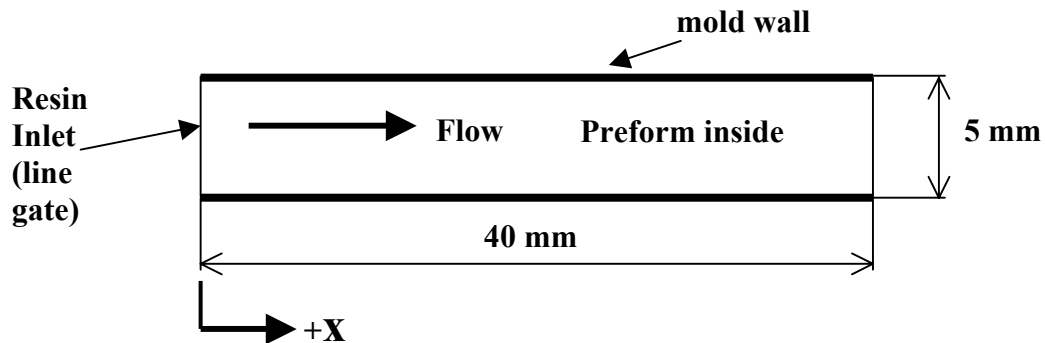


Figure 4.1 1-D Mold configuration

The problem has an analytical solution for uniform constant injection velocity at the inlet line gate, u_0

$$\frac{u_0}{1-v_f} = \frac{dx}{dt} = \text{constant} \quad (4.1)$$

where v_f is the fiber volume fraction, " $1-v_f$ " the porosity in the preform and t is time. Since u_0 is the superficial velocity, the actual resin velocity through the perform is $u_0/(1-v_f)$.

The flow velocity remains the same everywhere in the flow domain. Denoting the position of flow front as x_L at any time, integrating equation (4.1) yields

$$x_L = \frac{u_0}{1 - v_f} \cdot t \quad (4.2)$$

From Darcy' law, for 1-D, steady state flow in x-direction, the inlet injection velocity can be written as;

$$u_0 = - \frac{K_{xx}}{\mu} \frac{dP}{dx} \quad (4.3)$$

where K_{xx} the permeability in the x- direction is, μ is the viscosity, P is the pressure. Equation (4.3) can be integrated as

$$P(x) = \frac{\mu \cdot u_0}{K_{xx}} (x_L - x) \quad (4.4)$$

where x is any position within the flow domain. The flow front pressure is taken as atmospheric, hence zero gage (i.e. open to atmosphere through air vents in mold). The inlet pressure at $x=0$ is

$$P_{inlet} = \frac{\mu}{K_x} u_0 x_L \quad (4.5)$$

For 1-D impregnation, the RTM program is run for the parameters stated in the Table 4.1. The used data is taken from [24], where the same scenario is used for a different solution method.

Table 4.1 Process parameters and results for 1-D flow verification studies

u_0	1 mm/s
μ	1.149 Pa.s
K_{xx}	$38.37 \times 10^{-2} \text{ mm}^2$
$\Delta t_{INCREMENT}$	0.1 s
<i>Fiber Volume Fraction</i>	0.5
<i>Exact Fill Time</i>	15 s
<i>Numerical Fill Time</i>	15 s

The results show that the numerical fill time obtained through the simulation and the exact fill time obtained by using equation (4.5) are identical. Comparison of numerical and exact inlet pressure is presented in Figure 4.2. The exact pressure is determined via equation (4.5). As before, exact and numerical values are in excellent agreement. The fill time (complete filling of the mold by resin) under constant injection velocity shows no difference in numerical and exact calculations.

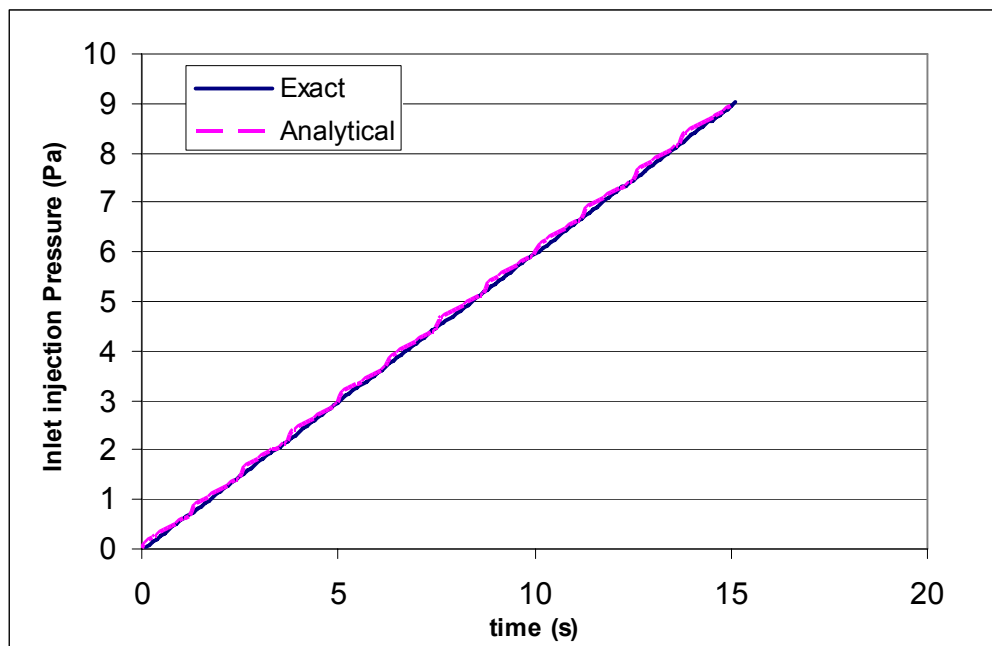


Figure 4.2 Variation of inlet pressure during one-dimensional RTM under constant injection rate

4.1.1 Permeability Analysis

The effects of preform permeability on results are investigated for 1-D RTM. The RTM configurations and various results are shown in the Table 4.2. The input values were taken from the reference [25].

Table 4.2 Process parameters and results for 1-D permeability analysis

	u_0 (mm/s)	Permeability $K_{xx} \times 10^{-5} \text{ mm}^2$	Numerical time increment Δt (s)	Fiber Volume Fraction v_f	Resin Viscosity (Pa.s) μ	Inlet Pressure (Pa) at the end of fill	Fill Time (s)
1	1	38.38	0.1	0.5	1.149	8.94	15
2	1	90	0.1	0.5	1.149	3.81	15
3	1	312	0.1	0.5	1.149	1.09	15

The simulation was performed for three different permeability values and the results are seen in Figure 4.3. As expected, inlet pressure increases at a slower rate as the fiber preform permeability increases.

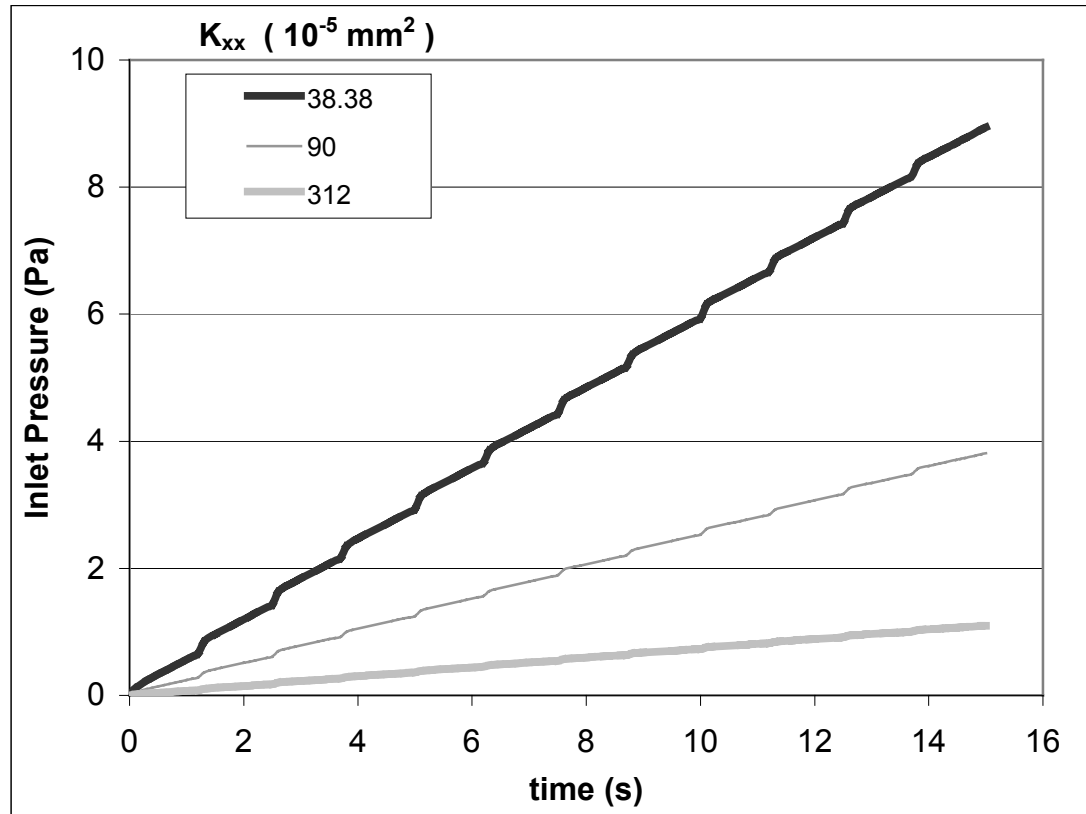


Figure 4.3 Variation of inlet pressure during one-dimensional RTM constant injection rate with different perform permeabilities values.

There is no change in the fill time with different permeability values, as the injection velocity is not changed.

4.1.2 Velocity Analysis

In this part the effects of varying the injection velocity are presented. The RTM run configuration and the results can be seen in Table 4.3 and the effect of varying the injection velocity on the fill time and inlet pressure can be seen in Figure 4.4.

Table 4.3 Process parameters and results for 1-D velocity analysis

	u_0 (mm/s)	Permeability $K_{xx} \times 10^{-5} \text{ mm}^2$	Numerical time increment Δt (s)	Fiber Volume Fraction v_f	Resin Viscosity (Pa.s) μ	Inlet Pressure (Pa) at the end of fill	Fill Time (s)
1	1.0	38.37	0.1	0.5	1.149	8.94	15
2	1.5	38.37	0.1	0.5	1.149	13.67	10
3	2.0	38.37	0.1	0.5	1.149	17.87	7.5
4	2.5	38.37	0.1	0.5	1.149	23.69	6

As expected, velocity and time are inversely proportional. The pressure increases rapidly with increasing velocity.

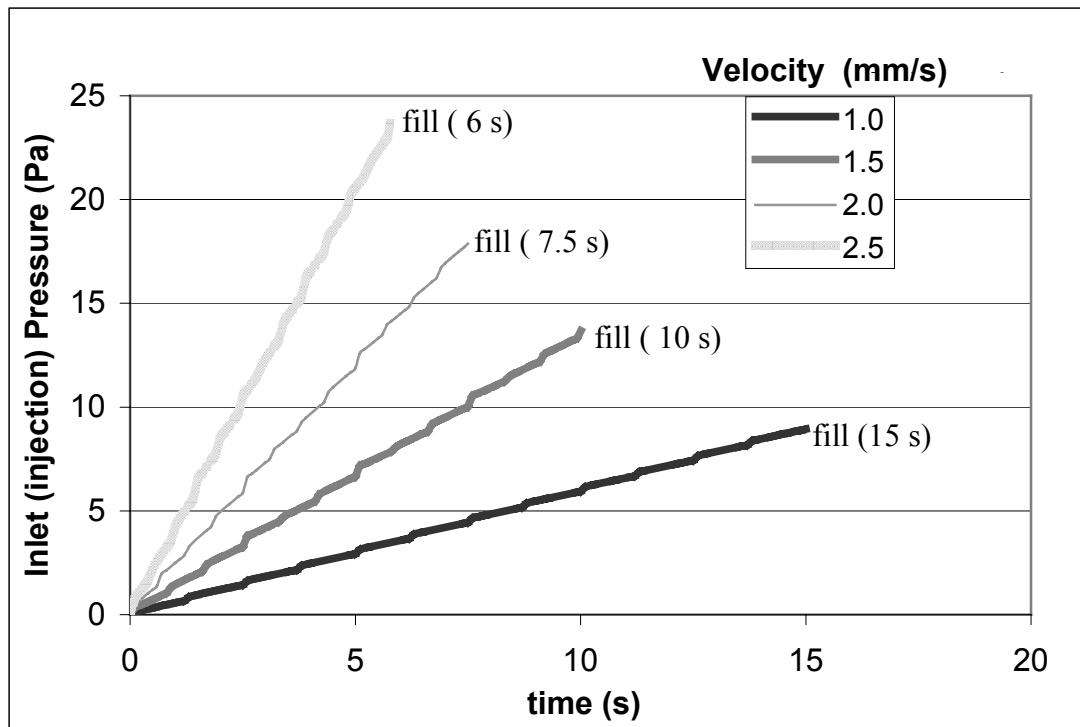


Figure 4.4 Variation in inlet pressure and fill time during one dimensional RTM under different injection velocities.

4.1.3 Viscosity Analysis

In this part, the effect of varying the resin, i.e. its viscosity, is presented. The relevant RTM run configurations and results are presented in Table 4.4. The results are also presented graphically in Figure 4.5.

Table 4.4 Process parameters and results for 1-D viscosity analysis

	u_0 (mm/s)	Permeability $K_{xx} \times 10^{-5} \text{ mm}^2$	Numerical time increment Δt (s)	Fiber Volume Fraction v_f	Resin Viscosity (Pa.s) μ	Inlet Pressure (Pa) at the end of fill	Fill Time (s)
1	1	38.37	0.1	0.5	1.149	8.94	15
2	1	38.37	0.1	0.5	2.149	16.73	15
3	1	38.37	0.1	0.5	3.149	24.51	15
4	1	38.37	0.1	0.5	4.149	32.29	15

When the viscosity is high, the impregnation of the fiber preform becomes difficult. This is accompanied by a proportional increase in inlet pressure (via Darcy's Law) as seen in Figure 4.5. As expected, there's no difference in fill times since each case has the same injection velocity and preform.

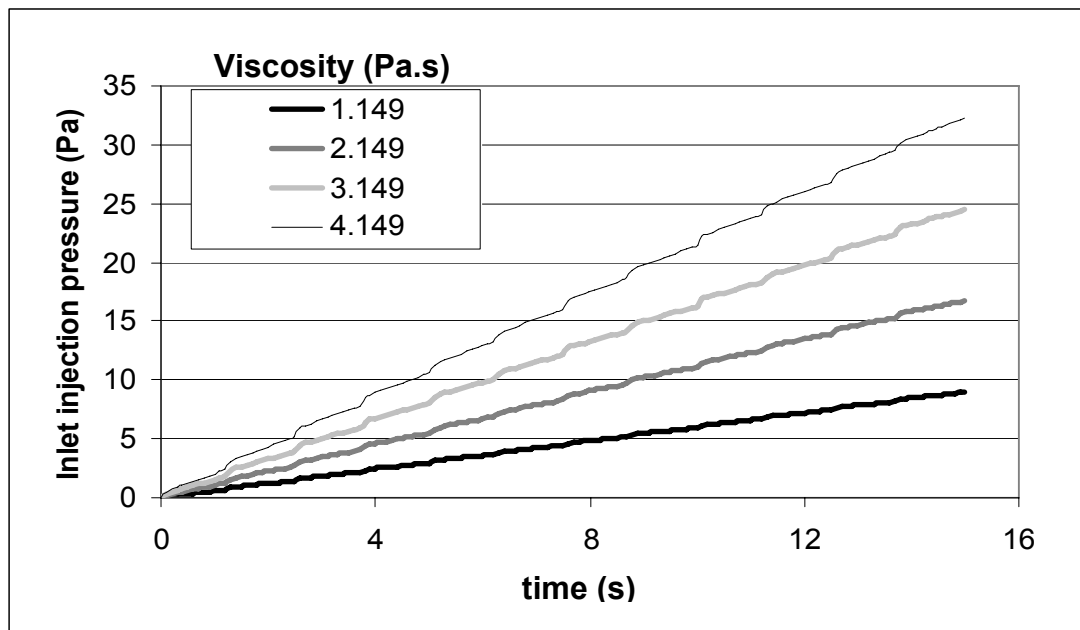


Figure 4.5 Variation of inlet pressure for one dimensional RTM under constant inlet velocity for different resin viscosities.

4.1.4 Fiber Volume Fraction Analysis

In this last portion of 1D RTM analysis; the effects of changing fiber volume fraction values are investigated. Fiber volume fractions are changed when more or less fibers (woven textiles) are packed into the mold. In effect, the changing fiber volume fraction also changes the preform permeability.

However, for the sake of the parametric analysis, the current investigation keeps preform permeability constant. The relevant RTM run configurations are presented in Table 4.5. The effect of variation of fiber volume fraction on the filling time and inlet pressure can be seen in Figure 4.6.

Table 4.5 Process parameters and results for 1-D volume fraction analysis

	u_0 (mm/s)	Permeability $K_{xx} \times 10^{-5} \text{ cm}^2$	Numerical time increment Δt (s)	Fiber Volume Fraction v_f	Resin Viscosity (Pa.s) μ	Inlet Pressure (Pa) at the end of fill	Fill Time (s)
1	1	38.37	0.1	0.4	0.5	3.89	18.00
2	1	38.37	0.1	0.45	0.5	3.89	16.50
3	1	38.37	0.1	0.5	0.5	3.89	15.00
4	1	38.37	0.1	0.55	0.5	3.88	13.50

By increasing the fiber volume fraction, the amount of empty volume inside the mold decreases and therefore less resin can fill the mold. This, in turn, decreases the fill time for the same injection rate.

As the volume fraction increases, the inlet pressure increases at a faster rate, as seen in Figure 4.6. This is expected, since an increasing fiber volume fraction implies higher resistance to flow due to decreasing flow passage area, which manifests itself in an increase inlet pressure.

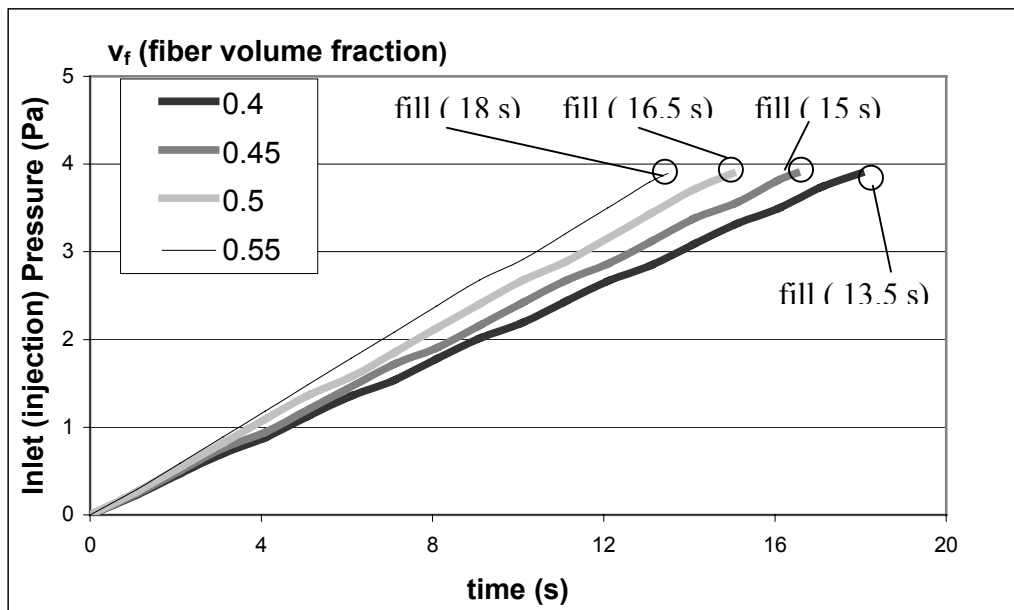


Figure 4.6 Variation in inlet pressure for one dimensional RTM under constant inlet velocity for different fiber volume fractions.

4.2 2-D RTM simulations

1-D RTM simulations presented the isolated effects of various process parameters. In addition, comparisons with exact solutions showed good agreement. In this section, RTM process analysis is extended to two dimensional resin flow configurations. The irregular mold geometry used in the 2-D simulations can be seen in Figure 4.7. This is a planar mold cavity in which the thickness of the cavity (i.e. part to be produced) is much smaller than the planar dimensions (thickness=0.2 mm). The cavity lies on a plane. Therefore, the impregnation simulations are to be performed for 2-D resin flow. The cavity shape is irregular and the location of the inlet gate can be seen in Figure 4.7. The impregnation resin front pressure will be atmospheric at all times. Though not shown, the mold model incorporates air vents to ensure this.

In this sections, the current capabilities of the code are employed to study the flow response at different resin velocities and viscosities, fiber volume fractions and permeabilities, similar to 1-D analysis, however, here, the analyses are all 2-D. Furthermore both isotropic and anisotropic preform cases are presented.

The program capabilities were extended, as part of the current study, to handle non-homogeneous preform permeabilities and fiber volume fractions within the mold. These cases can arise when different preforms (different weave, different material and/or different number of layers) are placed in the mold. The modified program is run for various nonhomogeneous scenarios. The result of the current code are also compared with the results of an impregnation experiment, to evaluate the accuracy of the simulation.

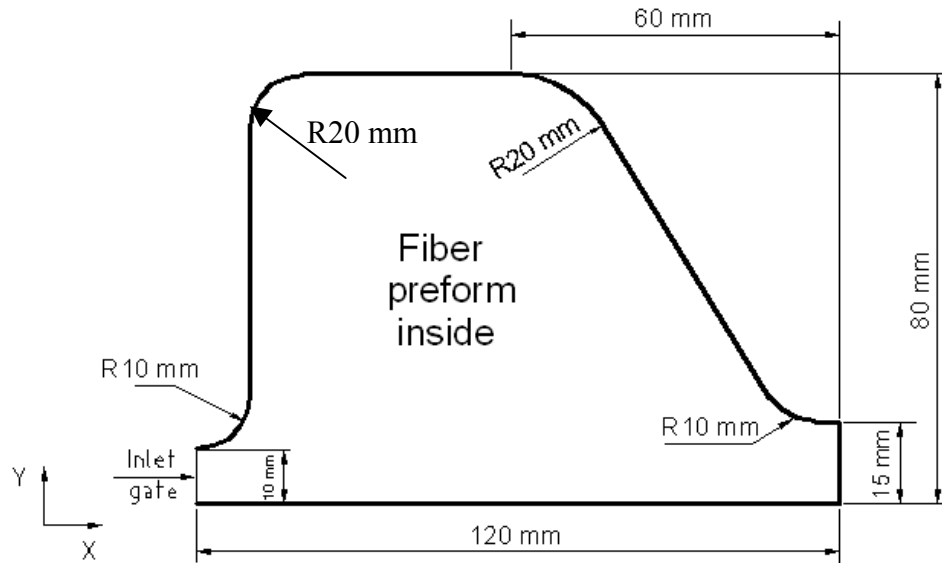


Figure 4.7 The irregular mold for 2D analysis.

4.2.1 Comparison of Model Results with Experiment

The model results are compared with an experimental case for simulation of 2-D impregnation through irregular mold geometry. The experimental data is taken from [1]. The experiment involves impregnation of pancake syrup in to a WS ES1920 angle interlock carbon preform having the shape of the irregular plate shape is show were in Figure 4.8. The viscosity and permeability values for this case were $\mu = 1.8 \text{ Pa}\cdot\text{s}$, $K_{xx} = 28.7 \times 10^{-9} \text{ mm}^2$, $K_{yy} = 6.9 \times 10^{-9} \text{ mm}^2$. The preform thickness was $h_p = 6.31 \text{ mm}$ and the inlet velocity, $u_{inlet} = 56.6 \text{ mm/s}$ during experimentation.

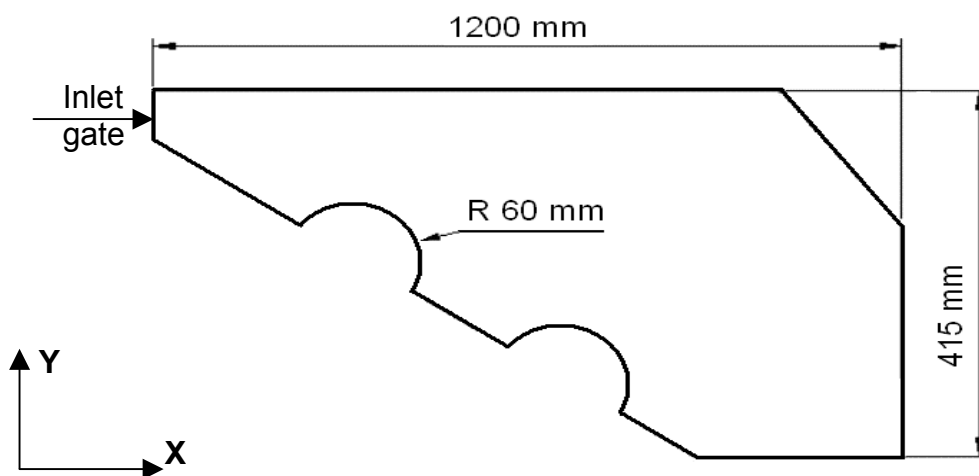


Figure 4.8 The mold cavity for model-experiment comparison

Figure 4.9 presents the results of the experiment as well as the current model. The figure shows the flows front location reached at every 37 seconds.

For the first half of the filling process, the model flow front progression lags behind the experiment. In the second half, the model flow fronts catch on with the experiment towards the end of the filling. On the upper mold wall side, the resin contact points in the model flow fronts are left behind those for the experiment. However on the lower mold wall side, the contact points for the model follow those in the experiment very closely.

The experimental filling time is $t_{fill} = 415$ s whereas the model produces a fill time of $t_{fill} = 422$ s. Even though the model lags behind at first, the overall fill time is quite close to the experimental result.

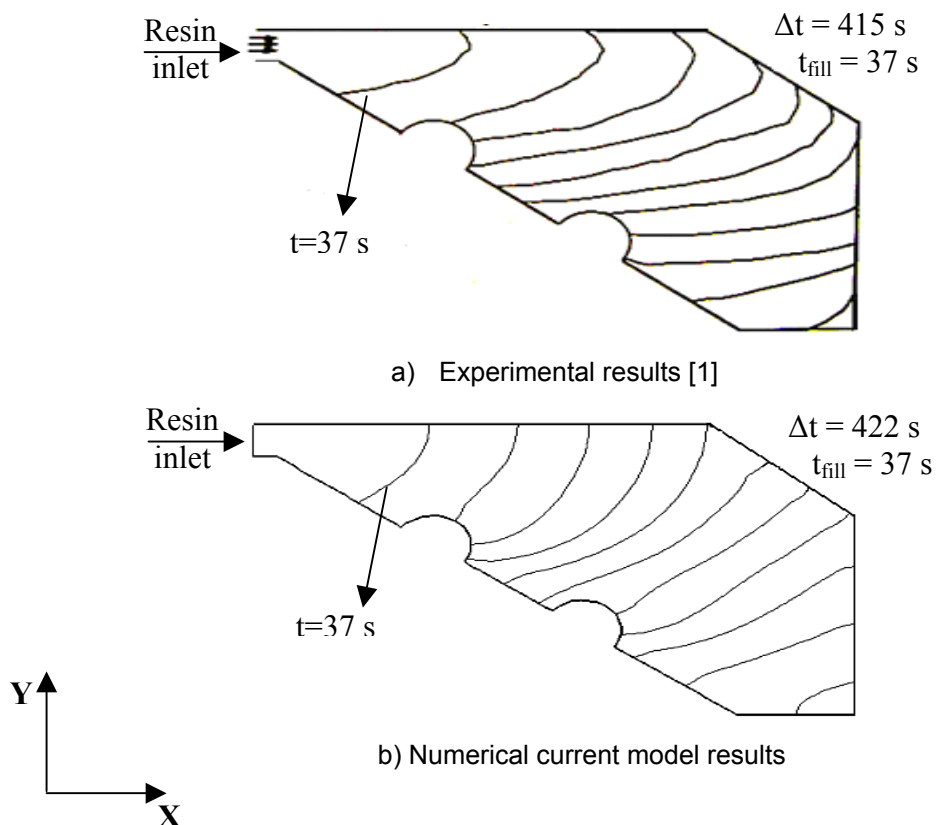


Figure 4.9 Comparison of experiment and simulation results for 2-D resin impregnation through an irregular mold geometry

4.2.2 Velocity Analysis

In this part, the effect of changing injection velocity on 2-D resin flow is studied. The four configurations (corresponding to four different velocities) are presented in Table 4.6. The presented properties for resin and fiber preform correspond to epoxy vinyl ester resin and 1523 E-glass fiber [26]. The preform is isotropic; the permeabilities in x and y directions are the same. The preform is also homogeneous, having the same fiber volume fraction and permeability, everywhere. Figure 4.10 presents various resin impregnation stages for the different velocity cases. The generated meshes at each time instance are also seen. As expected, fill time decreases with increasing velocity

Table 4.6 Process parameters for 2-D velocity analysis

	u_0 (mm/s)	Permeability $K_{xx} \times 10^{-5} \text{ mm}^2$	Permeability $K_{yy} \times 10^{-5} \text{ mm}^2$	Numerical time increment Δt (s)	Fiber Volume Fraction v_f	Resin Viscosity (Pa.s) μ	Fill Time (s)
1	1.0	4.8	4.8	0.2	0.49	0.45	360
2	1.5	4.8	4.8	0.2	0.49	0.45	240
3	2.0	4.8	4.8	0.2	0.49	0.45	180
4	2.5	4.8	4.8	0.2	0.49	0.45	140

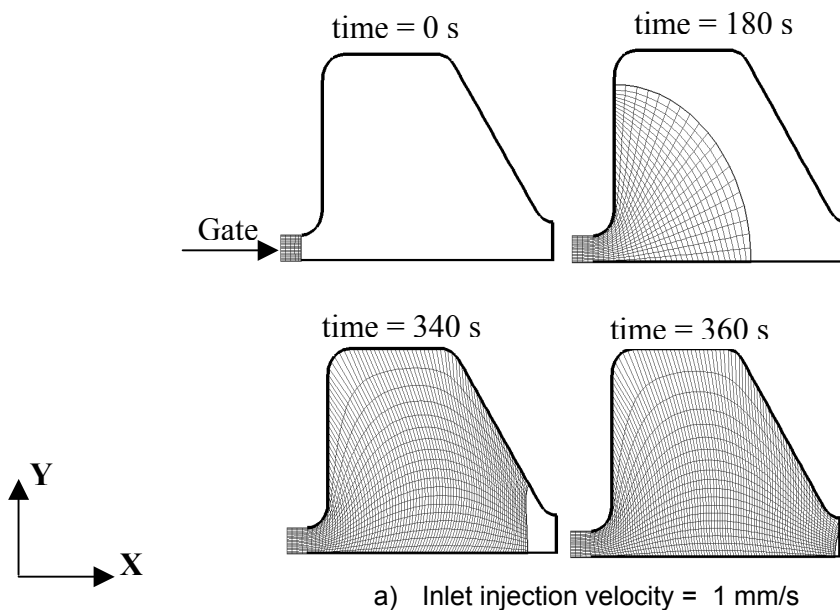


Figure 4.10 Resin flow progression and corresponding boundary fitted mesh systems for different resin inlet velocities

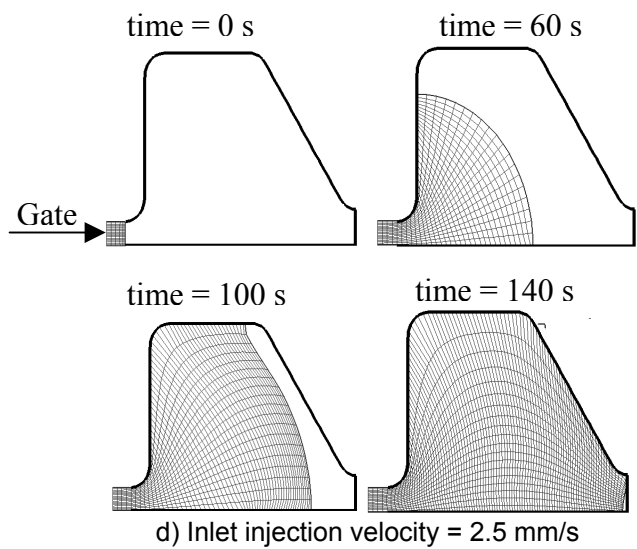
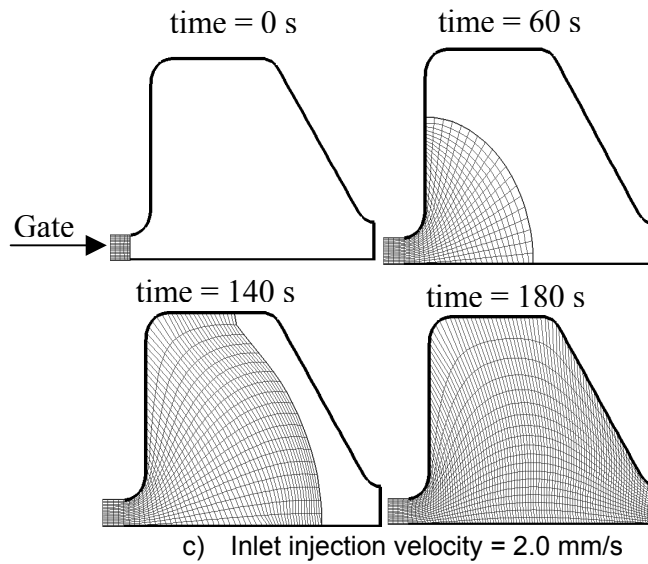
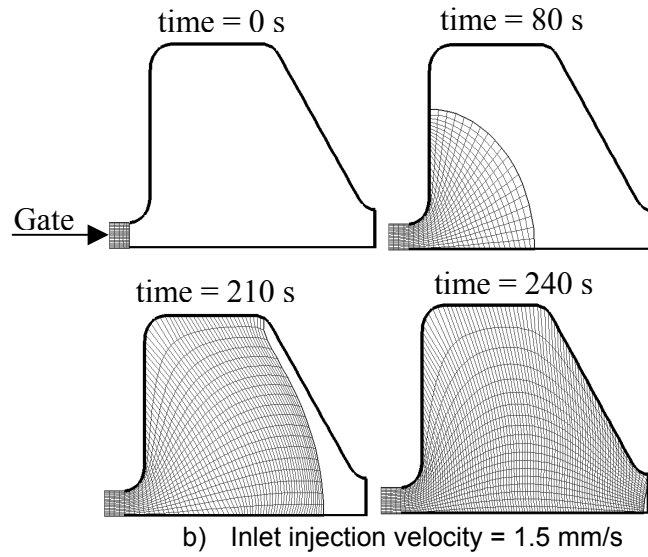


Figure 4.10 Resin flow progression and corresponding boundary fitted mesh systems for different resin inlet velocities (continued).

Figure 4.11 presents the inlet pressure variation with changing injection velocities. As in 1-D case, the pressure increases as velocity is increased. At the same time, for a given velocity, the pressure increases in three distinct patterns. An initial sharp increase followed by a gradual increase over a larger period of time, concluded by yet another sharp pressure increase. This particular trend is directly related to the mold (cavity) geometry.

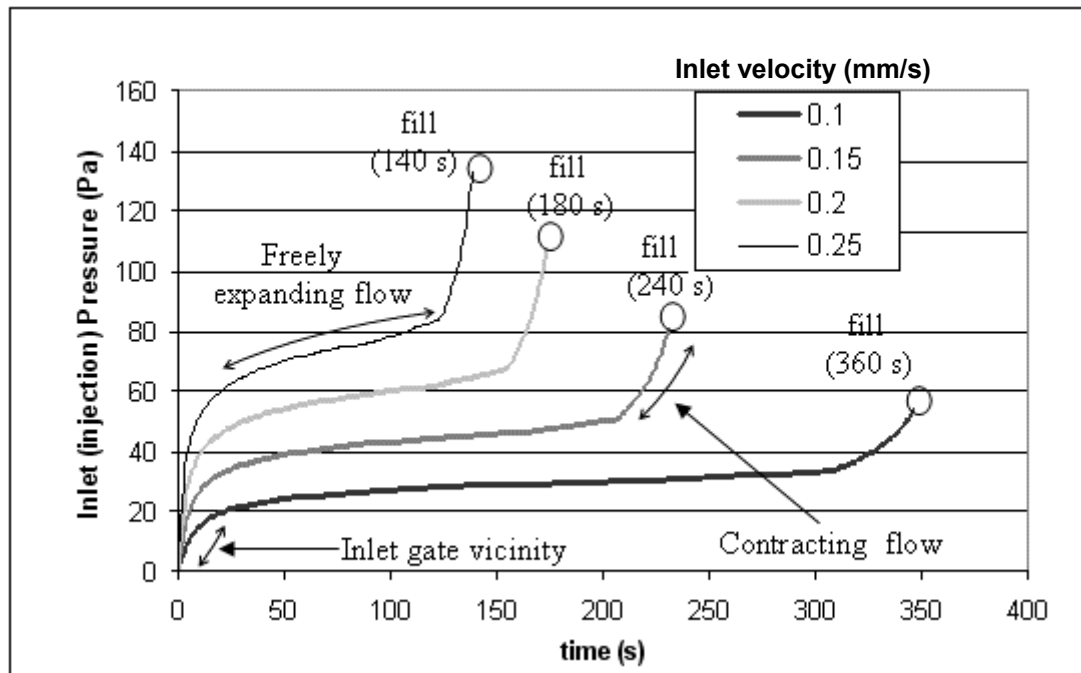
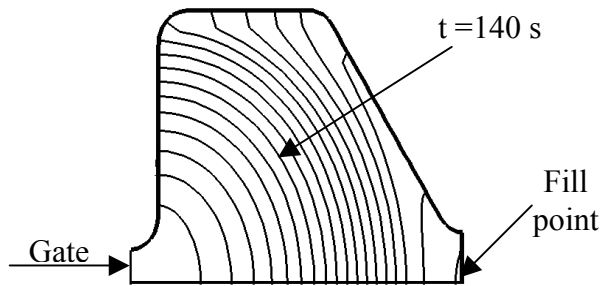


Figure 4.11 Inlet pressure variations at different inlet velocities

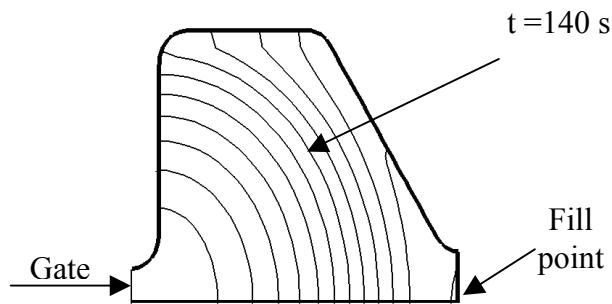
At first, the resin enters the mold through a relatively small flow channel, the inlet gate. But once in the cavity, the resin is free to expand in an unrestricted manner, i.e. circular patterns. These two regions of flow fronts are observed in the first two pressure regimes, as stated in Figure 4.11.

As the resin continues to fill the mold, the front eventually reaches the contracting boundary on the right side. This restricts the movement of the resin, resulting in a converging flow raising the pressure rapidly until fill. This is the final stage of pressure rise. With a different mold gate geometry, the pressure rise patterns will also change. In Figure 4.11, as the inlet velocity

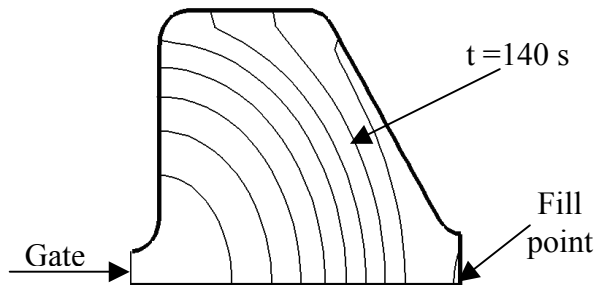
increases, the pressure rise pattern shifts up (due to increased pressure), but also contracts to the left (due to decreased fill time).



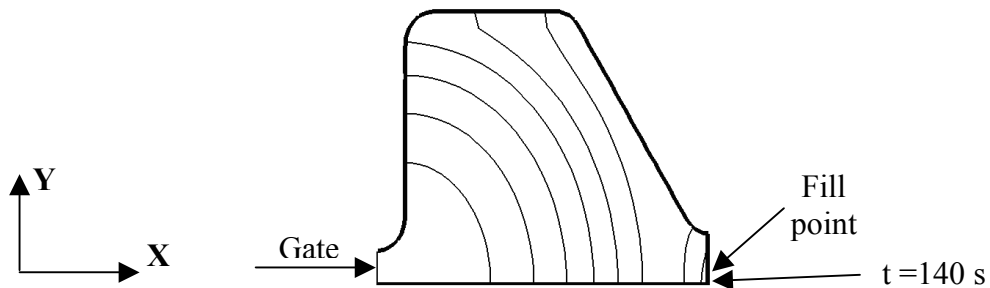
a) Inlet injection velocity = 1 mm/s; Fill time = 360 s; $\Delta t = 20$ s



b) Inlet injection velocity = 1.5 mm/s; Fill time = 240 s; $\Delta t = 20$ s



c) Inlet injection velocity = 2.0 mm/s; Fill time = 180 s; $\Delta t = 20$ s



d) Inlet injection velocity = 2.5 mm/s; Fill time = 140 s; $\Delta t = 20$ s

Figure 4.12 Flow front progressions for varying injection velocity.

The flow front progression for the different injection velocities are presented in Figure 4.12. The time increments for recording the front locations (Figure 4.12) are the same in all cases (20 s). The flow fronts are situated further away from one another, at higher flow rates, as expected. Other than this, there doesn't seem to be any difference between shapes of the fronts, including the final fill point (at the lower-right corner of mold, as marked).

The pressure distribution in the mold at the instant of fill, for different injection velocities, can be seen in Figure 4.13. Pressure distribution goes to the dark gray scale to the light form of the color because of the increasing velocity.

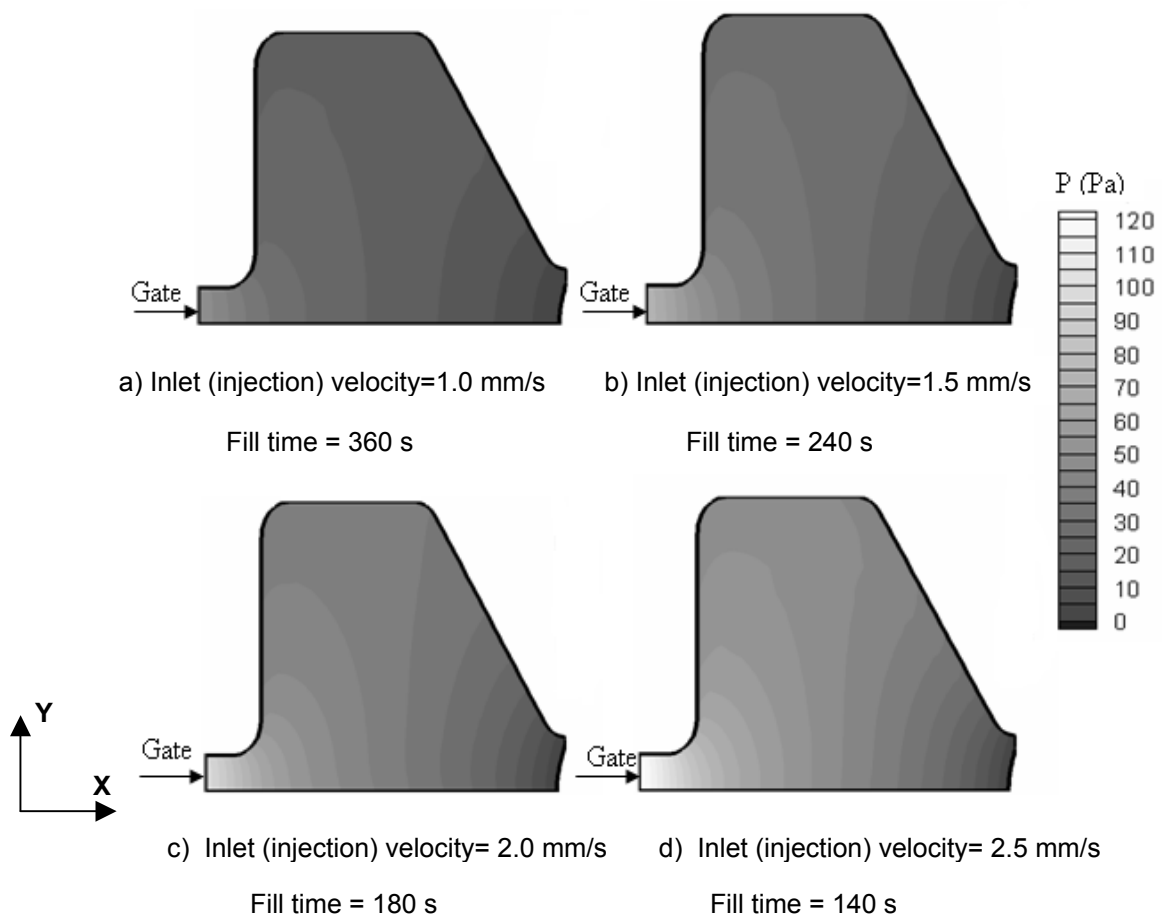


Figure 4.13 Pressure distributions at the instance of fill for varying injection velocity conditions.

Because of the restrictive geometry of the inlet and outlet regions of the mold, the pressure change is more rapid here than that in the middle of the

mold. As inlet velocity increases, there is a larger pressure variation (higher pressure) as expected.

4.2.3 Viscosity Analysis

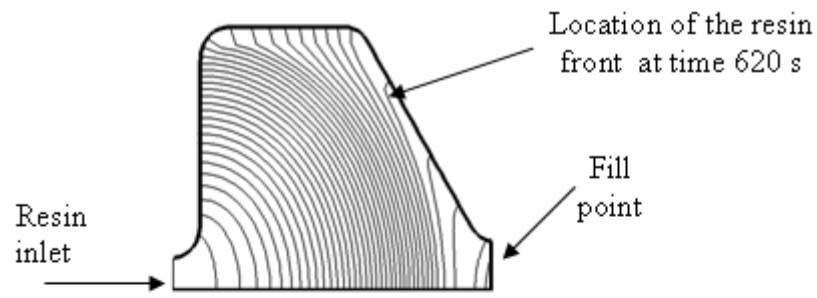
In this part, the effect of changing resin viscosity on 2-D resin impregnation is studied. The four simulation configurations (corresponding to four different resin viscosities) are presented in Table 4.7. The preform properties are those of 1523 E-glass. The four viscosities correspond to four types of epoxy vinyl ester ; L-10, SC-36, 510 A-40 and 976 [24].

Table 4.7 Process Parameters for 2-D Viscosity Analysis

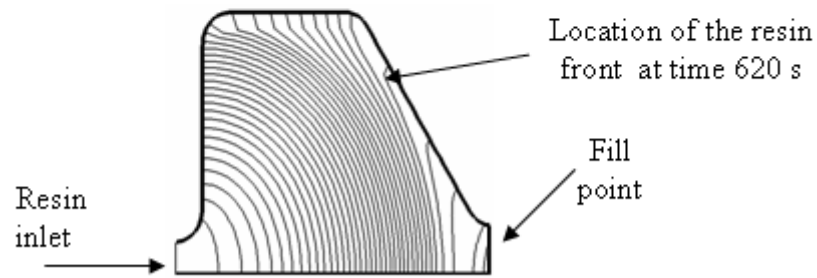
	u_0 (mm/s)	Permeability $K_{xx} \cdot 10^{-5} \text{ mm}^2$	Permeability $K_{yy} \cdot 10^{-5} \text{ mm}^2$	Numerical time Increment. Δt (s)	Fiber Volume Fraction v_f	Resin Viscosity (Pa.s) μ	Fill Time (s)
1	0.5	4.8	4.8	0.2	0.5	0.15	706
2	0.5	4.8	4.8	0.2	0.5	0.25	706
3	0.5	4.8	4.8	0.2	0.5	0.45	706
4	0.5	4.8	4.8	0.2	0.5	1.06	706

The fill times are identical for the four cases. Since the viscosity is homogeneous everywhere and the inlet injection velocities are the same, the flow front progressions are also identical as can be observed in Figure 4.14. The time increment for recording to the flow front is 20 s in all cases.

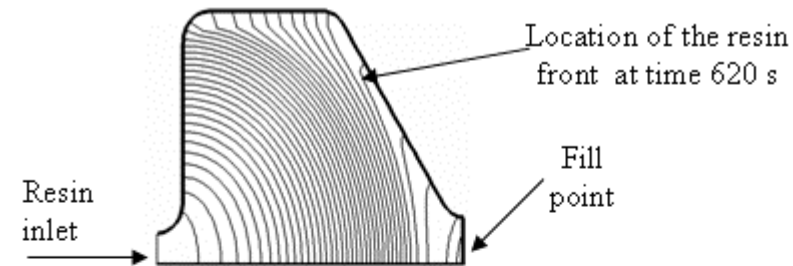
The viscosities are most effective on flow pressure through Darcy's Law, as can be seen from Figure 4.15. The same fast-slow-fast inlet pressure increase rate behavior observed in Figure 4.11, is also observed here. The main difference is the vertical shifting of the curves - higher pressure values for higher viscosities. The pressure distribution inside the mold cavity at the instant of fill for different resin viscosities are presented in Figure 4.16.



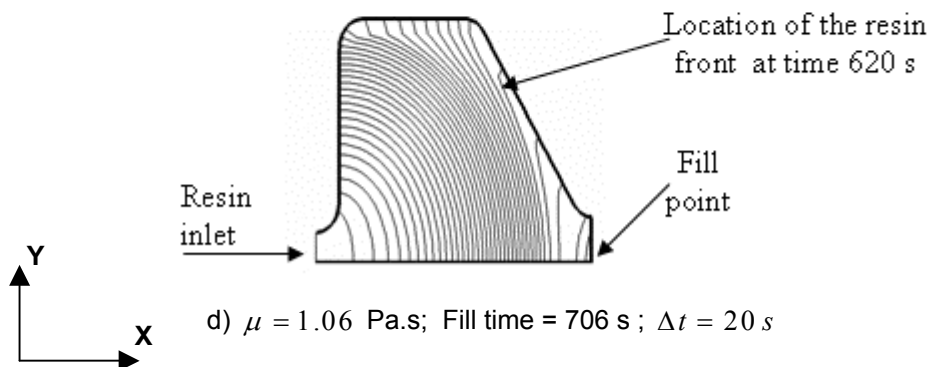
a) $\mu = 0.15$ Pa.s; Fill time = 706 s ; $\Delta t = 20$ s



b) $\mu = 0.25$ Pa.s; Fill time = 706 s ; $\Delta t = 20$ s



c) $\mu = 0.45$ Pa.s; Fill time = 706 s ; $\Delta t = 20$ s



d) $\mu = 1.06$ Pa.s; Fill time = 706 s ; $\Delta t = 20$ s

Figure 4.14 Flow front progressions for different resin viscosities at constant injection rates. (Flow fronts plotted every $\Delta t = 20$ s time increment)

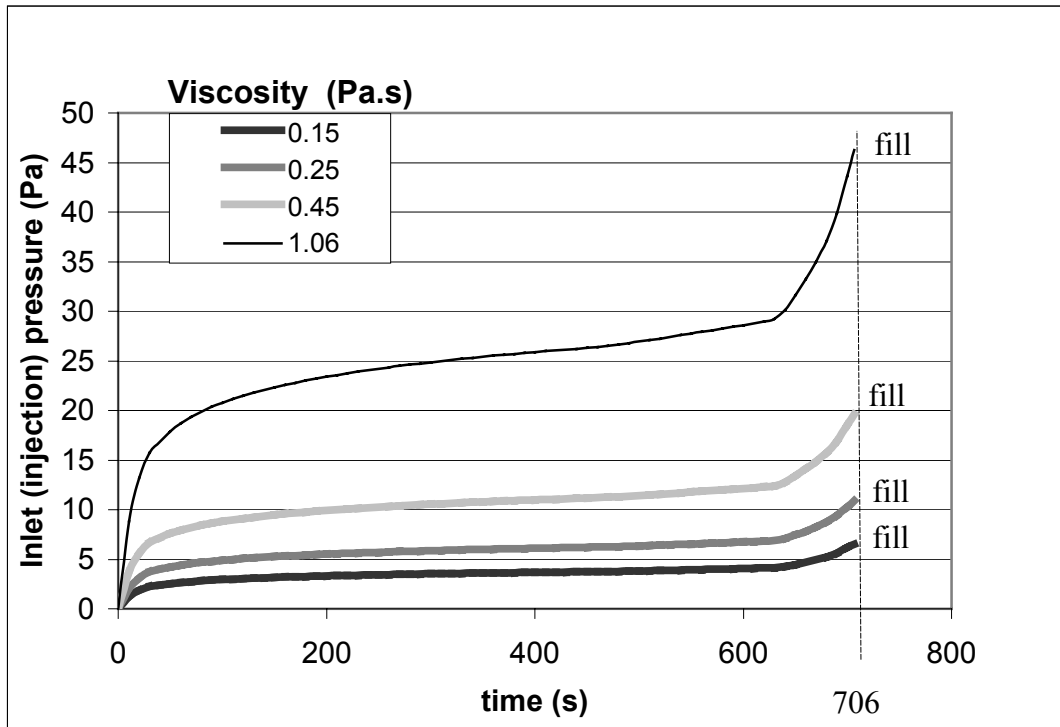


Figure 4.15 Inlet pressure variations at different inlet viscosities for constant injection rates.

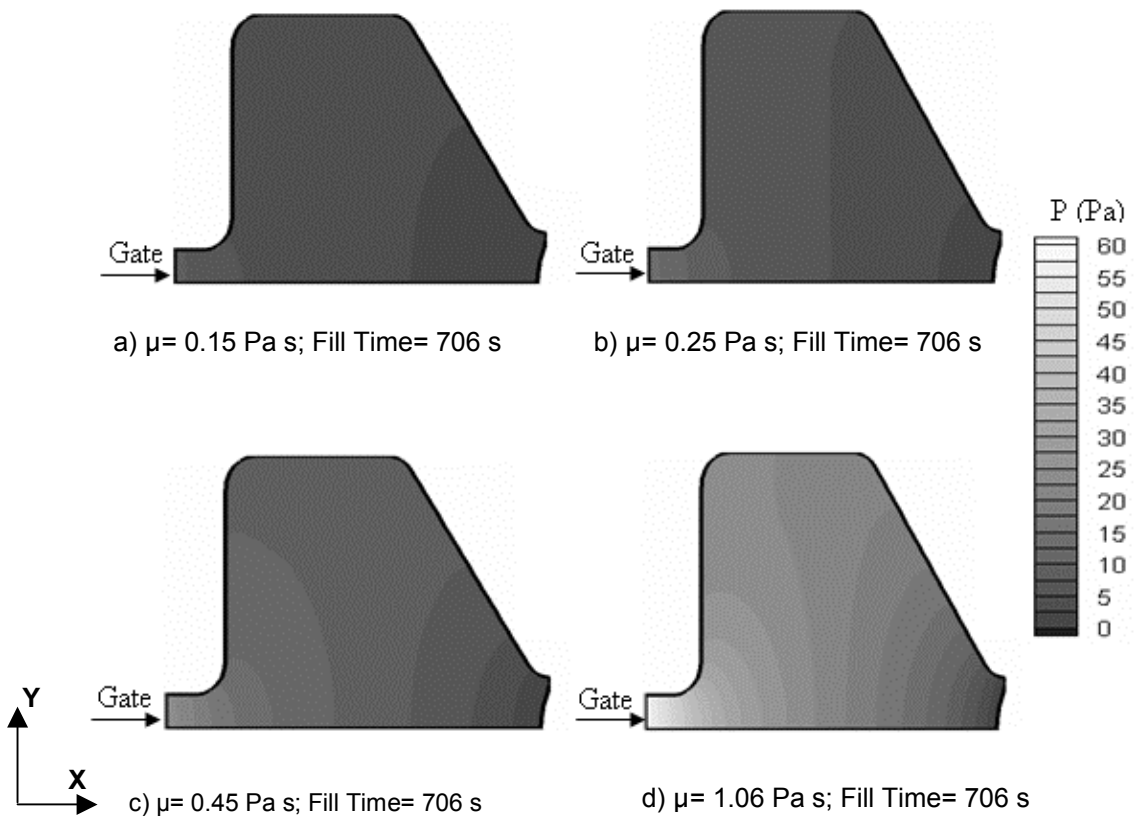


Figure 4.16 Pressure distributions at the instance of fill for different resin viscosities at constant injection rates.

According to Darcy's Law, increased viscosity should result in increased pressure, at the same flow rate. This is observed in Figure 4.16.

4.2.4 Fiber Volume Fraction Analysis

In this part, the effect of changing fiber volume fraction on 2D resin impregnation is studied. Unlike the previous results, there are two parts in this case: the first part deals with homogeneous fiber volume fraction distributions in the entire cavity. The second part investigates non-homogeneous fiber volume fraction distributions within the mold, which is a capability developed and added to the program as part of the current research.

4.2.4.1 Homogeneous Fiber Volume Fraction

In this part, the preform in the mold cavity is homogeneous. The effect of changing the homogeneous preform fiber volume fraction on resin impregnation is studied. The four run configurations (corresponding to four different fiber volume fractions) are presented in Table 4.8. The presented data corresponds to 1523 E-glass fiber and 976 epoxy resin [24].

Table 4.8 Process Parameters for 2-D Volume Fraction Analysis

	u_0 (mm/s)	<i>Permeability</i> $K_{xx} \times 10^{-5} \text{ mm}^2$	<i>Permeability</i> $K_{yy} \times 10^{-5} \text{ mm}^2$	Numerical time Increment. Δt (s)	Fiber Volume Fraction v_f	Resin Viscosity (Pa.s) μ	Fill Time (s)
1	0.2	4.8	4.8	0.2	0.40	1.06	416
2	0.2	4.8	4.8	0.2	0.45	1.06	382
3	0.2	4.8	4.8	0.2	0.50	1.06	340
4	0.2	4.8	4.8	0.2	0.55	1.06	312

Figure 4.17 presents the progression of flow fronts at different fiber volume fractions. As the fiber volume fraction increases, the amount of empty volume

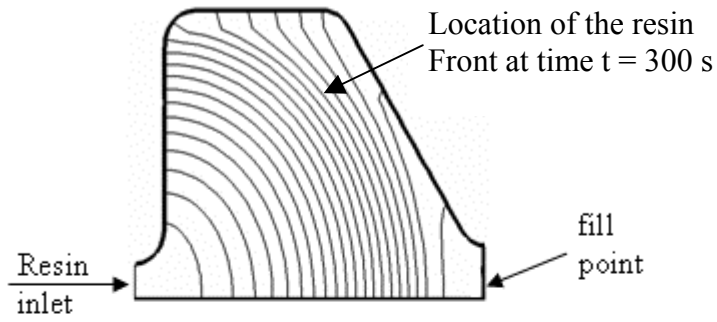
inside the mold cavity decreases and less resin can fill the mold, which decreases the fill time. This is observed from Figure 4.17. As the fiber volume fraction increases from (a) to (d), the fill time decreases from 416 s to 312 s.

Figure 4.18 presents the variation in inlet pressure at different fiber volume fractions. There does not seem to be much difference except shifting of the curves to the right due to different fill times. In reality, as the fiber volume fraction increases, the flow pressure increases due to decreased permeability (more fibers lead to less permeable domain). However, in the current simulation, the permeability values are kept the same for all fiber volume fractions. Hence, the pressure values are not higher at high fiber volume fractions but simply, the curves are shifted to the left due to reduced fill times.

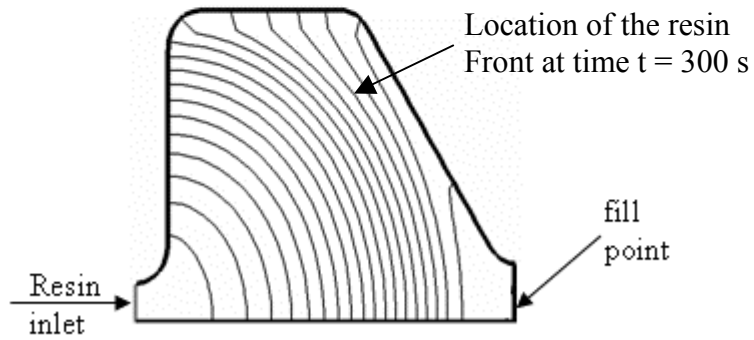
For the same reason, the pressure distributions in the mold cavity at the instance of fill are identical for all cases (they are not shown here). For a realistic modeling, the permeability and fiber volume fraction should be related to one another (through various porous medium models available in literature, such as Kozeny-Karman relation [27]). The changes in fiber volume fraction would reflect on pressure distribution and inlet pressure, approximating the actual effect more accurately.

4.2.4.2 Non homogeneous Fiber Volume Fraction

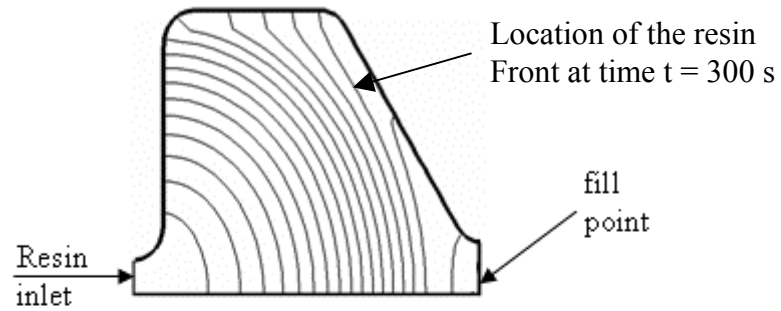
In this part, the effect of non-homogeneous fiber volume fraction distribution within the mold cavity is investigated. Such cases arise when different fiber fabrics are used together to form the preform, when different number of layers of fabrics are placed in the cavity or when the part (and hence, cavity) thickness is changing. In the current analysis, the same 2-D mold of Figure 4.7 is divided into different volume fraction regions, yielding a non-homogeneous preform, and the results are compared with the homogeneous case. The simulation configurations are presented in Table 4.9



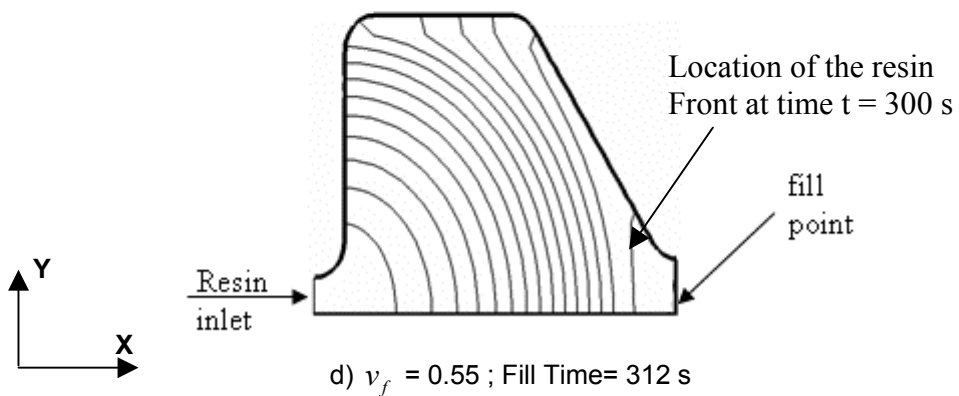
a) $v_f = 0.4$; Fill Time= 416 s



b) $v_f = 0.45$; Fill Time= 382 s



c) $v_f = 0.5$; Fill Time= 340 s



d) $v_f = 0.55$; Fill Time= 312 s

Figure 4.17 Flow front progressions for different fiber volume fractions (homogeneous preform) at constant resin injection rate. (Flow fronts plotted every $\Delta t = 20$ s time increment)

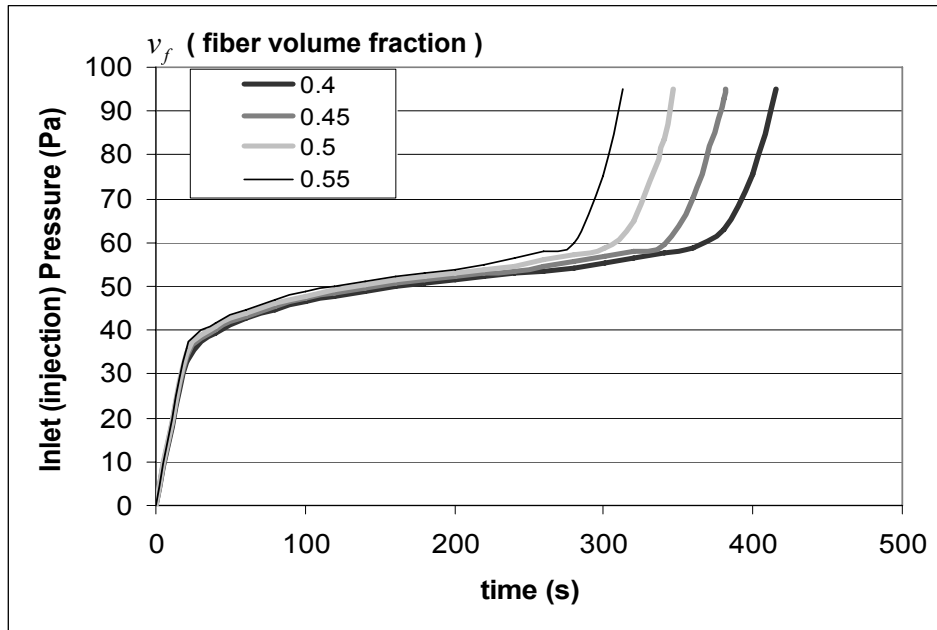


Figure 4.18 Inlet pressure rise with time at different volume fractions.

The sections refer to parts of the preform with different fiber volume fraction values, as presented in Table 4.9. Case-2 and Case-3 present fiber volume fraction variations in different directions. Case 1 refers to the simulation with homogeneous preform, serving as a base case for comparison. Table 4.9 presents the fill times at the end of simulations. The area average fiber volume fractions in case 2 and case 3 are less than 0.5 cm. Thus, the homogeneous case ($v_f = 0.5$) has the fastest fill expected. On the other hand, the fill times for the two nonhomogeneous preform are different.

Table 4.9 Process Parameters for 2-D Non-homogeneous Volume Fraction Analysis

Case #	u_0 (mm/s)	Section Number	Fiber Volume Fraction v_f	<i>Permeability</i> $K_{xx} \times 10^{-5} \text{ mm}^2$	<i>Permeability</i> $K_{yy} \times 10^{-5} \text{ mm}^2$	Numerical time increment Δt (s)	Resin Viscosity (Pa.s) μ	Fill Time (s)
1	0.5	Homogeneous	0.50	4.8	4.8	0.02	1.06	692
2	0.5	1	0.40	4.8	4.8	0.02	1.06	718
	0.5	2	0.45	4.8	4.8	0.02	1.06	
	0.5	3	0.50	4.8	4.8	0.02	1.06	
	0.5	4	0.55	4.8	4.8	0.02	1.06	
3	0.5	1	0.40	4.8	4.8	0.02	1.06	747
	0.5	2	0.45	4.8	4.8	0.02	1.06	
	0.5	3	0.50	4.8	4.8	0.02	1.06	
	0.5	4	0.55	4.8	4.8	0.02	1.06	

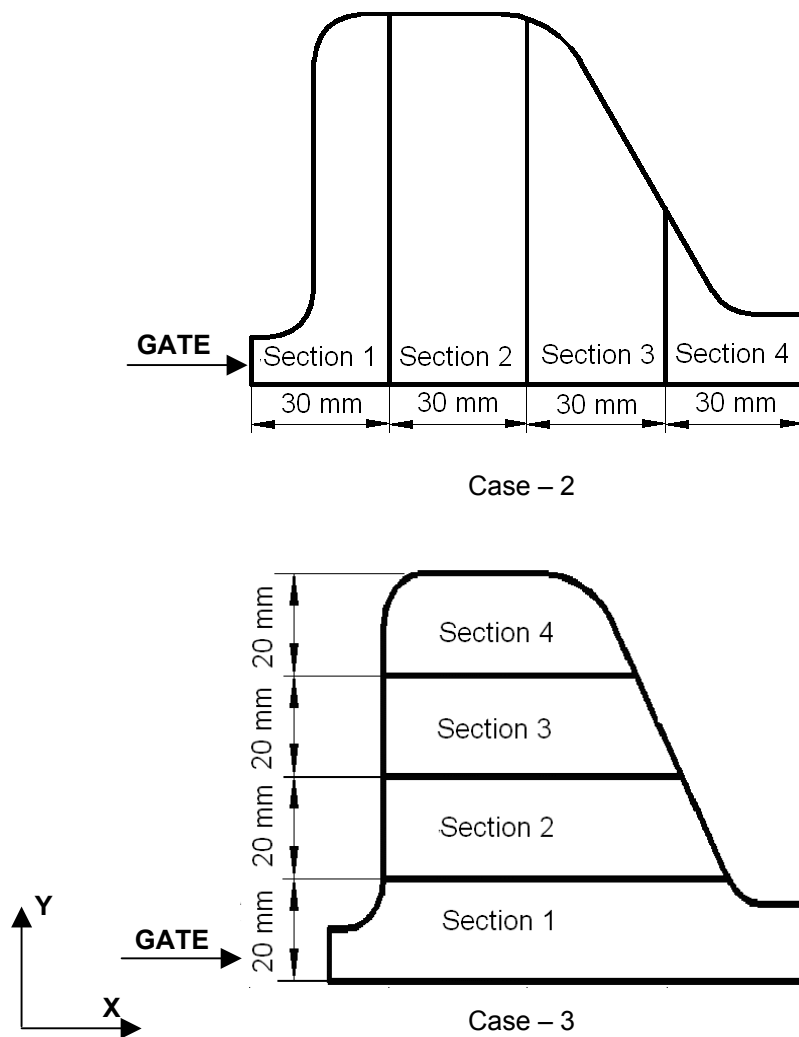
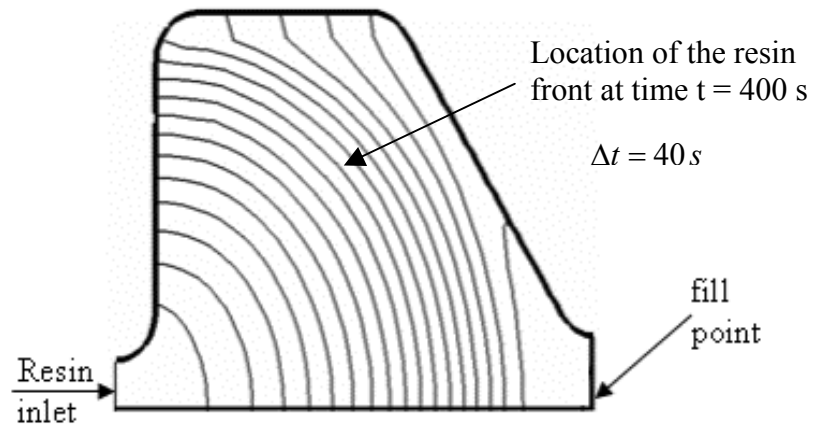


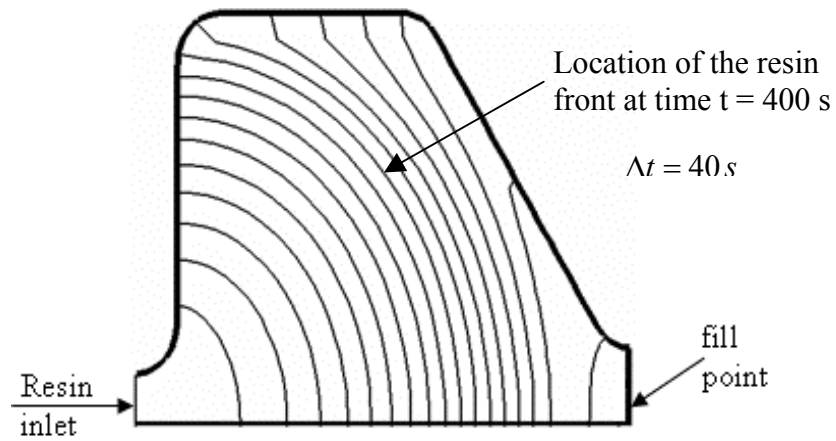
Figure 4.19 Non homogeneous preform configurations for simulations in cases 2 and 3.

Figure 4.20 presents the resin flow front progressions for the three cases. Due to the constancy of permeabilities there are only slight differences between the cases, even though the fiber volume fractions differ, similar to section 4.2.4.1. The differences are especially prominent on the converging side wall.

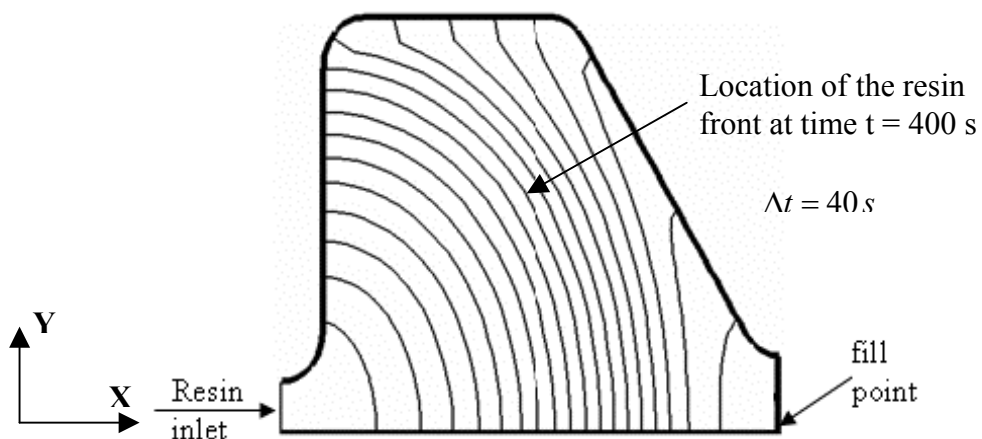
The variations of inlet pressure for the three cases are shown in Figure 4.21. Again, the major difference between the three cases is the fill time. However, inlet pressure in Case 3 simulation shows a more gradual increase rate at the final “fast rise” stage of the fast-slow-fast pressure rise trend than the other two cases.



a) Case-1; Homogeneous preform $v_f = 0.5$; Fill time = 692 s



b) Case-2; Non-homogeneous preform $v_f = 0.4-0.55$; Fill time = 718 s.



c) Case-3; Non-homogeneous preform $v_f = 0.4-0.55$; Fill time = 740 s.

Figure 4.20 Flow front progressions for isotropic, homogeneous and non-homogeneous fiber volume fraction (flow fronts plotted every $\Delta t = 40$ s time increment)

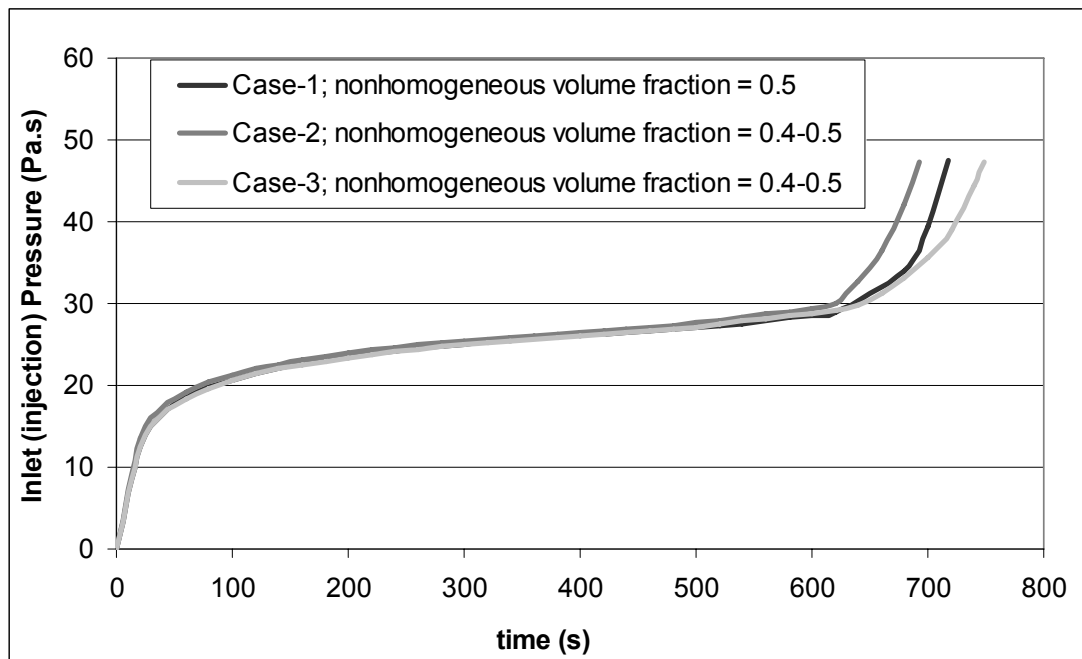


Figure 4.21 The change in inlet pressure with time according to the different volume fraction conditions

The pressure distribution in the mold cavity at the instant of fill for the three cases can be seen in the Figure 4.22. Cases 1 and 3 are more similar to one another during the first half of the impregnation. Towards the fill, near the right corner of the mold, the pressure profiles for the three cases look similar.

4.2.5 Permeability Analysis

In this part, the effect of preform permeability on 2D resin flow is studied. There are three parts to this study. The first part deals with homogeneous and isotropic preform permeability in the entire mold cavity. The second part investigates homogeneous and anisotropic preform permeability and the last part, non-homogeneous and anisotropic preform permeability distribution within the mold, which is a capability developed and added to the program as part of the current research.

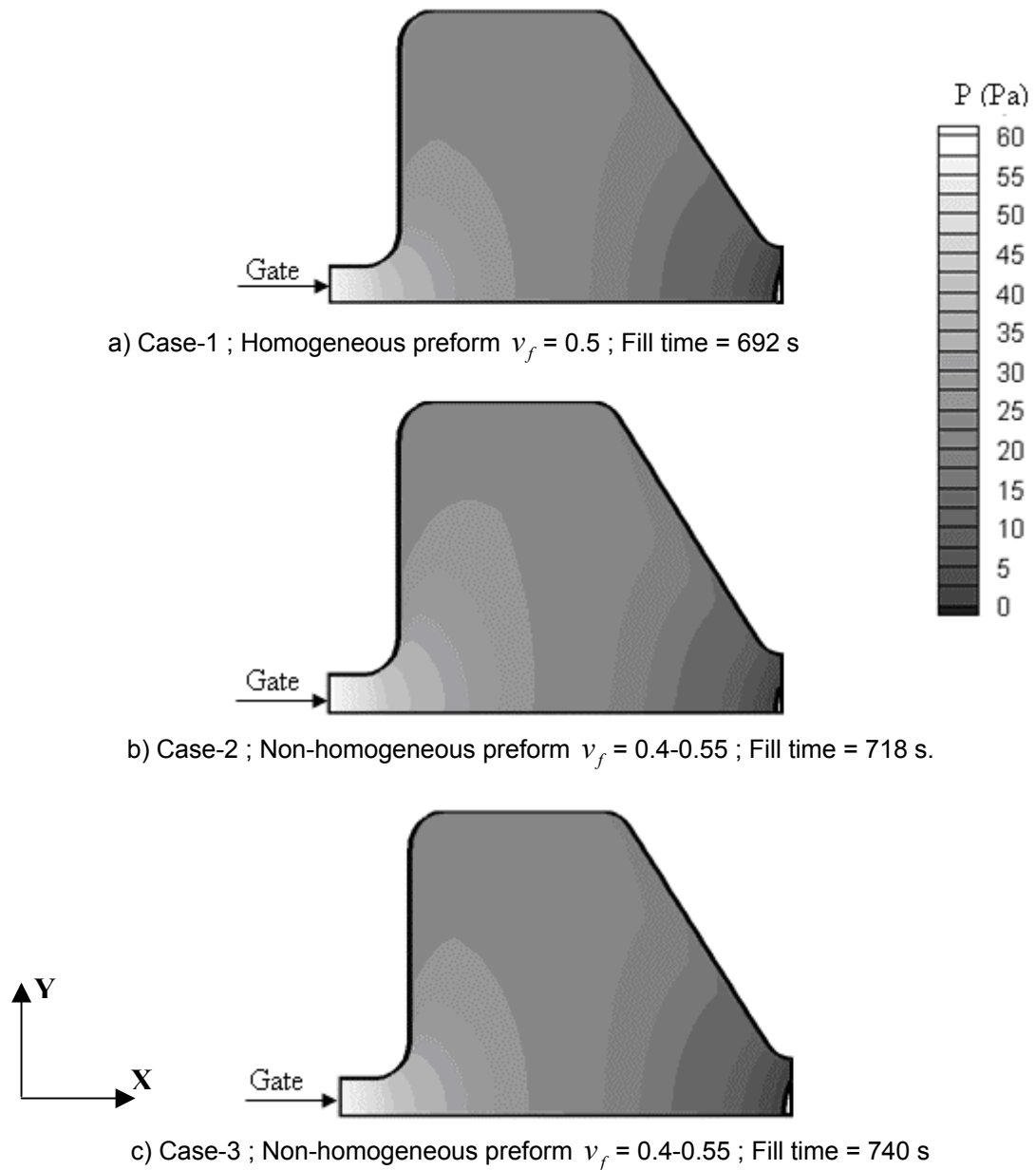


Figure 4.22 Pressure distributions at the instance of fill for homogeneous and non-homogeneous fiber volume fraction preform at constant injection rate.

4.2.5.1 Homogeneous and Isotropic Preform Permeability

Isotropic preform permeability implies, at any location, the preform exhibits the same permeability to an impregnating resin at every direction. Homogeneous permeability implies the permeability characteristics do not change from one location to another in the preform (though the permeability can be isotropic or anisotropic). In this part, the 2D analysis is based on

isotropic ($K_{xx} = K_{yy}$) and homogeneous ($K_{xx} \neq K_{xx}(x, y), K_{yy} \neq K_{yy}(x, y)$) permeability. The simulation configurations (corresponding to the three different permeability values) are presented in Table 4.10. The preform materials data is taken from [1].

Table 4.10 Process parameters for 2-D homogeneous and isotropic preform permeability analysis.

	u_0 (mm/s)	Permeability $K_{xx} \times 10^{-5} \text{ mm}^2$	Permeability $K_{yy} \times 10^{-5} \text{ mm}^2$	Numerical time Increment. Δt (s)	Fiber Volume Fraction v_f	Resin Viscosity (Pa.s) μ	Fill Time (s)
1	1	4.8	4.8	0.1	0.5	0.45	346.8
2	1	18.81	18.81	0.1	0.5	0.45	346.8
3	1	29.7	29.7	0.1	0.5	0.45	346.8

The fill times are identical for the same fiber volume fraction and injection rates as seen from Table 4.10. As a result, the impregnation flow front progressions are also identical and not shown here.

The effect of permeability change is observed directly in flow pressure. Figure 4.23 presents the inlet pressure variation with different permeability values. As expected, the inlet pressure rise is significant as the permeability decreases via Darcy's law. The linearity of inverse proportionality between permeability and pressure can be observed directly. For instance, about four times a permeability increase "4.8 to $18.81 \times 10^{-5} \text{ mm}^2$ " results in pressure dropping to about 1/4th its value.

The pressure distributions in the mold at the instance of fill can be seen in the Figure 4.24. The increase in overall pressure values observed at lower permeabilities, is consistent with the results of Figure 4.23.

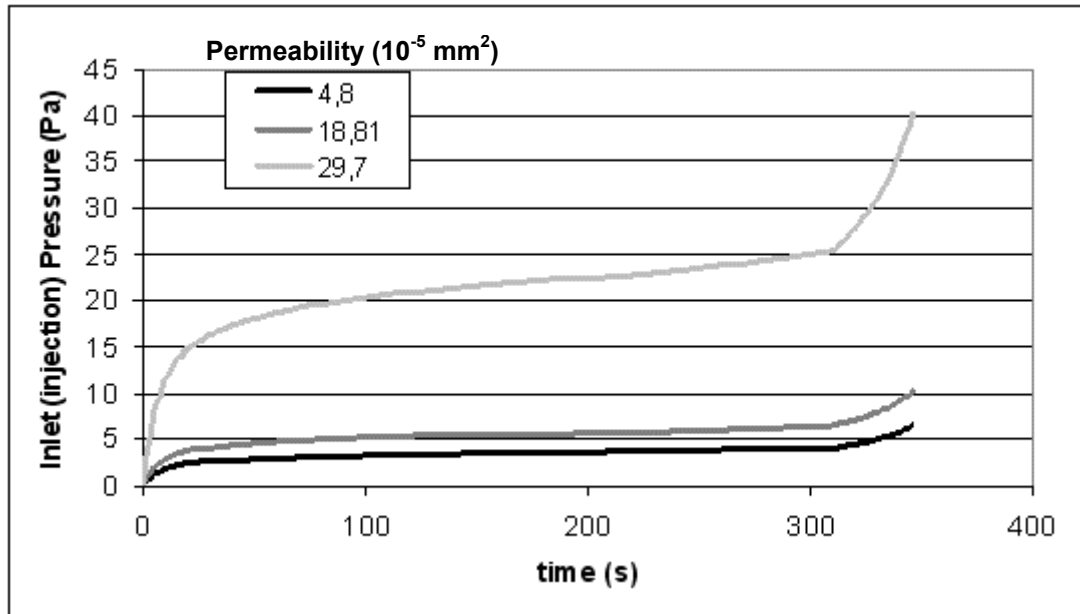


Figure 4.23 Inlet pressure variations for different values of homogeneous and isotropic preform permeability at constant injection rates.

4.2.5.2 Homogeneous and Anisotropic Preform Permeability

In this part, the 2-D impregnation analysis is based on homogeneous ($K_{xx} \neq K_{xx}(x, y), K_{yy} \neq K_{yy}(x, y)$) but anisotropic ($K_{xx} \neq K_{yy}$) preform permeability. The simulation configurations are presented in Table 4.11. The preform anisotropy is implemented by various K_{xx} / K_{yy} ratios as shown. The material data 1523 E-glass and 510-A40 are obtained from [26].

Table 4.11 Process parameters for 2-D homogenous and anisotropic preform permeability analysis

	u_0 (mm/s)	Permeability $K_{xx} \times 10^{-5} \text{ mm}^2$	Permeability $K_{yy} \times 10^{-5} \text{ mm}^2$	Numerical time Increment. Δt (s)	Fiber Volume Fraction v_f	Resin Viscosity (Pa.s) μ	Fill Time (s)
1	0.4	2.0	1.0	0.1	0.5	0.5	865
2	0.4	2.0	4.0	0.1	0.5	0.5	873
3	0.4	2.0	10.0	0.1	0.5	0.5	880

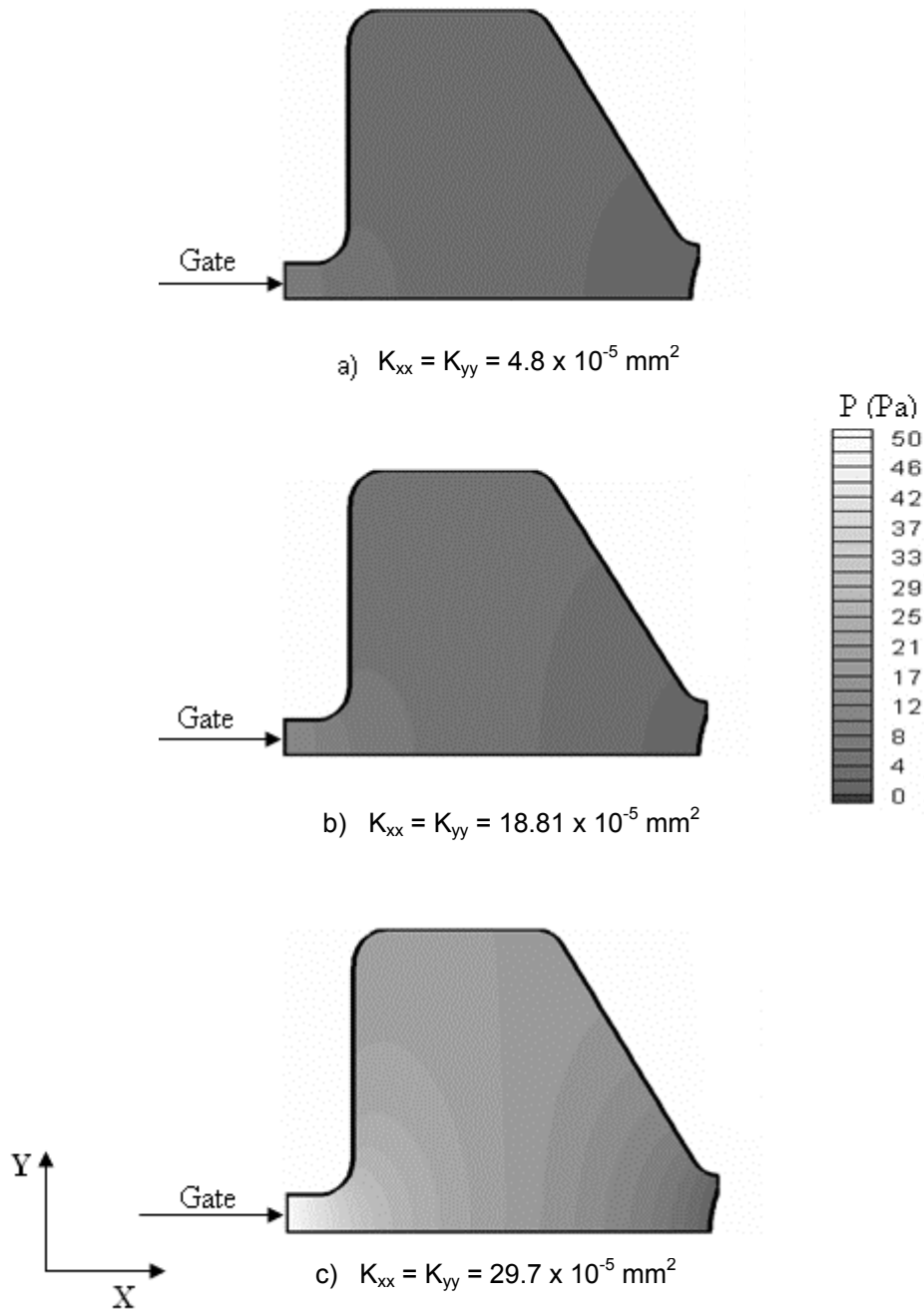


Figure 4.24 Pressure distributions at the instance of fill for different values of homogeneous and isotropic preform permeability at constant injection rates.

As seen from Table 4.11, there is a slight difference in fill times even though the fiber volume fraction and injection rates are the same. Figure 4.25 compares the shape and location of resin flow fronts at two time instances. The flow domains are marked by the boundary-fitted mesh system. As the K_{xx}/K_{yy} ratio decreases, the flow domain becomes more permeable

(comparatively) in y direction (or less permeable in x direction). Since the resin flows more easily in the direction of smaller resistance (larger permeability), this effect is immediately observed in the fronts. As K_{xx} / K_{yy} decreases, the shape of the front becomes more “vertical”. It is important to note that at any time instant, the planar areas occupied by the meshes for the different permeability simulations are approximately the same.

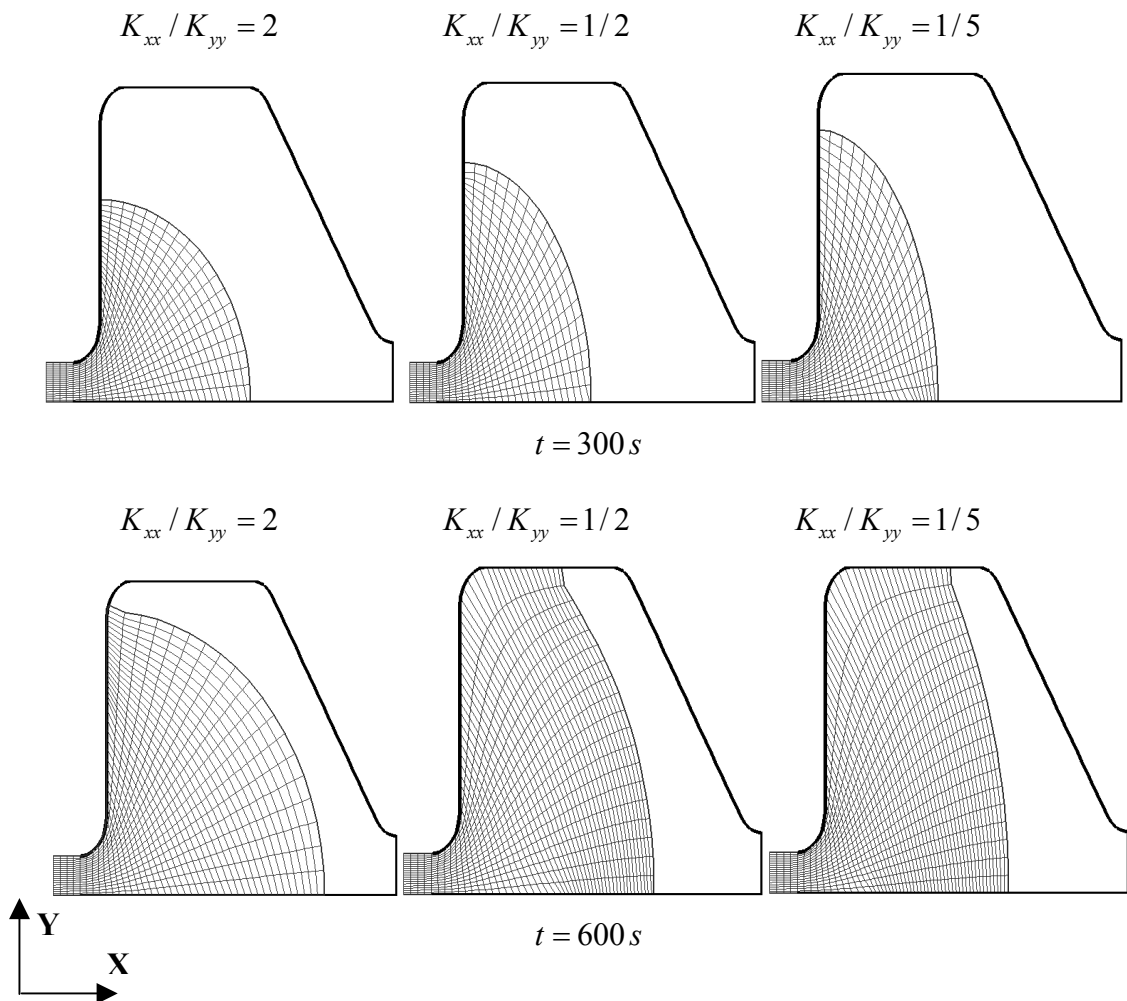


Figure 4.25 Comparison of the flow fronts at two time instances, for homogeneous, anisotropic preform permeability at constant injection rate.

The same results can be observed in flow front progressions, depicted in Figure 4.26. The flow fronts become more “vertical” as K_{xx} / K_{yy} decreases. The difference is most apparent near the mold wall on the right side. In fact, for $K_{xx} / K_{yy} = 2$, the cavity seems to fill from upper right corner as well as bottom right corner.

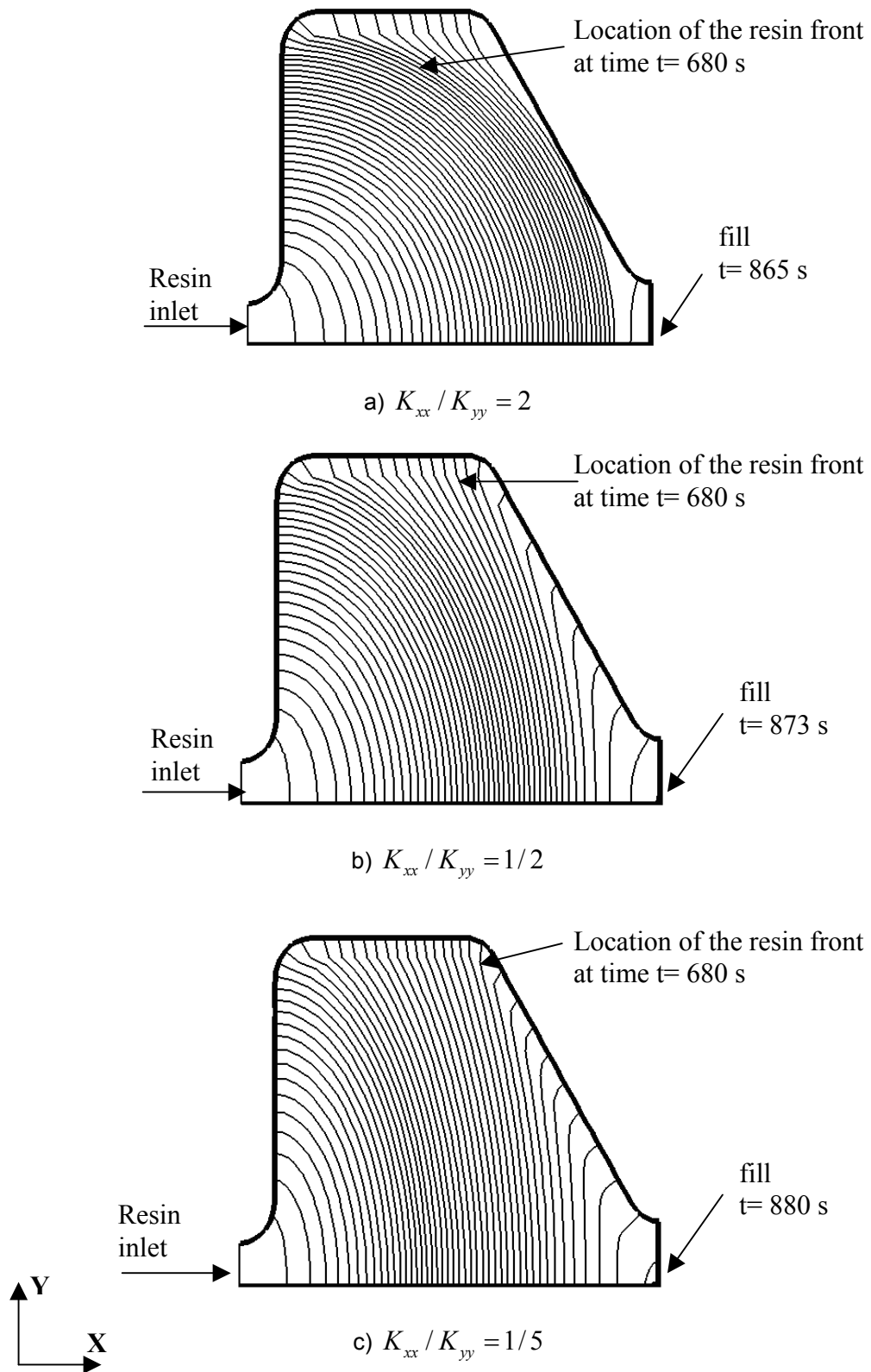


Figure 4.26 Flow front progressions for homogeneous and anisotropic permeability preforms at constant injection rates (flow fronts plotted every $\Delta t = 20$ s time increment)

Figure 4.27 presents the variation in inlet pressure at different levels of anisotropy. Although the pressure curves differ in magnitude, the relation to the level of anisotropy is not clear.

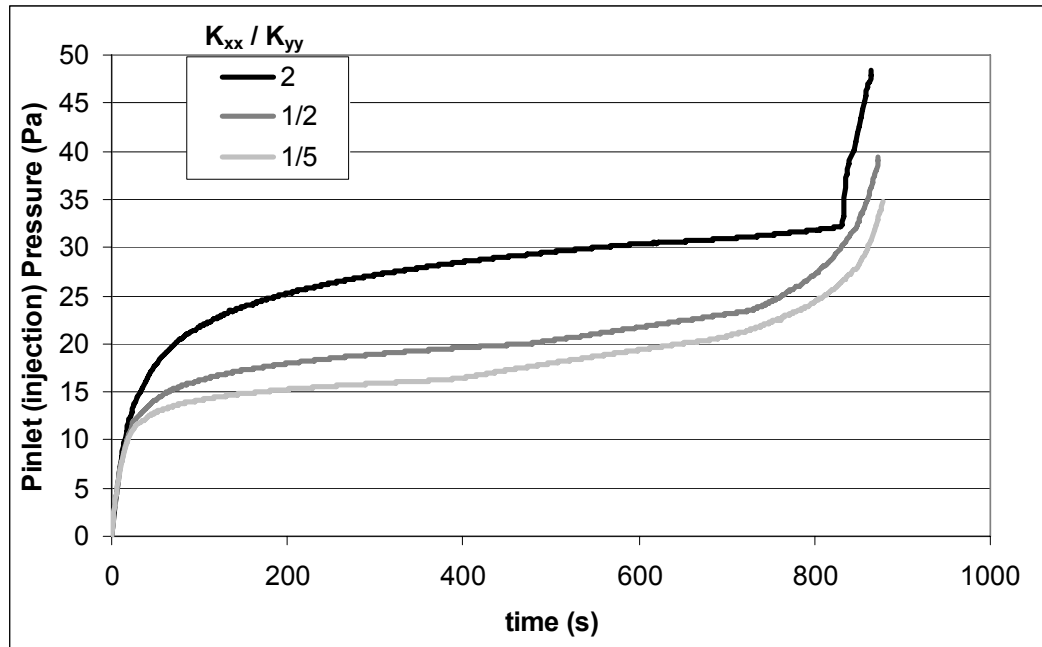


Figure 4.27 Inlet pressure variation for different levels of anisotropy for homogeneous performs at constant injection rates.

The pressure distributions at the instance of fill are presented in Figure 4.28. From the shape of the contours, the changing fill patterns are also evident. As K_{xx} / K_{yy} decreases, the increasing “verticalness” of the flow front is also observed in isobars.

4.2.5.3 Non-homogeneous and Anisotropic Preform Permeability

The last section in permeability analysis involves non-homogeneous ($K_{xx} = K_{xx}(x, y)$, $K_{yy} = K_{yy}(x, y)$) and anisotropic ($K_{xx} \neq K_{yy}$) preform permeability. The simulation configurations are presented in Table 4.12. For comparison, both isotropic and anisotropic results are presented. The non-homogeneous configurations are depicted in Figure 4.29. The material data for 1523 E-glass and 510-A40 are obtained from [26].

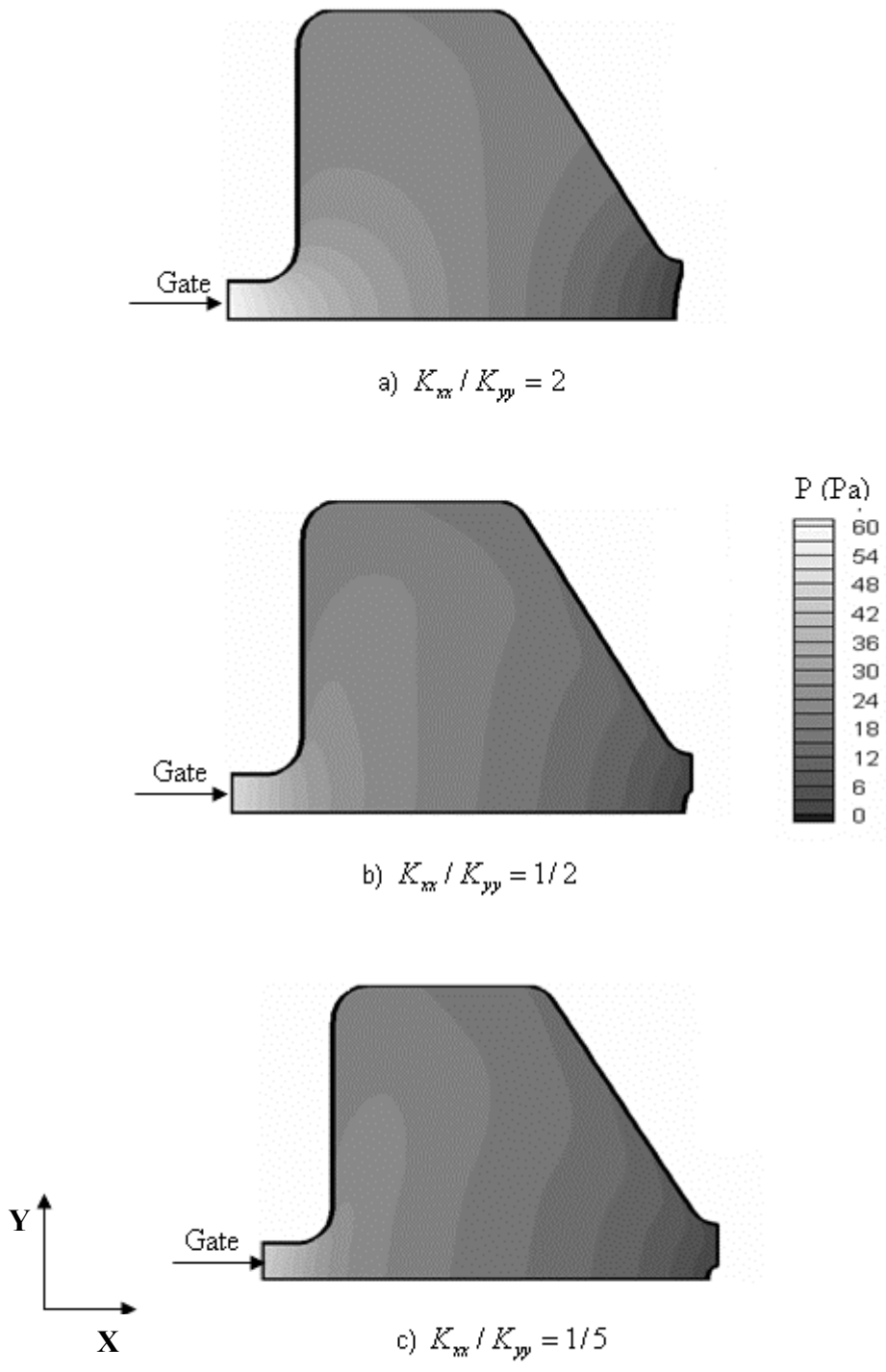


Figure 4.28 Pressure distribution at the instance of fill at various anisotropy levels for homogeneous preform.

Table 4.11 Process parameters for 2-D nonhomogenous and anisotropic preform permeability analysis

Case #	u_0 (mm/s)	Section Number	Permeability $K_{xx} \times 10^{-5} \text{ mm}^2$	Permeability $K_{yy} \times 10^{-5} \text{ mm}^2$	Numerical time increment Δt (s)	Fiber Volume Fraction v_f	Resin Viscosity (Pas) μ	Fill Time (s)
Case 1	0.2	1	2	2	0.2	0.5	0.5	1722
		2	4	4				
		3	6	6				
		4	8	8				
Case 2	0.2	1	2	2	0.2	0.5	0.5	1728
		2	2	4				
		3	2	6				
		4	2	8				
Case 3**	0.2	1	2	2	0.2	0.5	0.5	1740
		2	4	4				
		3	6	6				
		4	8	8				
Case 4**	0.2	1	2	2	0.2	0.5	0.5	1742
		2	2	4				
		3	2	6				
		4	2	8				

* Longitudinal nonhomogeneity

** Vertical nonhomogeneity

Figure 4.30, compares the shape and location of resin flow front at two time instances. A significant difference can be seen between Case 1 and 3 at both times. This is relatively straightforward since the nonhomogeneity of the domain is in horizontal direction in one (Case 1) and vertical in the other (Case 3). Both cases have the same nonhomogenous (but isotropic) permeability distribution but in different directions. The resulting flow front is more rounded for Case 1 and more vertical and narrow for Case 3. In Cases 2 and 4, there is the additional complexity of anisotropy. There is some difference between these cases as well as with Case 1 and 3, however it is difficult to pinpoint the reason.

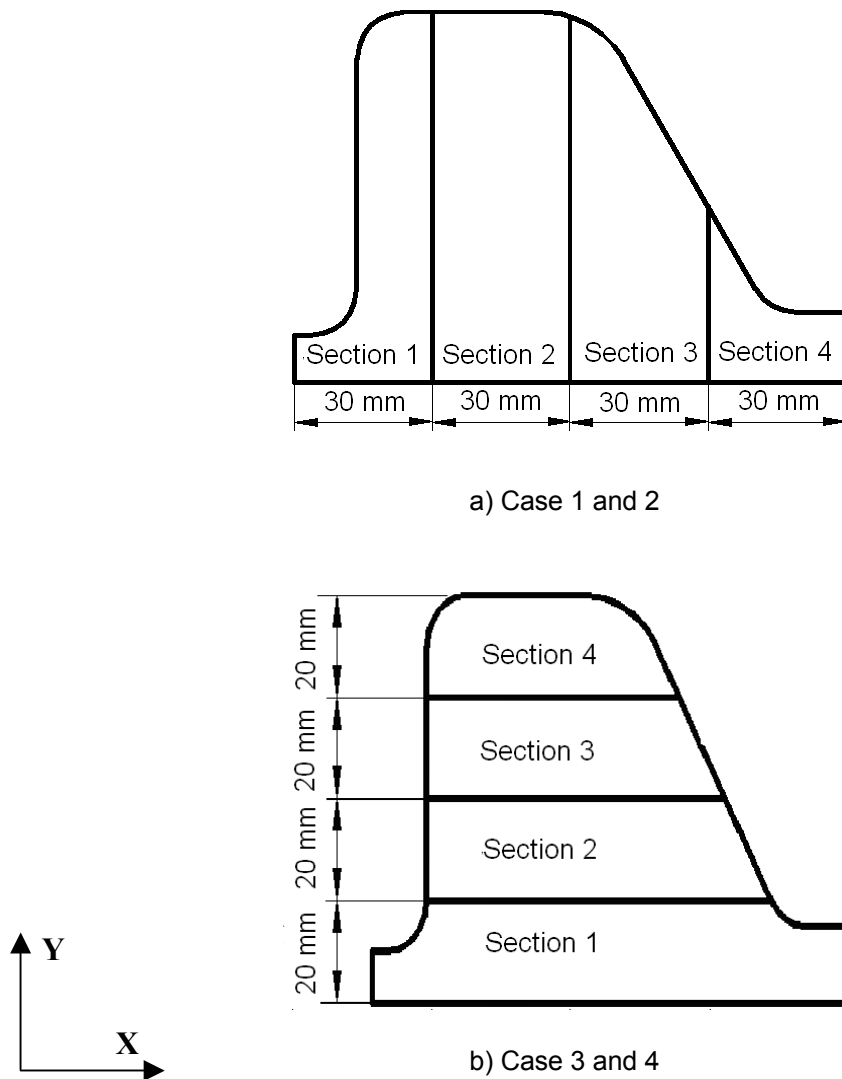


Figure 4.29 Non homogeneous preform configurations for anisotropic, non homogeneous preform permeability simulations.

Figure 4.31 presents flow front progressions for nonhomogeneous and anisotropic permeability preforms at constant injection rates. The most apparent difference is between Cases 1 and 3. Case 3 results in a more vertical front trend and the flow proceeds more slowly along the bottom mold wall. The difference is especially prominent on the right mold wall, as the resin fills towards the right corner. There are some differences in other cases as well due to different nonhomogeneity and anisotropy. It is not, at this stage, possible to conclude about the exact relations.

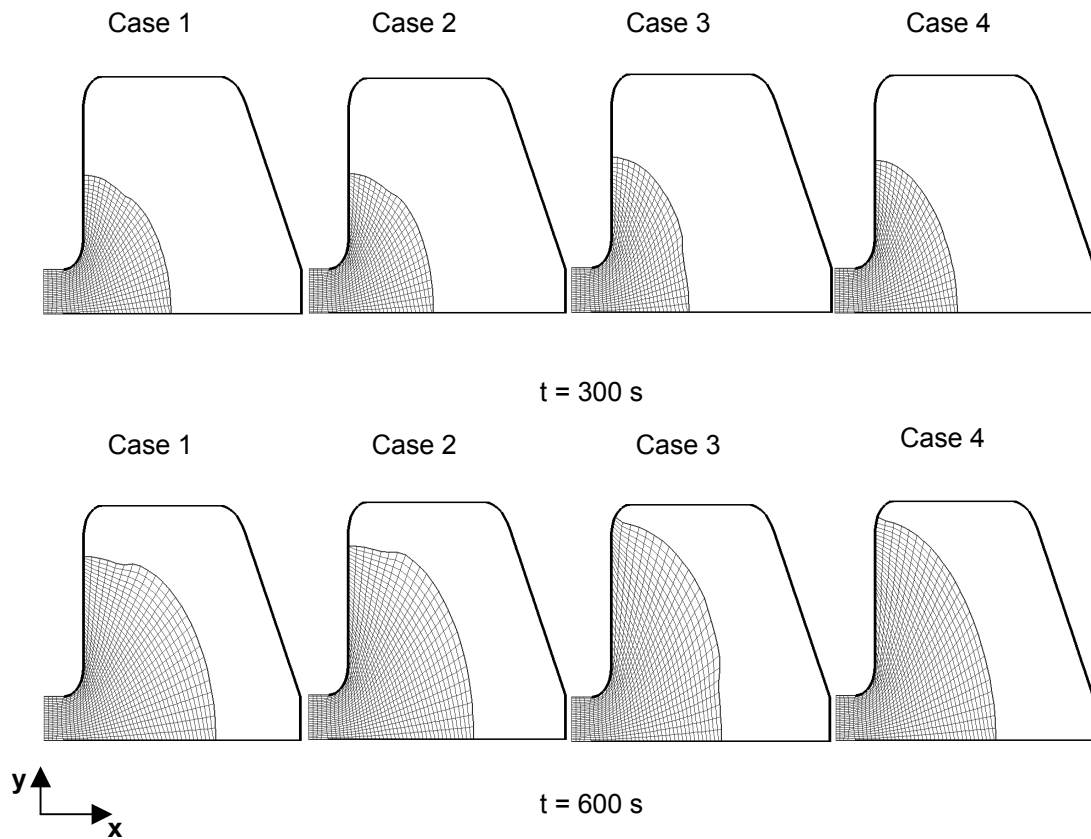
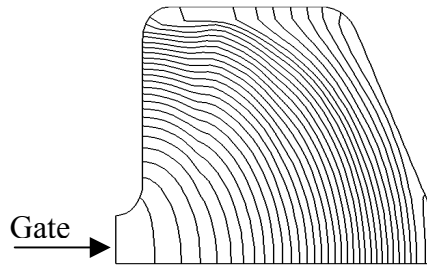


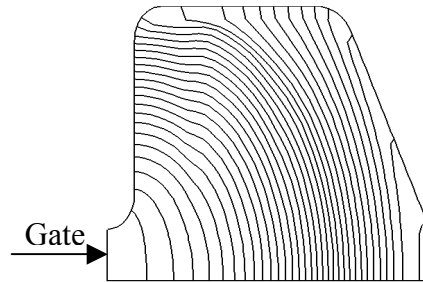
Figure 4.30 Comparison of the flow fronts at two time instances for nonhomogeneous isotropic-anisotropic preform permeability at constant injection rate.

Figure 4.32 presents the inlet pressure rise with time for different levels of nonhomogeneity and anisotropy. Case 3 and Case 4 appear to yield about the same pressure distribution therefore, in the presence of different nonhomogeneity configuration, anisotropy does not seem to have a significant effect. Case 1 stands apart from the rest of the cases with higher pressure. It is an isotropic case with vertical slabs of nonhomogeneity.

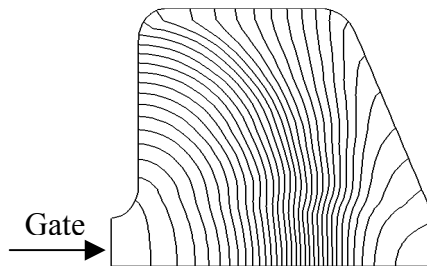
Figure 4.33 presents pressure distributions at the instance of fill. The pressure values vary considerably in value, especially between Cases 1 and 3. Although the average permeability values are close, the “horizontalness/verticalness” of the domain nonhomogeneity seems to be the dominant effect.



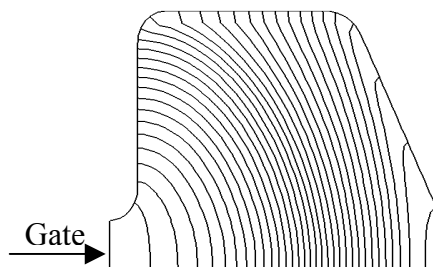
a) Case-1; Non-homogeneous and isotropic preform $K_{xx} = K_{yy}$; Fill time = 1722 s.



b) Case-2 ; Non-homogeneous and anisotropic preform $K_{xx} \neq K_{yy}$; Fill time = 1728 s.



c) Case-3; Non-homogeneous and isotropic preform $K_{xx} = K_{yy}$; Fill time = 1740 s.



d) Case-4 ; Non-homogeneous and anisotropic preform $K_{xx} \neq K_{yy}$; Fill time = 1742 s.

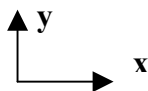


Figure 4.31 Flow front progressions for non-homogeneous isotropic-anisotropic permeability cases. (Flow fronts plotted every $\Delta t = 40$ s time increment)

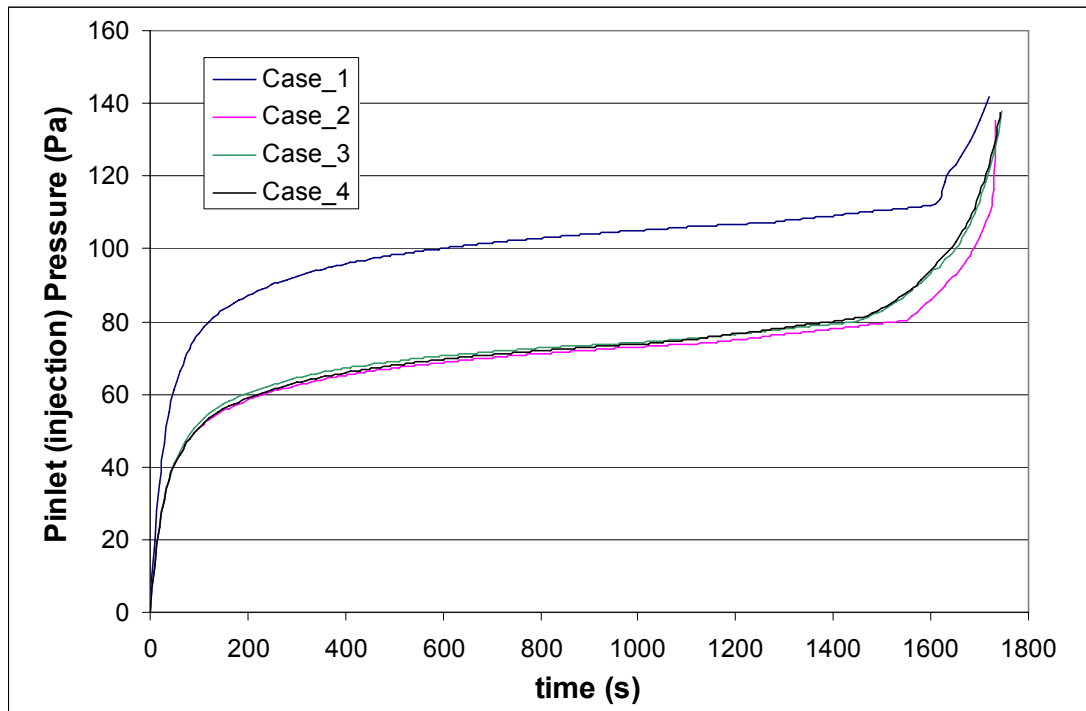
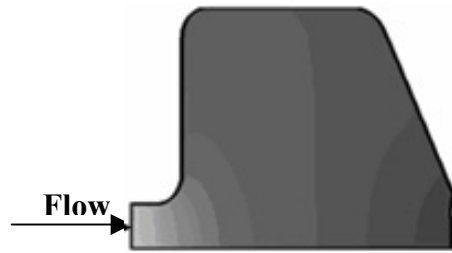


Figure 4.32 Inlet pressure variation for different levels of anisotropy for nonhomogeneous preforms at constant injection rates.

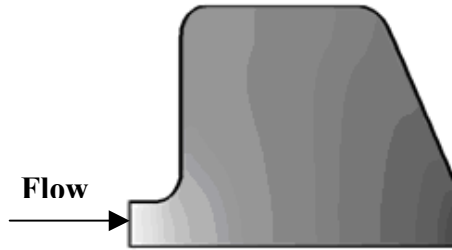
The maximum pressure values in Cases 2, 3 and 4 are comparable. The major difference lies in how the pressure is distributed. In Case 3 there is little pressure variation within the majority of mold. The variations are concentrated near inlet and fill. In Case 4, there is a more even pressure variation throughout the mold. As before, Case 1 has the largest pressure in the mold.

4.3 Double Gate RTM Analysis

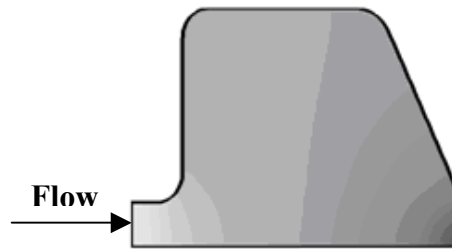
As part of the current thesis work, double gate injection simulation capability has been developed and added to the current program. The simulation data are presented in Table 4.12. The presented properties for resin and fiber



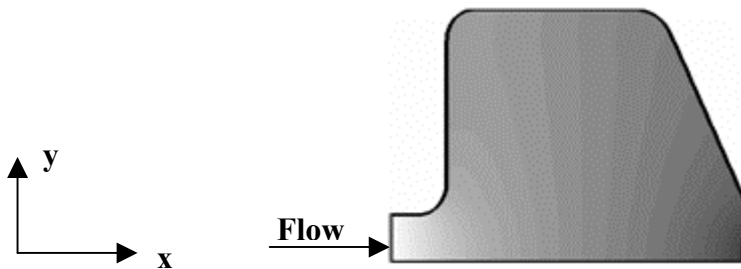
a) Case-2; Non-homogeneous and isotropic preform $K_{xx} = K_{yy}$; Fill time = 1722s.



b) Case-2; Non-homogeneous and anisotropic preform $K_{xx} \neq K_{yy}$; Fill time = 1728 s.



c) Case-3; Non-homogeneous and isotropic preform $K_{xx} = K_{yy}$; Fill time = 1740 s.



d) Case-4; Non-homogeneous and anisotropic preform $K_{xx} \neq K_{yy}$; Fill time = 1742 s.

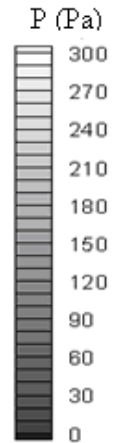


Figure 4.33 Pressure distributions at the instance of fill at various nonhomogeneous levels for isotropic/anisotropic preform.

preform correspond to epoxy vinyl ester resin and 1523 E-glass fiber [26]. The preform is isotropic; the permeabilities in x and y directions are the same. The preform is also homogeneous, having the same fiber volume fraction and permeability, everywhere. The cross-sectional areas of the two gates differ slightly. The width of gate 1 is 10 mm, whereas for gate 2, it is 15

mm. For the same injection velocities, mass flow rate from gate 2 is slightly larger than that from gate 1.

Table 4.12 Process parameters for double gate resin injection (same injection rates at both gates).

Gate # 1 u_0 (mm/s)	Gate # 2 u_0 (mm/s)	Permeability $K_{xx} \times 10^{-5} \text{ mm}^2$	Permeability $K_{yy} \times 10^{-5} \text{ mm}^2$	Numerical time increment Δt (s)	Fiber Volume Fraction v_f	Resin Viscosity (Pas) μ	Fill Time (s)
1	1	4.8	4.8	0.1	0.5	0.45	192

Figure 4.34, presents the location of the flow fronts at various time levels before and during merging of the flow fronts.

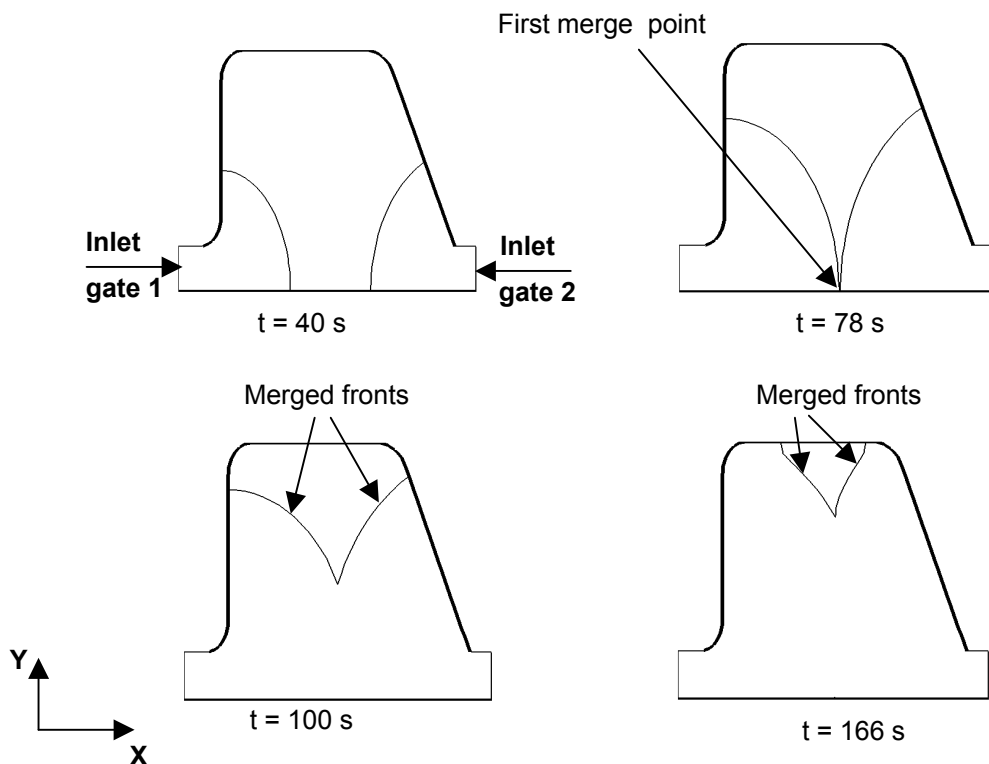


Figure 4.34 Location of resin flow fronts at various time levels for double gate resin injection (same injection rates at both gates)

The solution of the merged flow domain was explained previously in Chapter 3. Once the flow fronts merge, the process parameters in both flow domain become related and are not calculated independently.

Figure 4.35 presents the flow front progression of the double gate injection process until fill, depicting the location of the flow fronts at every 20 seconds. Once the flow fronts begin merging, (after about 78 s) the incoming resin from both gates forces the two fronts to move closer to one another, but, at the same time, towards the top mold wall. Thus, the slope of the combined fronts does not flatten out at once.

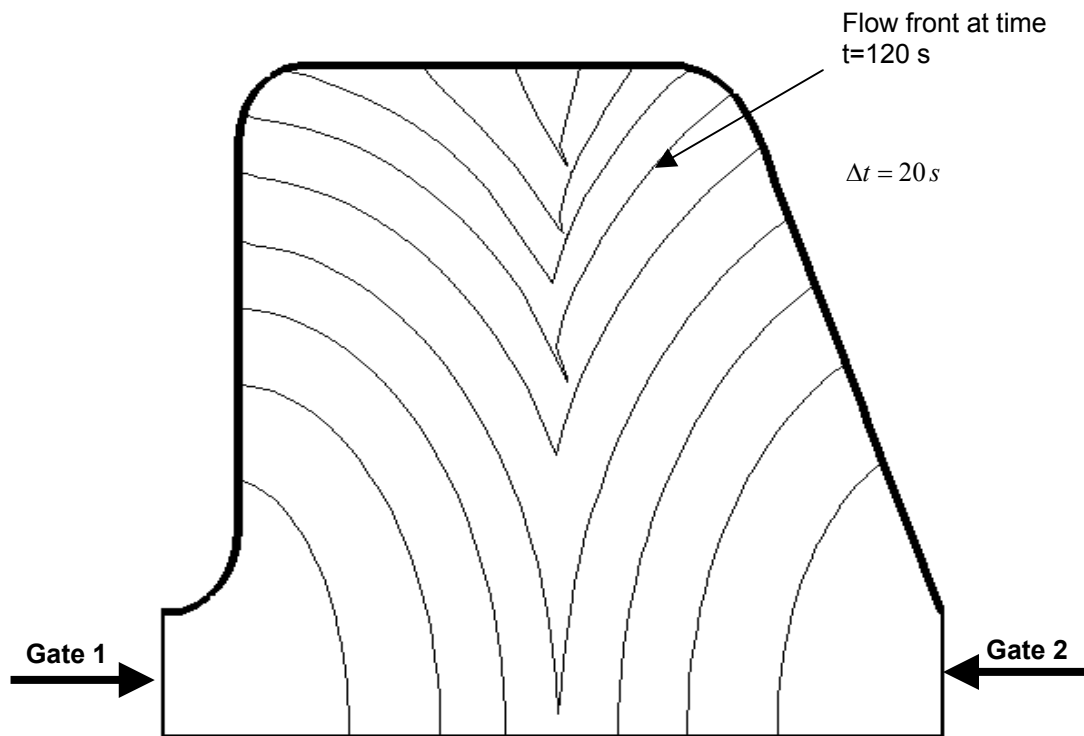


Figure 4.35 Flow front progressions for double gate resin injection.

Figure 4.36 depicts the "weld line" formed by the merging flow fronts. Weld line is formed by the locus of points at which the fronts have met. Weld line is a term originally used in injection molding to depict the "weak" spots in a molded product (due to weaker adhesion of molten plastic). The line is not a straight vertical line, but is skewed due to the unsymmetrical geometry of the mold cavity.

Figure 4.37 presents the variation in inlet pressure at gates 1 and 2. For comparison, the inlet pressure change for single gate injection (gate 1) under the same circumstances is also given.

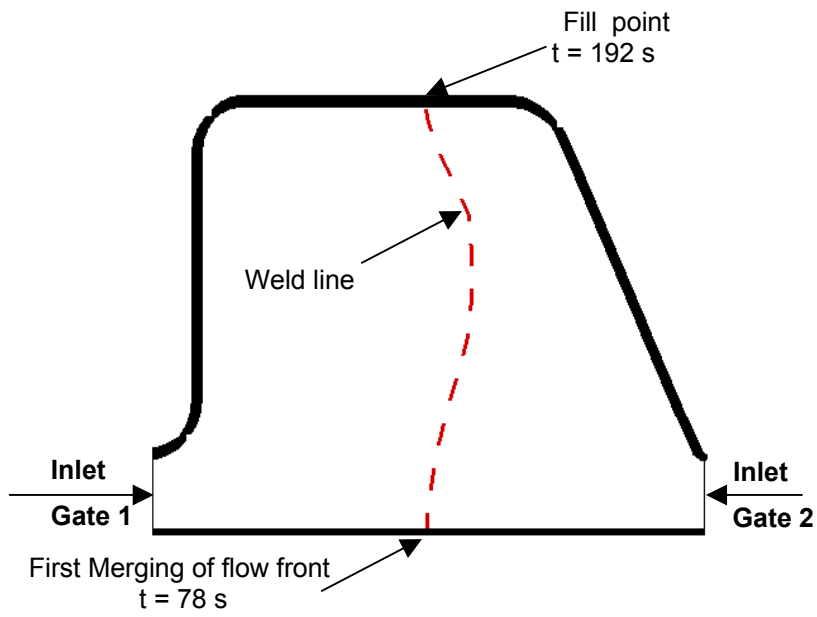


Figure 4.36 "Weld" line formed by merging of the two flow fronts (at the same resin injection rate)

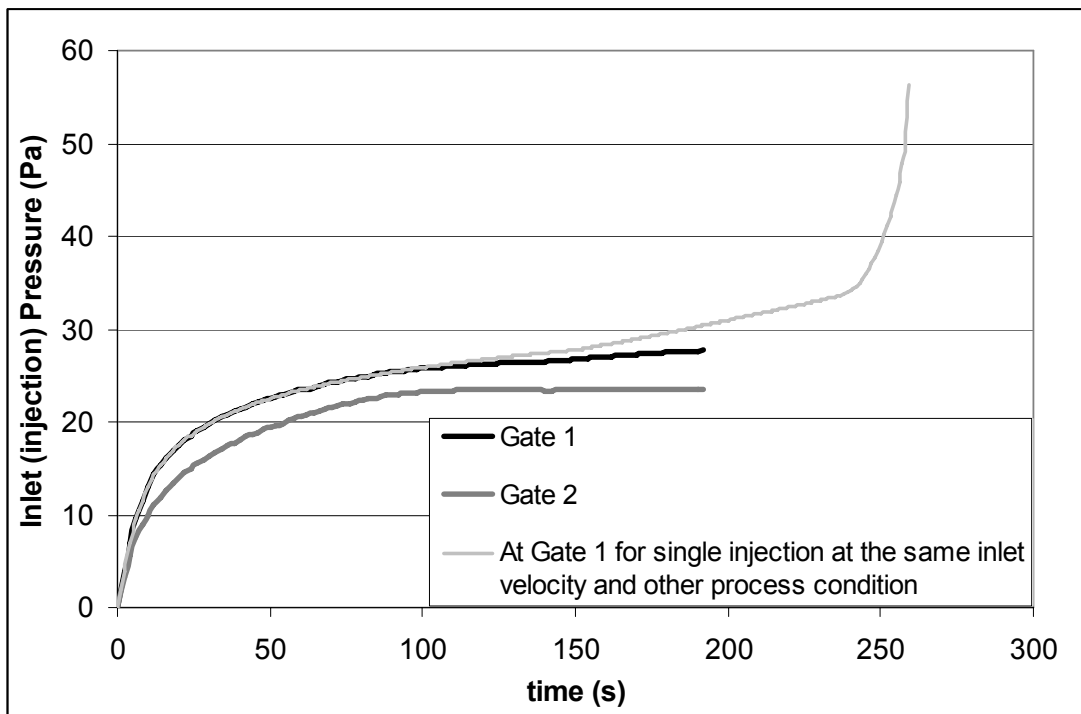


Figure 4.37 Comparisons of inlet pressure at gates 1 and 2 for double gate resin injection and single gate (gate 1) injection

The pressure differences between Gate 1 and Gate 2 are caused by the inlet gate geometries. The flow in Gate 1 is somewhat more restrictive than the flow in the Gate 2. As a result, the pressure on Gate 1 is higher than that in Gate 2. After merging, the pressure does not increase too much up to fill, for the two gates. The trends are similar to the single gate injection except the final sharp pressure increase in the single gate injection.

Figure 4.38 presents the pressure distribution at various time instances of double gate resin injection. As the resin fills towards the top mold wall, the pressure profiles lose their rounded shape and follow the merge path.

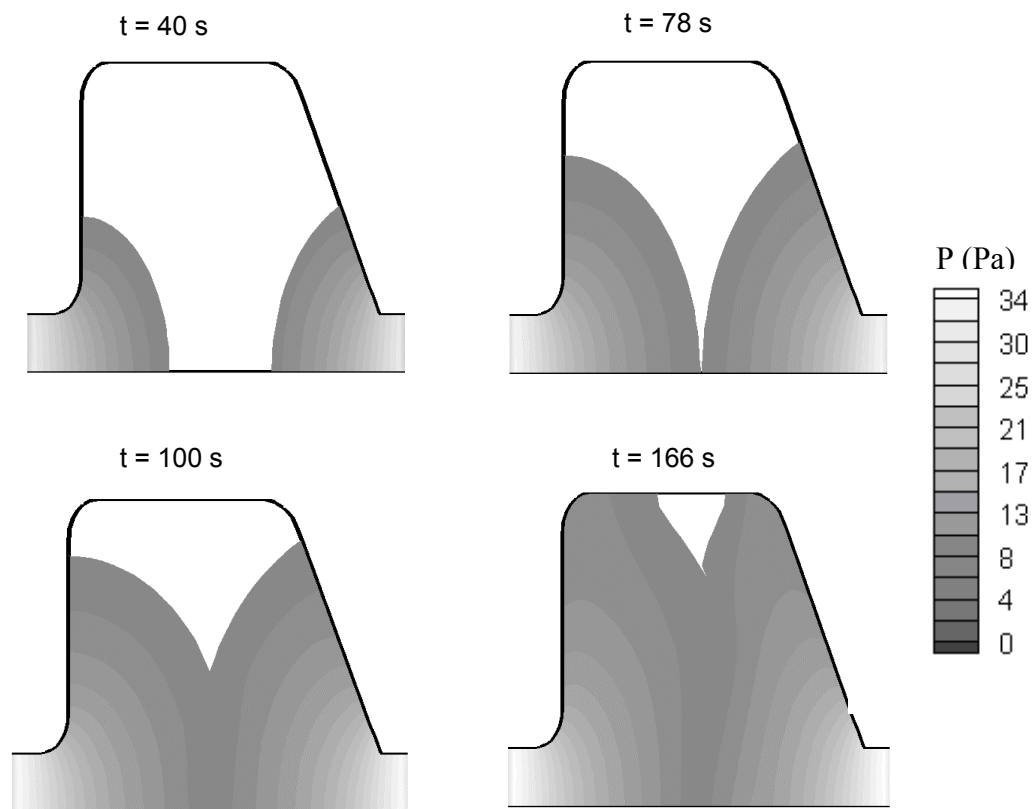


Figure 4.38 Pressure distribution at various time instances of double gate resin injection.

Finally, a double gate injection simulation with different injection velocities at the gates is performed. Table 4.13 presents the simulation data. All the data are the same except resin injection velocities. The velocity of the resin at gate 2 is cut half. As expected, fill time increase proportionally.

Table 4.13 The simulation data for 2-D homogeneous and isotropic double gate run

Gate # 1 u_0 (mm/s)	Gate # 2 u_0 (mm/s)	Permeability $K_{xx} \times 10^{-5} \text{ mm}^2$	Permeability $K_{yy} \times 10^{-5} \text{ mm}^2$	Numerical time increment Δt (s)	Fiber Volume Fraction v_f	Resin Viscosity (Pa.s) μ	Fill Time (s)
1	0.5	4.8	4.8	0.1	0.5	0.45	246

Figure 4.39 presents the location of resin flow fronts recorded every 20 seconds. Compared with Figure 4.33, the first merge point is closer to gate 2, since the injection rate from gate 2 is halved. Furthermore, the fill pattern has also changed as the fill point has shifted to the right, as expected.

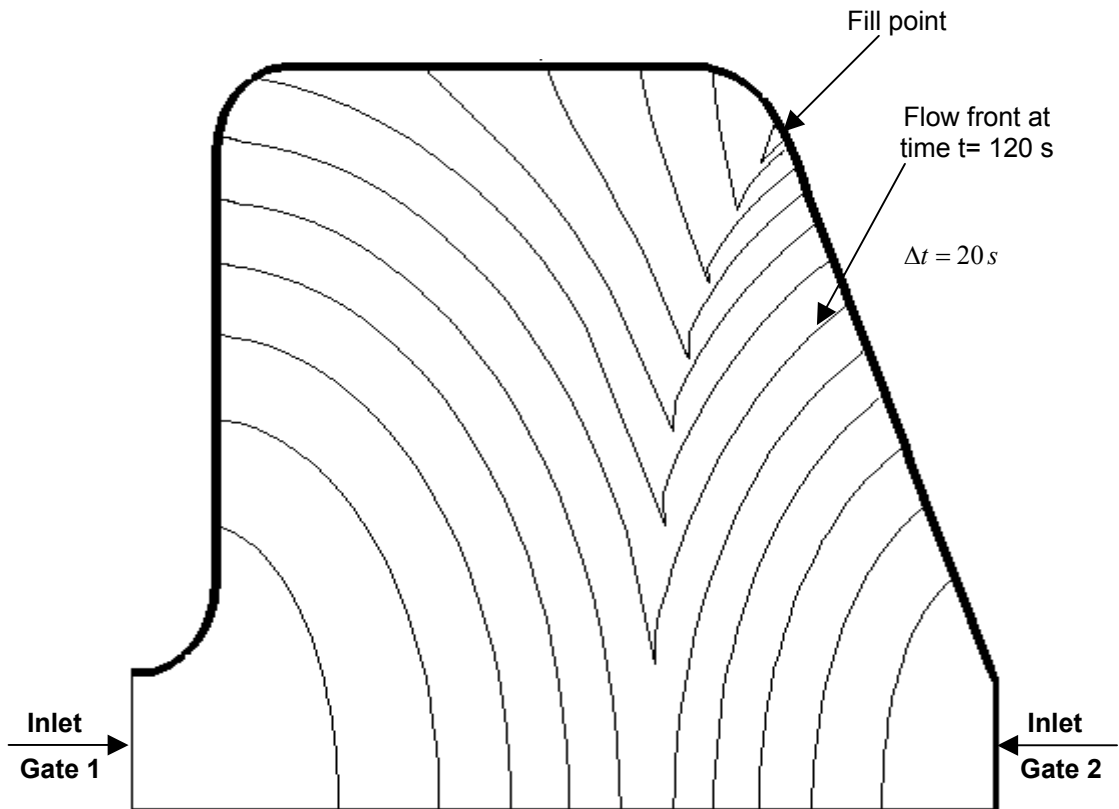


Figure 4.39 Flow front progressions for double gate resin injection rates (different injection rates at the gates)

The flow fronts begin merging after 112 seconds as opposed 78 second in the previous configuration. This is expected as the velocity is decreased (on Gate 2) and the effect is also observed in a larger fill time, 246 s.

CHAPTER 5

CONCLUSIONS AND FUTURE WORK

This study used and updated a custom computer program, written in FORTRAN, to simulate various RTM scenarios. In the program, resin impregnation was formulated assuming two dimensional, quasi-steady, isothermal flow of a viscous fluid through a porous medium. The preform was assumed to be orthotropic; however, the principal permeability axes were made to coincide with the Cartesian coordinate system during formulations, somewhat simplifying the mathematics in the model. The governing equation formulation and boundary conditions were derived, the numerical discretization involving domain transformation and finite difference method, and the solution methodology were presented. The double gate injection capability was implemented and the related solution sequence was also presented. Lastly, various RTM simulation scenarios involving 1-D and 2-D impregnations, parametric studies, non-homogeneous preforms and resin injection from two gates (the last two being capabilities implemented as part of the current thesis study) were presented and discussed.

To check the numerical calculation accuracies, 1-D resin impregnation modeling results were compared with analytic solutions for the same problem. The analytical and numerical results matched almost identically, in terms of mold fill time and inlet pressure increase with time. An experimental impregnation analysis was taken from the literature and compared with modeling results for the same RTM configuration. Specifically, an impregnation experiment and the corresponding numerical solution for 2-D resin impregnation through irregular planar mold geometry from a single gate were compared. Even though the fill times were close in the two cases, the progression of the flow fronts was somewhat different, especially for the first half of injection. The model flow fronts, recorded at the same time instances as the experiment, lagged behind the experiment, especially at the upper

mold wall where a contracting (concave) wall curvature existed. On the lower mold wall where a diverging (convex) wall curvature existed, the experiment and the model contact points matched their positions almost identically. In the second half of the fill, the model flow fronts caught up with the experiment and the time that it took to fill the entire mold cavity were, eventually, close. In this analysis, the appropriation of the experimental data was somewhat problematic as there was some uncertainty about the dimensions of the actual mold that was used in the experiment. Therefore, the slight mismatch between the experiment and model flow front progressions can be partly due to the uncertainty of geometric data.

With the double gate injection simulation capability added to the program, the flow front progression, inlet pressure rise and flow domain pressure variations could be predicted for the 2-D impregnation in an irregular planar geometry from two gates, both at the same flow rate or at different flow rates. However, a verification study for the accuracy of double-gate injection predictions has not been undertaken yet.

The capability to simulate resin impregnation through non-homogenous preforms, which is added to the computer program as part of this thesis, enables the analysis of process configurations in which different types of preforms, different fiber loadings (fiber volume fractions) and (to a degree) different mold cavity thicknesses exist.

Since there was some uncertainty in the geometric mold data of the experimental results that were compared with the single gate injection simulation results, in the future, the model results can further be compared with other experimental results in the literature and/or the results obtained from a commercial computer program. In addition, for better simulation accuracy, the computer program can further be updated to relate the permeability of the preform to changing fiber volume fractions, using various models from literature.

As part of the future work, the verification studies for the accuracy of double-gate injection predictions can also be performed. The results of the current double-gate impregnation model can be compared with a related experiment and/or commercial computer program results for the same configuration. The model can also be implemented for different gate locations in a specific mold, to analyze the resulting process.

REFERENCES

- [1] John P. Coulter , Resin impregnation during the manufacturing of composite materials, Ph.D. dissertation, Department of Mechanical Engineering, University of Delaware, Newark, Delaware 19716, USA, 1998.
- [2] Islnotes.cse.msu.edu, Resin Transfer Molding, Material Selection, <http://islnotes.cse.msu.edu/trp/liquid/rtm/index.html> , last visited on May 2005.
- [3] Typical Applications for Hexcel Products in Aero-Engines, <http://www.hexcel.com/Markets/Aerospace/>, Typical Applications for Hexcel Products in Aero-Engines, last visited on May 2005.
- [4] Me.gatech.edu, Liquid Resin Molding ver 1, <http://www.me.gatech.edu/jonathan.colton/me4793/rtm.pdf>, last visited on May 2005.
- [5] Esi Group The virtual Try-out Space Company, Features & Specifications PAM-RTM 2004, <http://www.esi-group.com>, last visited on June 2005.
- [6] Islnotes.cse.msu.edu, Introduction to Resin Transfer Molding, <http://islnotes.cse.msu.edu/trp/liquid/rtm/index.html> , last visited on May 2005.
- [7] Network group for composites in construction, Engineering Properties of Fibre Reinforced Composites, <http://www.ngcc.org.uk/info/ch4.html>, last visited on June 2005.
- [8] Matthew Chatterton, Darryl Knight, Paula McInenly and Kitty Tsang, Advanced Polymer Structure, Properties and Processing, Department of

Chemical Engineering, Queen's University, Kingston, Ontario, 28 March 2002.

- [9] Prof. Joe Greene, Reinforcements, http://www.csuchico.edu/~jpgreene/m247/m247_ch03/m247_ch03.ppt, last visited on 28 March 2002.
- [10] Composite worlds, Resin transfer molding processes, <http://www.compositesworld.com/sb/ov-rtm>, last visited on 28 March 2002.
- [11] Christophe Birdtruy, Bruno Hilaireb & Jo& Pabiot, The Interactions Between Flows Occurring Inside And Outside Fabric Tows During Rtm, *Composites Science and Technology* 57 (1997) 587-596, 1997 Elsevier Science.
- [12] H. Darcy. *Les fontaines publiques de la ville de Dijon*. Dalmont, Paris, 1856.
- [13] John P. Coulter & Selçuk İ. Güçeri, Resin impregnation during composites manufacturing theory and experimentation, 6 December 1998.
- [14] H. Aoyagi. Filling process simulation in the mold for the RTM and SRIM. Center for Composite Materials Report CCM 92-96, University of Delaware, Newark, Delaware 19716, USA, 1998.
- [15] H. Aoyagi, M. Uenoyama, and S.İ. Güçeri. Analysis and simulation of structural reaction injection molding (SRIM). *International Polymer Processing*, 7(1) : 71-83, 1992.
- [16] M.V. Brusckhe and S.G. Advani. A finite element /control volume approach to mold filling in anisotropic porous media. *Polymer Composites*, 11(6) : 398-405, 1990.

- [17] C.A. Fracchia and C.L. Tucker . Simulation of resin transfer mold filling. In Proc. PPS; Sixth Annual Meeting. Polymer Processing Society, 1990.
- [18] A.W. Chan and S.T.Hwang. Modelling resin transfer molding of axisymmetric composite parts. Journal of Material Processing and Manufacturing Science, 1(1) : 105-118,1992.
- [19] Chan AW, Morgan RJ. Sequential multiple port injection for resin transfer molding of polymer composites. SAMPE Quarterly 1992; October: 45–9.
- [20] Charles L. Tucker III, Computer modelling for polymer processing fundamentals,1989.
- [21] Burkhard Friedrichs, Modeling of three dimensional flow fields in injection and resin transfer molding processes .Ph.D. dissertation, Department of Mechanical Engineering, University of Delaware, Newark, Delaware 19716, USA, 1992.
- [22] Yeong-Eun Yoo and Woo IL Lee*, Numerical simulation of the Resin transfer mold filling process using the boundary element method.
- [23] Moon Koo Kang, Jae Joon Jung, Woo Il Lee* ; Analysis of resin transfer moulding process with controlled multiple gates resin injection,24 September 1999 .
- [24] Y.C. Lam, Sunil C. Joshi, X.L. Liu; Numerical simulation of the mould-filling process in resin-transfer moulding, 18 November 1999.
- [25] Zhong Cai, Analysis of mold filling in RTM processes, August 15 1991.

[26] Jay Randall Sayre, "Vacuum-Assisted Resin Transfer Molding (VARTM) Model Development, Verification, and Process Analysis, Dissertation submitted to the Faculty of the Virginia Polytechnic Institute and State University In partial fulfillment of the requirements for the degree of Doctor of Philosophy in Materials Engineering Science , April 11, 2000 Blacksburg, Virginia.

[27] Pachepsky, Yakov 1; Rawls, Walter 1; Timlin, Dennis 2, A one-parameter relationship between unsaturated hydraulic conductivity and water retention.

Soil Science. 165(12):911-919, December 2000.

APPENDIX A

INTERCHANGING THE DEPENDENT AND INDEPENDENT VARIABLES IN GRID GENERATION EQUATIONS

The equations for 2D numerical grid generation are manipulated in order to interchange the dependent and the independent variables [10]. The resulting partial differential equations, when solved, yields $x(\xi, \eta)$ and $y(\xi, \eta)$.

The grid generation equations are:

$$\xi_{xx} + \xi_{yy} = \frac{\partial^2 \xi}{\partial x^2} + \frac{\partial^2 \xi}{\partial y^2} = P(x, y) \quad (\text{A.1})$$

$$\eta_{xx} + \eta_{yy} = \frac{\partial^2 \eta}{\partial x^2} + \frac{\partial^2 \eta}{\partial y^2} = P(x, y) \quad (\text{A.2})$$

Using the chain rule:

$$\frac{\partial \xi}{\partial \xi} = 1 = \xi_x x_\xi + \xi_y y_\xi \quad (\text{A.3})$$

$$\frac{\partial \xi}{\partial \eta} = 0 = \xi_x x_\eta + \xi_y y_\eta \quad (\text{A.4})$$

Solving these equations simultaneously for ξ_x and ξ_y yields:

$$\xi_x = \frac{y_\eta}{J} \quad (\text{A.5})$$

$$\xi_y = \frac{x_\eta}{J} \quad (\text{A.6})$$

J is the Jacobian of transformation, defined as

$$J = x_\xi y_\eta - y_\xi x_\eta \quad (\text{A.7})$$

Similarly, η_x and η_y are found as

$$\eta_x = \frac{y_\xi}{J} \quad (\text{A.8})$$

$$\eta_y = \frac{x_\xi}{J} \quad (\text{A.9})$$

Using the chain rule:

$$\frac{\partial}{\partial x} = \frac{\partial}{\partial \eta} \frac{\partial \eta}{\partial x} + \frac{\partial}{\partial \xi} \frac{\partial \xi}{\partial x} = \eta_x \frac{\partial}{\partial \eta} + \xi_x \frac{\partial}{\partial \xi} \quad (\text{A.10})$$

$$\frac{\partial}{\partial y} = \frac{\partial}{\partial \eta} \frac{\partial \eta}{\partial y} + \frac{\partial}{\partial \xi} \frac{\partial \xi}{\partial y} = \eta_y \frac{\partial}{\partial \eta} + \xi_y \frac{\partial}{\partial \xi} \quad (\text{A.11})$$

Equations (A.3) to (A.11) are placed into (A.1) as:

$$\eta_x \frac{\partial}{\partial \eta} \xi_x + \xi_x \frac{\partial}{\partial \xi} \xi_x + \eta_y \frac{\partial}{\partial \eta} \xi_y + \xi_y \frac{\partial}{\partial \xi} \xi_y = P(\xi, \eta) \quad (\text{A.12})$$

$$\eta_x \frac{\partial}{\partial \eta} \frac{y_\eta}{J} + \xi_x \frac{\partial}{\partial \xi} \frac{y_\eta}{J} - \eta_y \frac{\partial}{\partial \eta} \frac{x_\eta}{J} + \xi_y \frac{\partial}{\partial \xi} \frac{x_\eta}{J} = P(\xi, \eta) \quad (\text{A.13})$$

$$-\frac{\partial}{\partial \eta} \frac{y_\xi}{J} \frac{y_\eta}{J} + \frac{\partial}{\partial \xi} \frac{y_\eta}{J} \frac{y_\eta}{J} - \frac{\partial}{\partial \eta} \frac{x_\xi}{J} \frac{x_\eta}{J} - \frac{\partial}{\partial \xi} \frac{x_\eta}{J} \frac{x_\eta}{J} = P(\xi, \eta) \quad (\text{A.14})$$

$$J \left(\frac{\partial}{\partial \eta} y_\xi y_\eta + \frac{\partial}{\partial \xi} y_\eta^2 - \frac{\partial}{\partial \eta} x_\xi x_\eta - \frac{\partial}{\partial \xi} x_\eta^2 \right) = J^3 P(\xi, \eta) \quad (\text{A.15})$$

Likewise, equation (A.2) takes the form:

$$\xi_x \frac{\partial}{\partial \xi} \eta_x + \eta_x \frac{\partial}{\partial \eta} \eta_x + \xi_y \frac{\partial}{\partial \xi} \eta_y + \eta_y \frac{\partial}{\partial \eta} \xi_y = P(\xi, \eta) \quad (\text{A.16})$$

$$\eta_x \frac{\partial}{\partial \xi} \frac{y_\xi}{J} + \eta_x \frac{\partial}{\partial \eta} \frac{y_\xi}{J} - \xi_y \frac{\partial}{\partial \xi} \frac{x_\xi}{J} + \eta_y \frac{\partial}{\partial \eta} \frac{x_\xi}{J} = P(\xi, \eta) \quad (\text{A.17})$$

$$-\frac{\partial}{\partial \eta} \frac{y_\eta}{J} \frac{y_\xi}{J} + \frac{\partial}{\partial \eta} \frac{y_\xi}{J} \frac{y_\xi}{J} - \frac{\partial}{\partial \xi} \frac{x_\eta}{J} \frac{x_\xi}{J} - \frac{\partial}{\partial \mu} \frac{x_\xi}{J} \frac{x_\xi}{J} = P(\xi, \eta) \quad (\text{A.18})$$

$$J \left(\frac{\partial}{\partial \xi} y_\eta y_\xi + \frac{\partial}{\partial \eta} y_\xi^2 - \frac{\partial}{\partial \xi} x_\eta x_\xi - \frac{\partial}{\partial \eta} x_\xi^2 \right) = J^3 P(\xi, \eta) \quad (\text{A.19})$$

After various manipulations,

$$\begin{aligned}
& x_\eta \left[(x_\eta^2 + y_\eta^2) y_{\xi\xi} - 2(x_\xi x_\eta + y_\xi y_\eta) y_{\xi\eta} + (x_\xi^2 + y_\xi^2) y_{\eta\eta} \right] \\
& - y_\eta \left[(x_\eta^2 + y_\eta^2) x_{\xi\xi} - 2(x_\xi x_\eta + y_\xi y_\eta) x_{\xi\eta} + (x_\xi^2 + y_\xi^2) x_{\eta\eta} \right] \\
& = J^3 P(\xi, \eta)
\end{aligned} \tag{A.20}$$

$$\begin{aligned}
& y_\xi \left[(x_\eta^2 + y_\eta^2) y_{\xi\xi} - 2(x_\xi x_\eta + y_\xi y_\eta) y_{\xi\eta} + (x_\xi^2 + y_\xi^2) y_{\eta\eta} \right] \\
& - x_\xi \left[(x_\eta^2 + y_\eta^2) y_{\xi\xi} - 2(x_\xi x_\eta + y_\xi y_\eta) y_{\xi\eta} + (x_\xi^2 + y_\xi^2) y_{\eta\eta} \right] \\
& = J^3 Q(\xi, \eta)
\end{aligned} \tag{A.21}$$

Defining geometric coefficients α, β and γ as

$$\alpha = x_\eta^2 + y_\eta^2 \quad \beta = x_\xi x_\eta + y_\xi y_\eta \quad \gamma = x_\xi^2 + y_\xi^2 \tag{A.22}$$

Multiplying equation (A.20) with x_ξ and equation (A.21) with x_η yields:

$$x_\xi x_\eta \left[\alpha y_{\xi\xi} - 2\beta y_{\xi\eta} + \gamma y_{\eta\eta} \right] - x_\xi y_\eta \left[\alpha x_{\xi\xi} - 2\beta x_{\xi\eta} + \gamma x_{\eta\eta} \right] = J^3 P x_\xi \tag{A.23}$$

$$y_\xi x_\eta \left[\alpha y_{\xi\xi} - 2\beta y_{\xi\eta} + \gamma y_{\eta\eta} \right] - x_\xi x_\eta \left[\alpha y_{\xi\xi} - 2\beta y_{\xi\eta} + \gamma y_{\eta\eta} \right] = J^3 Q x_\eta \tag{A.24}$$

Adding equations (A.23) and (A.24) and manipulating the equation yields:

$$\alpha x_{\xi\xi} - 2\beta x_{\xi\eta} + \gamma x_{\eta\eta} + J^2 (P x_\xi + Q x_\eta) = 0 \tag{A.25}$$

Similarly, multiplying equation (A.20) with y_ξ and equation (A.21) with y_η , adding the resulting equations and manipulating the sum equation yields

$$\alpha y_{\xi\xi} - 2\beta y_{\xi\eta} + \gamma y_{\eta\eta} + J^2 (P y_\xi + Q y_\eta) = 0 \tag{A.26}$$

APPENDIX B

FINITE DIFFERENCE EXPRESSIONS

For an M x N grid system in computational domain (ζ, η) for unit grid length, $\Delta\xi=1$ and $\Delta\eta=1$.

First Derivatives:

i=1 (forward difference)

$$\left. \frac{\partial \phi}{\partial \xi} \right|_{1,j} = \frac{1}{2}(-3\phi_{1,j} + 5\phi_{2,j} - \phi_{3,j}) + O[(\Delta\xi)^2] \quad (\text{B.1})$$

1 < i < M (central difference)

$$\left. \frac{\partial \phi}{\partial \xi} \right|_{i,j} = \frac{1}{2}(\phi_{i+1,j} - \phi_{i-1,j}) + O[(\Delta\xi)^2] \quad (\text{B.2})$$

i= M (backward difference)

$$\left. \frac{\partial \phi}{\partial \xi} \right|_{M,j} = \frac{1}{2}(3\phi_{M,j} - 4\phi_{M-1,j} - \phi_{M-2,j}) \quad (\text{B.3})$$

j= 1 (forward difference)

$$\left. \frac{\partial \phi}{\partial \eta} \right|_{i,1} = \frac{1}{2}(-3\phi_{i,1} + 4\phi_{i,2} - \phi_{i,3}) + O[(\Delta\eta)^2] \quad (\text{B.4})$$

1 < j < N (central difference)

$$\left. \frac{\partial \phi}{\partial \eta} \right|_{i,j} = \frac{1}{2}(\phi_{i,j+1} - \phi_{i,j-1}) + O(\Delta\eta^2) \quad (\text{B.5})$$

j= N (backward difference)

$$\left. \frac{\partial \phi}{\partial \eta} \right|_{i,N} = \frac{1}{2}(3\phi_{i,N} - 4\phi_{i,N-1} + \phi_{i,N-2}) + O(\Delta\eta^2) \quad (\text{B.6})$$

Second Derivatives:

$i = 1$ (forward difference)

$$\left. \frac{\partial^2 \phi}{\partial \xi^2} \right|_{1,j} = (2\phi_{1,j} - 5\phi_{2,j} + 4\phi_{3,j} - \phi_{4,j}) + O(\Delta \xi^2) + O[(\Delta \xi)^2] \quad (\text{B.7})$$

$1 < i < M$ (central difference)

$$\left. \frac{\partial^2 \phi}{\partial \xi^2} \right|_{i,j} = (\phi_{i+1,j} - 2\phi_{i,j} + \phi_{i-1,j}) + O[(\Delta \xi)^2] \quad (\text{B.8})$$

$i = M$ (backward difference)

$$\left. \frac{\partial^2 \phi}{\partial \xi^2} \right|_{M,j} = (2\phi_{M,j} - 5\phi_{M-1,j} + 4\phi_{M-2,j} - \phi_{M-3,j}) + O[(\Delta \xi)^2] \quad (\text{B.9})$$

$j = 1$ (forward difference)

$$\left. \frac{\partial^2 \phi}{\partial \eta^2} \right|_{i,1} = (2\phi_{i,1} - 5\phi_{i,2} + 4\phi_{i,3} - \phi_{i,4}) + O[(\Delta \eta)^2] \quad (\text{B.10})$$

$1 < j < N$ (central difference)

$$\left. \frac{\partial^2 \phi}{\partial \eta^2} \right|_{i,j} = (\phi_{i,j+1} - 2\phi_{i,j} + \phi_{i,j-1}) + O[(\Delta \eta)^2] \quad (\text{B.11})$$

$j = N$ (backward difference)

$$\left. \frac{\partial^2 \phi}{\partial \eta^2} \right|_{i,N} = (2\phi_{i,N} - 5\phi_{i,N-1} + 4\phi_{i,N-2} - \phi_{i,N-3}) + O[(\Delta \eta)^2] \quad (\text{B.12})$$

$i = 1, 1 < j < N$

$$\left. \frac{\partial^2 \phi}{\partial \xi \partial \eta} \right|_{1,j} = \frac{1}{2}(\phi_{2,j+1} - \phi_{2,j-1} - \phi_{1,j+1} + \phi_{1,j-1}) + O[(\Delta \xi)^2] + O[(\Delta \eta)^2] \quad (\text{B.13})$$

$1 < i < M, 1 < j < N$

$$\left. \frac{\partial^2 \phi}{\partial \xi \partial \eta} \right|_{i,j} = \frac{1}{4}(\phi_{i+1,j+1} - \phi_{i+1,j-1} - \phi_{i-1,j+1} + \phi_{i-1,j-1}) + O[(\Delta \xi)^2] + O[(\Delta \eta)^2] \quad (\text{B.14})$$

$i = M, 1 < j < N$

$$\left. \frac{\partial^2 \phi}{\partial \xi \partial \eta} \right|_{M,j} = \frac{1}{2}(\phi_{M,j+1} - \phi_{M,j-1} - \phi_{M-1,j+1} + \phi_{M-1,j-1}) + O[(\Delta \xi)^2] + O[(\Delta \eta)^2] \quad (\text{B.15})$$

APPENDIX C

PRESSURE EQUATION DISCRETIZATION

Letting the nodal point labeled A in equation (3.73) correspond to the point (i, j) and the point B in the equation represent the point (i+1, j), equation (3.73) can be put in the form

$$p_{i,j} = F_1 \left(\frac{\partial \psi}{\partial \xi} \right)_{i+1,j} + F_2 \left(\frac{\partial \psi}{\partial \eta} \right)_{i+1,j} + F_3 \left(\frac{\partial \psi}{\partial \xi} \right)_{i,j} + F_4 \left(\frac{\partial \psi}{\partial \eta} \right)_{i,j} + p_{i+1,j} \quad (\text{C.1})$$

where

$$F_1 = F_{y1} + F_{x2} \quad (\text{C.2})$$

$$F_2 = F_{y2} + F_{x1} \quad (\text{C.3})$$

$$F_3 = F_{y3} + F_{x4} \quad (\text{C.4})$$

$$F_4 = F_{y4} + F_{x3} \quad (\text{C.5})$$

with

$$F_{y1} = F_y (C_{x\xi})_{i+1,j} \quad (\text{C.6})$$

$$F_{y2} = F_y (C_{x\eta})_{i+1,j} \quad (\text{C.7})$$

$$F_{y3} = F_y (C_{x\xi})_{i,j} \quad (\text{C.8})$$

$$F_{y4} = F_y (C_{x\eta})_{i,j} \quad (\text{C.9})$$

$$F_{x1} = -F_x (C_{y\eta})_{i+1,j} \quad (\text{C.10})$$

$$F_{x2} = -F_x (C_{y\xi})_{i+1,j} \quad (\text{C.11})$$

$$F_{x3} = -F_x (C_{y\eta})_{i,j} \quad (\text{C.12})$$

$$F_{x4} = -F_x (C_{y\xi})_{i,j} \quad (\text{C.13})$$

and

$$F_y = \frac{1}{2} \left\{ \frac{\mu_{i+1,j} + \mu_{i,j}}{(K_y)_{i+1,j} + (K_y)_{i,j}} \right\} (y_{i,j} - y_{i-1,j}) \quad (\text{C.14})$$

$$F_x = \frac{1}{2} \left\{ \frac{\mu_{i+1,j} + \mu_{i,j}}{(K_x)_{i+1,j} + (K_x)_{i,j}} \right\} (x_{i,j} - x_{i-1,j}) \quad (\text{C.15})$$

Equation (C.1) is used, with proper differencing of the stream function derivatives, at all nodes in the quasi-steady state time step domain with the exception of the nodes along the impregnation front, i.e. the nodes where $i=M$. At these frontal nodes, the condition of vanishing pressure is enforced. The remaining computational domain nodal points where equation (C.1) is to be applied, is divided into nine subgroups, which are discretized using the differencing expressions listed in Appendix B. The nine nodal point regions are shown in Figure C.1, and the successive-substitution type equations which were used to determine pressures in each region were presented below:

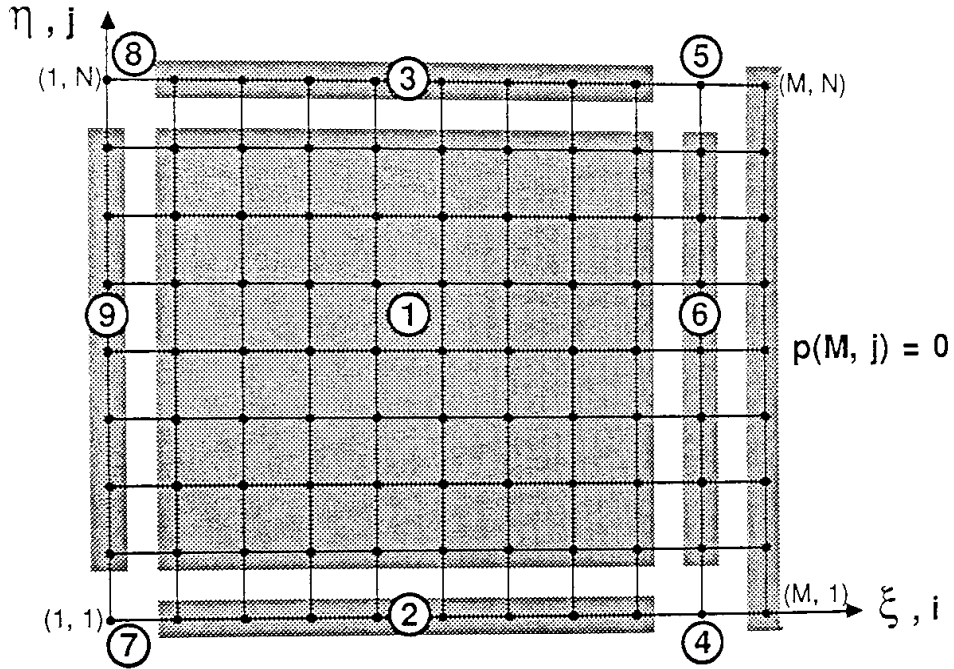


Figure C.1 Nodal point regions used discretized pressure equation

Equation (C.1) is derivatized in each region as follows:

Region 1: $2 \leq i \leq M-1, 2 \leq j \leq N-1$

$$\begin{aligned}
 p_{i,j} = & -\frac{1}{2}F_4\psi_{i,j-1} - \frac{1}{2}F_2\psi_{i-1,j-1} - \frac{1}{2}F_3\psi_{i-1,j} - \frac{1}{2}F_1\psi_{i,j} \\
 & + \frac{1}{2}F_3\psi_{i+1,j} + \frac{1}{2}F_1\psi_{i+2,j} + \frac{1}{2}F_4\psi_{i,j+1} + \frac{1}{2}F_2\psi_{i+1,j+1} + p_{i+1,j}
 \end{aligned} \tag{C.16}$$

Region 2: $2 \leq i \leq M-1, j=1$

$$\begin{aligned}
p_{i,1} = & -\frac{1}{2}F_3\psi_{i-1,1} + \left[\frac{1}{2}F_1 - \frac{3}{4}F_4\right]\psi_{i,j} + \left[\frac{3}{2}F_2 + \frac{1}{2}F_3\right]\psi_{i+1,j} \\
& + \frac{1}{2}F_1\psi_{i+2,1} + 2F_4\psi_{i,2} + 2F_2\psi_{i+2,2} - \frac{1}{2}F_4\psi_{i,3} - \frac{1}{2}F_2\psi_{i-1,3} + p_{i+1,1}
\end{aligned} \tag{C.17}$$

Region 3: $2 \leq i \leq M-1, j=N$

$$\begin{aligned}
p_{i,N} = & -\frac{1}{2}F_4\psi_{i,N-2} - \frac{1}{2}F_2\psi_{i+2,N-2} - 2F_4\psi_{i,N-1} - 2F_2\psi_{i+1,N-1} \\
& - \frac{1}{2}F_3\psi_{i-1,N} + \left[-\frac{1}{2}F_1 + \frac{3}{2}F_4\right]\psi_{i,N} + \left[\frac{3}{2}F_2 + \frac{1}{2}F_3\right]\psi_{i+1,N} \\
& - \frac{1}{2}F_1\psi_{i+2,N} + p_{i+1,N}
\end{aligned} \tag{C.18}$$

Region 4: $i=M-1, j=1$

$$\begin{aligned}
p_{M-1,1} = & \left[\frac{1}{2}F_1 - \frac{1}{2}F_3\right]\psi_{M-2,1} - \left[-2F_1 - \frac{3}{2}F_4\right]\psi_{M-1,1} \\
& + \left[\frac{3}{2}F_1 - \frac{3}{2}F_2 + \frac{1}{2}F_3\right]\psi_{M,1} + 2F_4\psi_{M-1,2} \\
& - 2F_2\psi_{M,2} - \frac{1}{2}F_4\psi_{M-1,3} - \frac{1}{2}F_2\psi_{M,3} + p_{M,1}
\end{aligned} \tag{C.19}$$

Region 5: $i=M-1, j=N$

$$\begin{aligned}
p_{M-1,N} = & \frac{1}{2}F_4\psi_{M-1,N-2} + \frac{1}{2}F_2\psi_{M,N-2} - 2F_4\psi_{M-1,N-1} - 2F_2\psi_{M,N-1} \\
& + \left[\frac{1}{2}F_1 - \frac{1}{2}F_3\right]\psi_{M-2,N} + \left[2F_1 + \frac{3}{2}F_4\right]\psi_{M-1,N} \\
& + \left[\frac{3}{2}F_1 + \frac{3}{2}F_2 + \frac{1}{2}F_3\right]\psi_{M,N} + p_{M,N}
\end{aligned} \tag{C.20}$$

Region 6: $i = M-1, 2 \leq j \leq N-1$

$$\begin{aligned}
p_{M-1,j} = & -\frac{1}{2}F_4\psi_{M-1,j-1} - \frac{1}{2}F_2\psi_{M,j-1} + \left[\frac{1}{2}F_1 - \frac{1}{2}F_3\right]\psi_{M-2,j} \\
& - 2F_1\psi_{M-1,j} + \left[\frac{3}{2}F_1 + \frac{1}{2}F_3\right]\psi_{M,j} - \frac{1}{2}F_4\psi_{M-1,j+1} \\
& - \frac{1}{2}F_2\psi_{M,j+1} + p_{M,j}
\end{aligned} \tag{C.21}$$

Region 7: $i = 1, j = 1$

$$\begin{aligned}
p_{1,1} = & \left[-\frac{1}{2}F_1 - \frac{3}{2}F_3 - \frac{3}{2}F_4\right]\psi_{1,1} + \left[-\frac{3}{2}F_2 - 2F_3\right]\psi_{2,1} \\
& + \left[\frac{1}{2}F_1 - \frac{1}{2}F_3\right]\psi_{3,1} + 2F_4\psi_{1,2} + 2F_2\psi_{2,2} \\
& - \frac{1}{2}F_4\psi_{1,3} - \frac{1}{2}F_2\psi_{2,3} + p_{2,1}
\end{aligned} \tag{C.22}$$

Region 8: $i = 1, j = N$

$$\begin{aligned}
p_{1,N} = & -\frac{1}{2}F_4\psi_{1,N-2} + \frac{1}{2}F_2\psi_{2,N-2} - 2F_4\psi_{1,N-1} - 2F_2\psi_{2,N-1} \\
& + \left[\frac{1}{2}F_1 - \frac{3}{2}F_3 + \frac{3}{2}F_4\right]\psi_{1,N} + \left[\frac{3}{2}F_2 + 2F_3\right]\psi_{2,N} \\
& + \left[\frac{1}{2}F_1 - \frac{1}{2}F_3\right]\psi_{3,N} + p_{2,N}
\end{aligned} \tag{C.23}$$

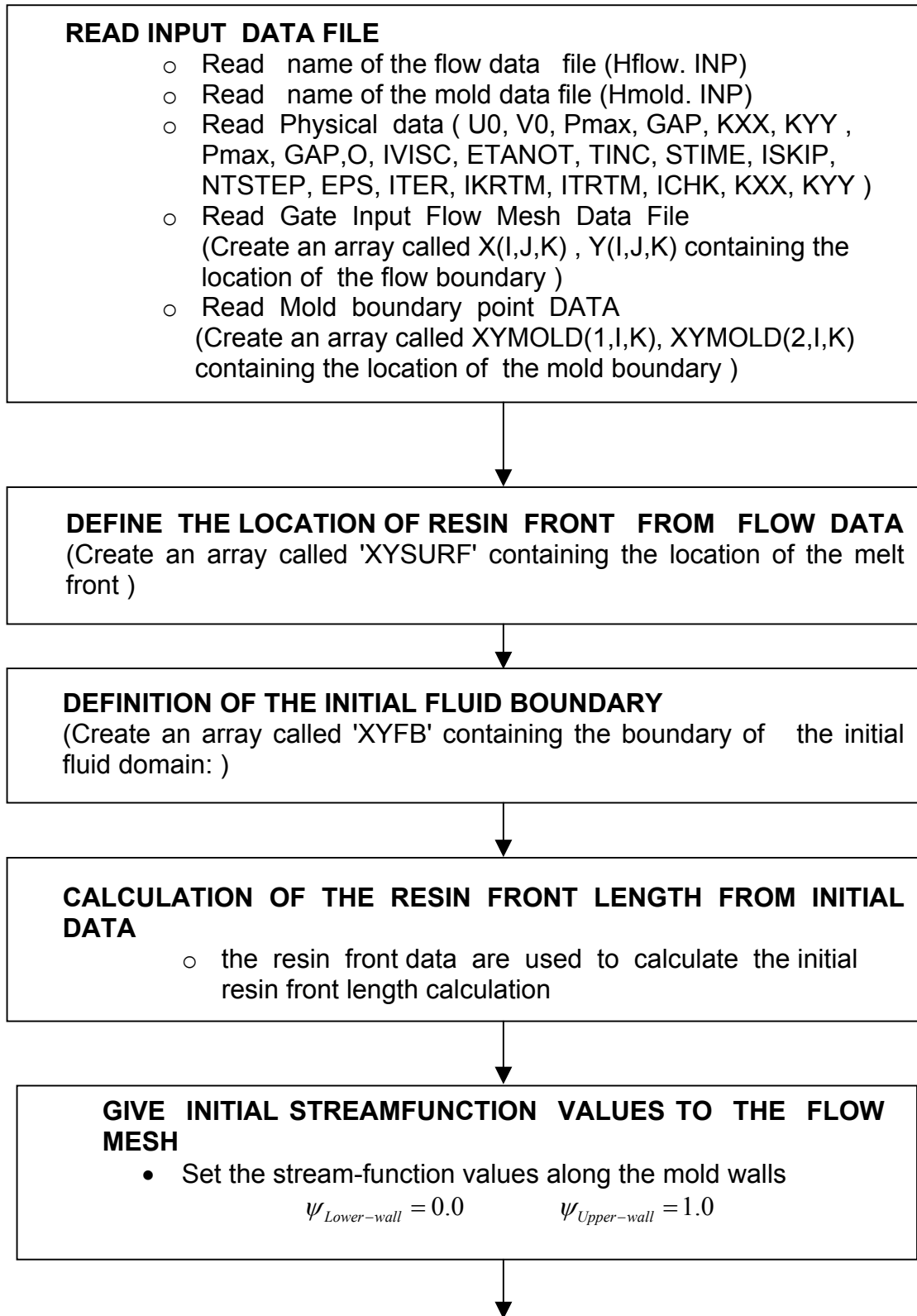
Region 9: $i = 1, 2 \leq j \leq N-1$

$$\begin{aligned}
p_{1,j} = & -\frac{1}{2}F_4\psi_{1,j-1} - \frac{1}{2}F_2\psi_{2,j-1} + \left[-\frac{1}{2}F_1 - \frac{3}{2}F_3\right]\psi_{1,j} \\
& - 2F_3\psi_{2,j} + \left[\frac{1}{2}F_1 - \frac{1}{2}F_3\right]\psi_{3,j} + \frac{1}{2}F_4\psi_{1,j+1} \\
& + \frac{1}{2}F_2\psi_{2,j+1} + p_{2,j}
\end{aligned} \tag{C.24}$$

The use of equation (C.16) through (C.24) along with the trivial equations $p_{M,j} = 0$ which is applied at all nodal points on the impregnation front, results in a system of linear algebraic equation for pressure.

APPENDIX D

COMPUTER PROGRAM FLOW CHART



ITERATION BEGINS

CALL SUBROUTINE TCOEFF

- Calculate the coefficients (alpha, beta, gamma, Jacobian, etc.) of governing equation in the computational domain, needed for the coordinate transformations.

CALL SUBROUTINE VISCO

- Use Newtonian model to assign nodal viscosity values

Is this the first
time step?

YES

CALL SUBROUTINE PKCAL

- This subroutine calculates the pressure for the first time step only, Darcy's Law

$$\frac{\partial P}{\partial x} = -\frac{\mu}{K_x} u$$

CALL SUBROUTINE STREAMRTM

- This subroutine calculates the streamfunction values from Darcy's law and continuity

$$\frac{\mu}{K_y} \frac{\partial \psi^2}{\partial x^2} + \frac{\mu}{K_x} \frac{\partial \psi^2}{\partial y^2} + \left[\frac{1}{K_x} \frac{\partial \mu}{\partial y} - \frac{\mu}{K_x^2} \left(\frac{\partial K_x}{\partial y} \right) \right] \frac{\partial \psi}{\partial y} + \left[\frac{1}{K_y} \frac{\partial \mu}{\partial x} - \frac{\mu}{K_y^2} \left(\frac{\partial K_y}{\partial x} \right) \right] \frac{\partial \psi}{\partial x} = 0$$

